공학박사 학위논문

Nanostructured Bulk of Doped Strontium Titanium Oxide and Bismuth Telluride for Thermoelectric Applications

열전 응용을 위한 도핑된 티탄산 스트론튬과 비스무스 텔루라이드의 제조

2017년 2월

서울대학교 대학원

화학생물공학부

박 건 수

Abstract

Nanostructured Bulk of Doped Strontium Titanium Oxide and Bismuth Telluride for Thermoelectric Applications

Kunsu Park
School of Chemical and Biological Engineering
The Graduate School
Seoul National University

Enhancement of thermoelectric performance is of key importance in the practical application of thermoelectric materials. Recently, the use of nanostructured bulk materials has been proposed to exploit the reduction in the thermal conductivity and consequently increase in the dimensionless figure-of-merit *ZT*. In this dissertation, I will discuss synthesis of nanocrystals, their compaction to nanostructured bulk materials, and the thermoelectric property characterization. Amongst

many thermoelectric candidate materials, I will focus on nanostructured bulk materials of La-doped $SrTiO_3$ and K-doped Bi_2Te_3.

First, I will report on the synthesis of La-doped $SrTiO_3$ nanoparticles with controlled La doping levels and their enhanced thermoelectric properties. The nanoparticles were sintered using a spark plasma sintering process to fabricate nanostructured bulk materials. The *ZT* value reaches a maximum of ~0.37 at 973 K, which is ~25% higher than that of the single-crystal bulk material. The increased *ZT* is due to the reduction of the thermal conductivity while maintaining the electrical conductivity and Seebeck coefficient. In addition, the nanostructured bulk La-doped $SrTiO_3$ exhibits thermal stability even after heat treatment at 973 K, demonstrating their suitability for high-temperature applications.

Second, I will report on the preparation of new nanostructured bulk materials of bismuth telluride having non-equilibrium phase compositions. Furthermore, potassium cations, which act as unconventional electron donors, were successfully doped into the bulk bismuth telluride. According to the results of scanning transmission electron microscope with electron energy loss spectroscopy studies and density functional theory calculations, K cations occupy the interlayer

and interstitial sites. The resulting compounds with high tellurium and potassium concentrations show increased electrical conductivity and the Seebeck coefficient. Consequently, a high power factor of ~43 μW cm^{-1} K^{-2} and the ZT >1.1 at 350 K, which are among the highest values observed for n-type bismuth telluride materials, are achieved in the thermoelectric measurements.

Keywords: Thermoelectric materials, doping, nanostructured bulk, nanocrystal synthesis, strontium titanate, bismuth telluride.

Student Number: 2009-20989

Contents

List of Tables

List of Schemes

List of Figures

Chapter 1. Introduction: Bulk Nanostructured Materials for Enhanced Thermoelectric Efficiency and Dissertation Overview

1.1 Introduction to Thermoelectrics

The need for sustainable energy sources to replace the combustion of fossil fuels has become the one of the most critical issues of the modern day. There have been many candidates to meet this energy challenge using the renewable sources such as sunlight, wind, rain, tides, waves, and geothermal heat for power generation. Along with these popular renewable energy sources, thermoelectrics have drawn attention over the past few decades for their ability to generate power using waste heat. Thermoelectric materials directly convert between thermal and electrical energy without any moving parts or chemical reactions; therefore, they are applicable to solid-state electricity generation and refrigeration devices.[1] Despite many advantages, thermoelectric materials have been only used in a few cases such as deep-space probes, automobiles, coolers, and biothermal betteries, because their low

efficiency limits widespread practical usage.[2]

The effectiveness of a thermoelectric material is determined by measuring the dimensionless figure of merit, *ZT*,

$$ZT = \frac{S^2\sigma}{\kappa}T$$

where *S* is the Seebeck coefficient, σ is the electrical conductivity, *T* is temperature, and κ is the thermal conductivity. To develop highly efficient thermoelectric materials, we must increase the electrical conductivity and the Seebeck coefficient, and also decrease the thermal conductivity. However, these three components making up the *ZT* are unfavorably correlated with each other, presenting a serious obstacle to enhance the efficiency. Generally, the electrical conductivity is increased with higher carrier concentration, such as in metals, while the Seebeck coefficient and the thermal conductivity are increased with lower carrier concentrations, such as in insulators (Figure 1.1).[3] Optimization of *ZT* by controlling the carrier concentration of the material is possible, however this approach is not feasible for obtaining high *ZT* required for thermoelectric applications. To obtain a high *ZT*, we must find new thermoelectric materials that intrinsically have high $S^2\sigma$ and low thermal conductivity. Another way to improve *ZT* is to

break the correlation between the conductivities and the Seebeck coefficient by using well-designed band engineering and micro/nanostructuring.[4]

Before investigating the strategies for enhancing thermoelectric efficiency, we start with a discussion of the fundamental thermoelectric phenomena, which are based on the Seebeck effect. Thomas Seebeck discovered that if two different metals are connected together with different temperatures, then an electrical current, which is termed "thermoelectricity", is induced by the voltage difference at the junction. Further, Jean Peltier explored the related effect that heat is absorbed when the electrical current flows through the junction. The basic mechanism of this effect is depicted in Figure 1.2.[5] The carriers in the material (electrons in this case) become more energetic at hot side (T_H) than at cold side (T_C) of the temperature gradient. Then the diffusion of carriers from T_H to T_C establishes the electric field, which is generated as long as the temperature gradient is maintained, and the current flows like in a battery.

To maximize current generation from the heat flow, we use an n-type and p-type pair of thermoelectric materials, termed a thermoelectric couple (Figure 1.3). Commercialized thermoelectric devices are

composed of many of these thermoelectric couples in their modules (Figure 1.4). Because the Seebeck and Peltier effect are thermodynamically reversible, a thermoelectric module for power generation can be also used for electronic cooling.

Starting with a thermoelectric couple consisting of n- and p-type thermoelectric materials, the basic unit of a thermoelectric module, we now discuss the overall thermoelectric efficiency. With the heat flow rate (Q_H), the thermoelectric efficiency (η) of power generation is determined by:

$$\eta = \frac{W}{Q_H} = \frac{T_H - T_C}{T_H}\left(\frac{\sqrt{1+ZT_{avg}}-1}{\sqrt{1+ZT_{avg}}+{T_C}/{T_H}}\right)$$

where W is the load, T_H is the temperature of hot side, T_C is that of cold side, and T_{avg} is the average temperature across the two sides. We assume that there is no irreversible loss of thermal and electrical energy from contact resistance or thermal radiation and, thus, the thermoelectric efficiency is proportional to the Carnot efficiency in this equation. Because the Carnot efficiency is the fundamental upper-bound of the thermal efficiency, which is determined by the device operating temperature, the thermoelectric efficiency is dependent only

on the figure of merit, *ZT,* of the material at a fixed temperature. The figure of merit, *ZT,* of a thermoelectric couple is determined by:

$$ZT = \frac{(S_p - S_n)^2 T}{\left[\sqrt{(\kappa_n/\sigma_n)} + \sqrt{(\kappa_p/\sigma_p)}\right]^2}$$

Thus, to maximize the thermoelectric efficiency, we need high *ZT* materials of n-type and p-type at the operating temperature, T_{avg}. If we increase *ZT* to 3 for a given ΔT, it is expected the thermoelectric efficiency would be around 30%, making thermoelectric energy generation an attractive alternative to fossil fuels in some cases.[5]

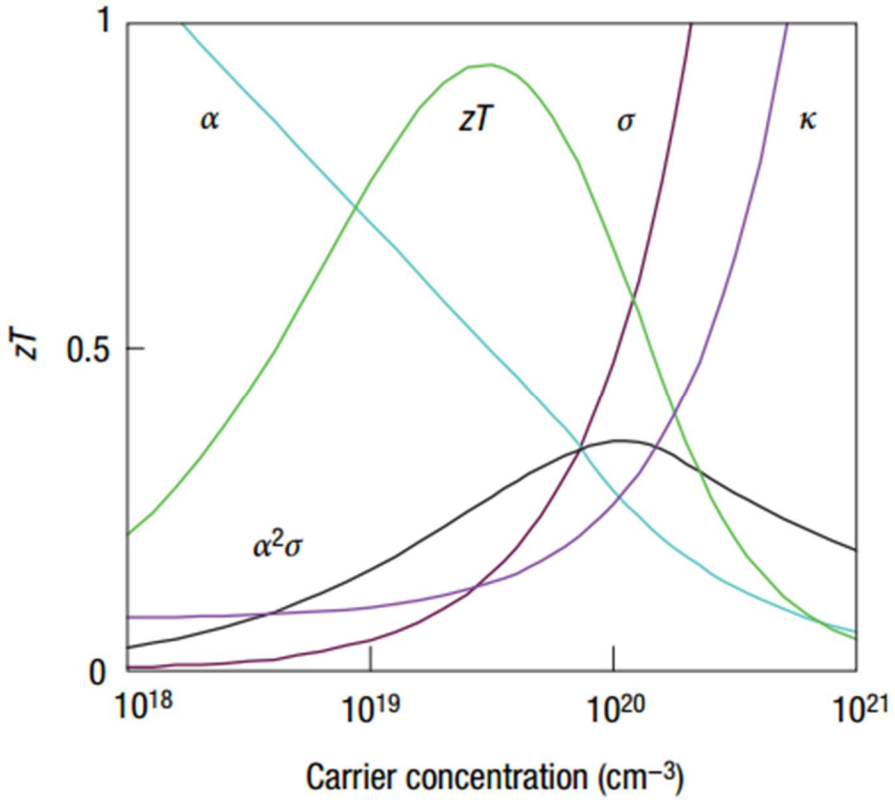

Figure 1.1 Thermoelectric *ZT* optimization through carrier concentration tuning. Typically, *ZT* maximizes in heavily doped semiconductors with a carrier concentration between 10^{19} and 10^{21} carriers per cm^3. (from Ref. [3], Snyder, G. J.; Toberer, E. S. *Nat. Mater.* **2008**, *7*, 105).

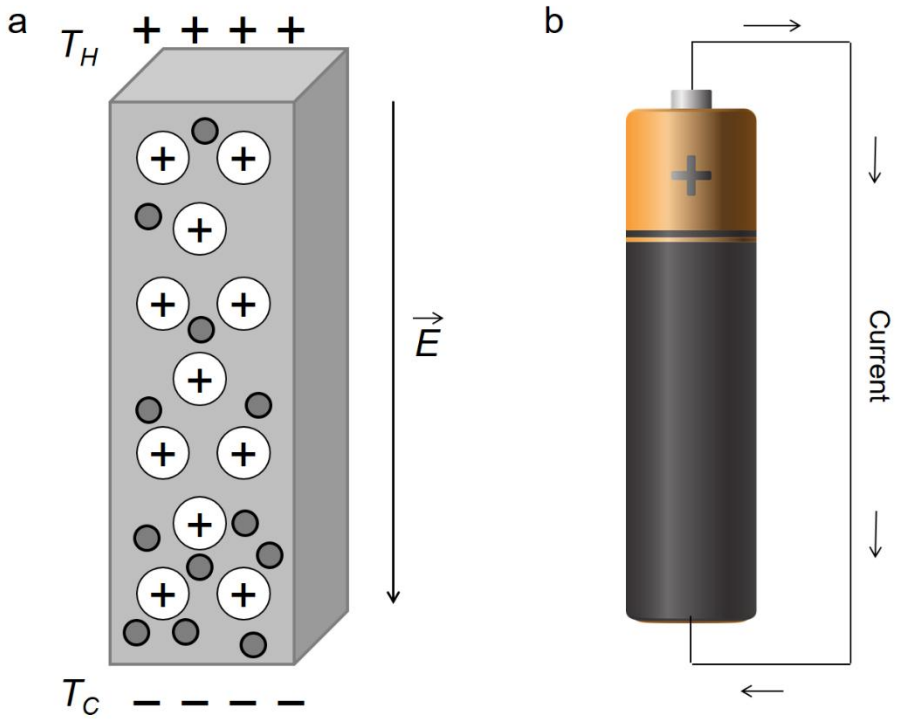

Figure 1.2 Illustration depict the thermoelectric effect. **(a)** When a external temperature gradient establishes to a material, energetic free electrons diffuse to the cold side (T_C) from hot side (T_H) then an electric field is developed. **(b)** Electric field induces the current flow like a battery.

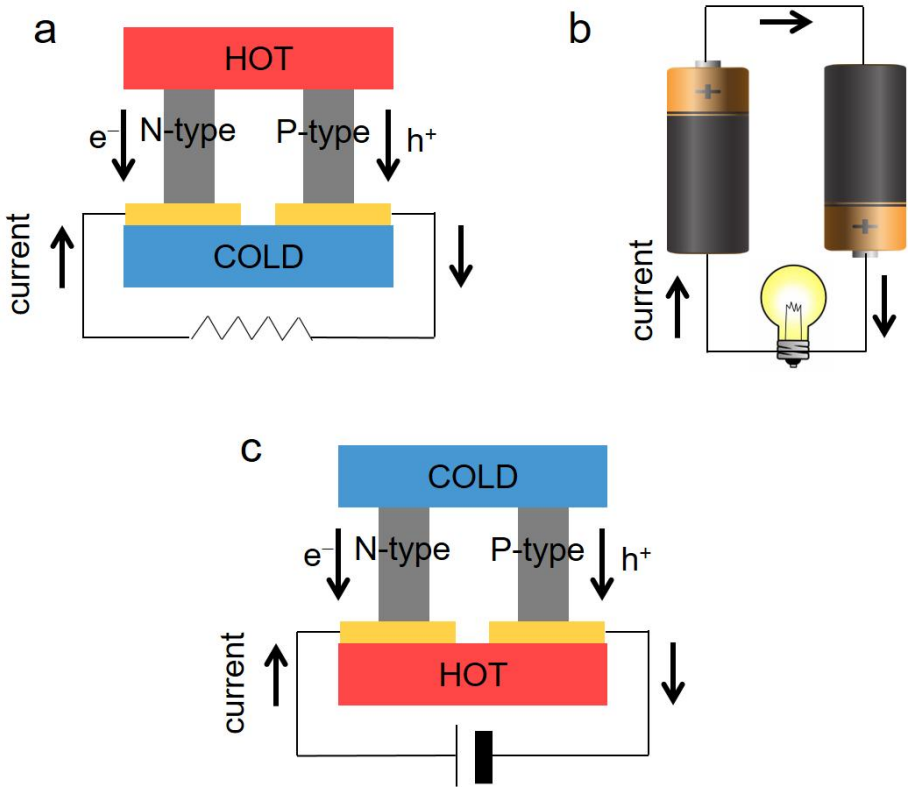

Figure 1.3 Thermoelectric couples made of n-type and p-type thermoelectric materials. **(a)** Electrical power generation. **(b)** Comparison to two batteries in series. **(c)** Peltier cooling.

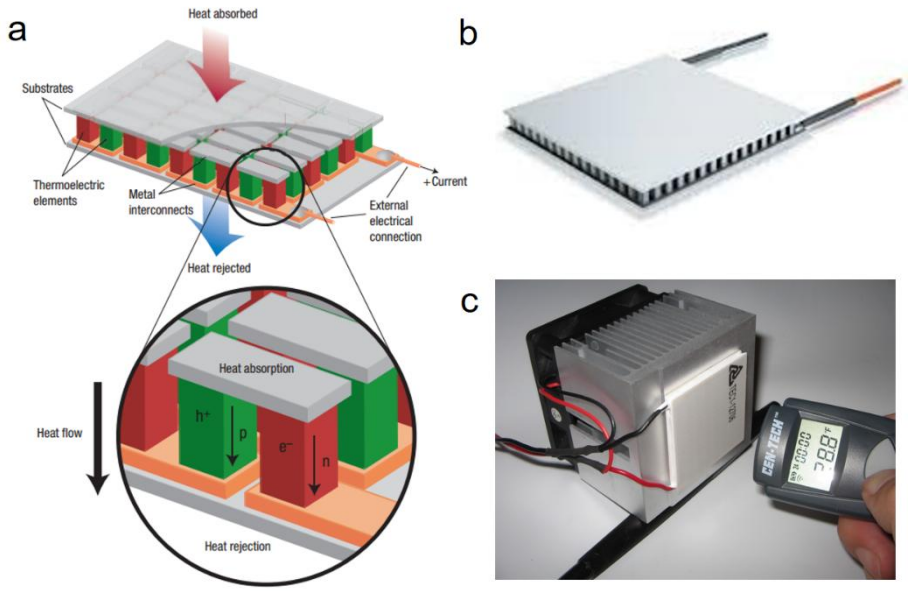

Figure 1.4 (a) Thermoelectric module consists of thermoelectric couples. **(b)** Real module and **(c)** thermoelectric module which is used as Peltier cooler. (from Ref. [3], Snyder, G. J.; Toberer, E. S. *Nat. Mater.* **2008**, *7*, 105).

1.2 Improvement in Thermoelectric Materials

Historically, there have been many attempts to find new, high performance thermoelectric materials. After the discovery of the thermoelectric phenomenon by Seebeck, a few materials have proven their effectiveness.[6] However, a material with an intrinsically high electrical conductivity, Seebeck coefficient and low thermal conductivity remains elusive due to the co-dependency of the factors controlling these values, as discussed earlier. Therefore, recent efforts to achieve a high *ZT* have focused on manipulating conventional materials that show good thermoelectric properties and studying the fundamental mechanism that controls the thermoelectric effect. In the past two decades, the field of thermoelectrics has seen rapid advancement by the development of new strategies to enhance the efficiency of materials (Figure 1.5).[4]

Given the equation which determines the *ZT*, the strategies for enhancing *ZT* include increasing the power factor ($PF = S^2\sigma$) while keeping the thermal conductivity constant, reducing the thermal conductivity while keeping the electrical conductivity constant, and increasing the *PF* and reducing κ simultaneously. However, as discussed earlier, σ, *S*, and κ are interrelated and therefore, it is

challenging to control each variable separately. To overcome this problem and enhance the power factor, the band structure of materials is modified by appropriate doping and alloying, resulting in the increased *ZT* by changing the electrical transport properties.[7]

Another approach for enhancing *ZT* is reducing the thermal conductivity.[8] This concept is based upon separation of the thermal conductivity from the electrical conductivity. The total thermal conductivity κ_T is:

$$\kappa_T = \kappa_e + \kappa_L$$

where κ_e and κ_L are the electronic and the lattice contributions, respectively. Through Wiedemann-Franz law, the electrical conductivity is proportional to the thermal conductivity:

$$\kappa_e = L_0 \sigma T$$

where L_0 is the Lorenz number, 2.4×10^{-8} J^2 K^{-2} C^{-2}, for free electrons. Thus, efforts to reduce the thermal conductivity are focused on reducing the lattice thermal conductivity, which can be controlled independently of the electrical conductivity.

As is commonly known, insulators have low thermal conductivity. Glasses, for example, exhibit one of the lowest lattice thermal conductivities. However, glasses are not suitable as good thermoelectric

materials because of their poor electrical transport properties compared to typical semiconductors. Thus, we need a material with low lattice thermal conductivity, like a glass, and high electrical transport properties, like a crystal. Such a material is called a "phonon glass electron crystal" (PGEC), which was proposed by Slack to enhance the thermoelectric *ZT*.[6] In following chapters, we explore methods to disrupt the movement of phonons, which are directly related to the lattice thermal conductivity, while keeping the electrical conductivity constant (Figure 1.6).

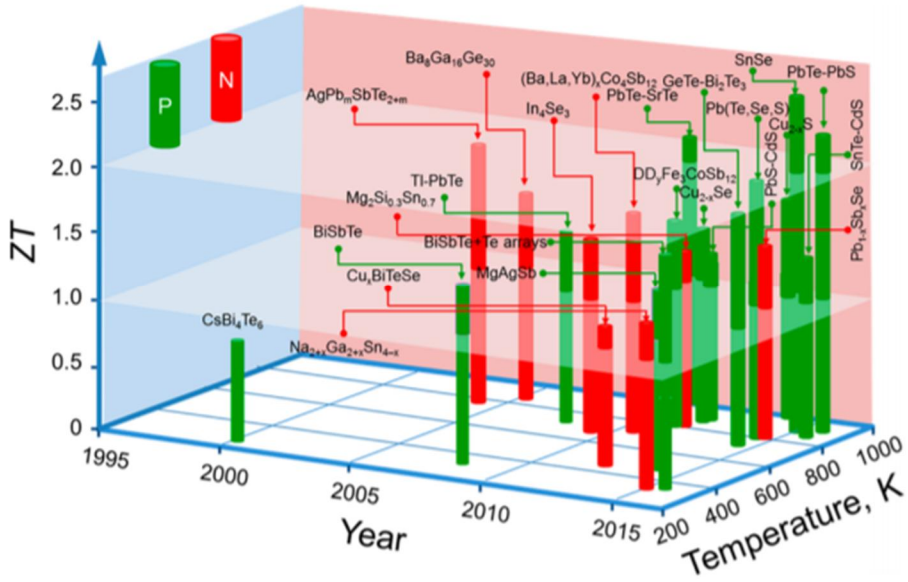

Figure 1.5 State-of-art bulk thermoelectric materials. Thermoeletric figure-of-merit ZT is shown as a function of temperature and year. (from Ref. [4], Tan, G.; Zhao, L. D.; Kanatzidis, M. G. *Chem. Rev.* **2016**, *116*, 12123).

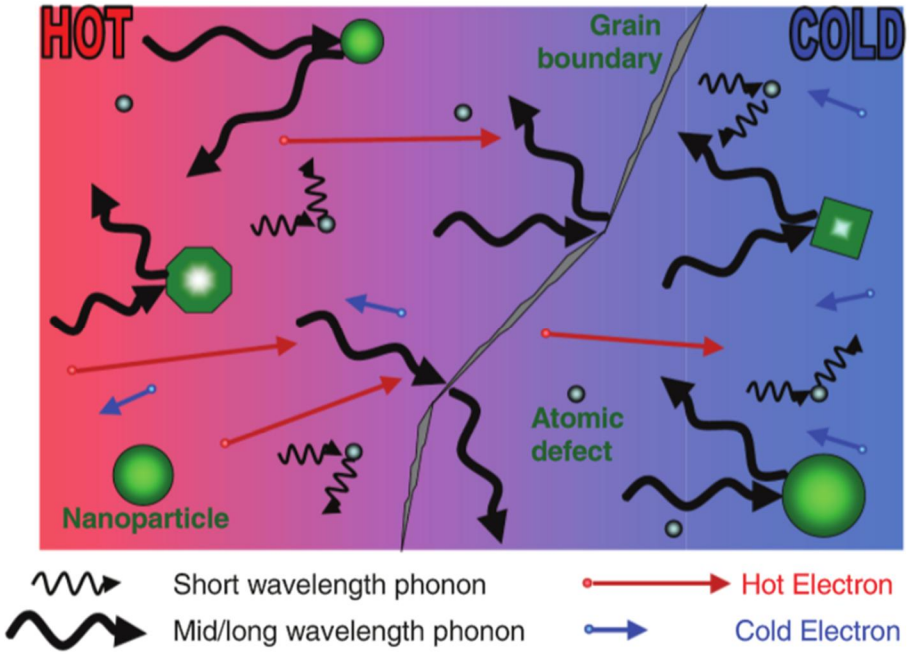

Figure 1.6 Schematic illustration showing phonon scattering mechanisms. Grain boundary and embedded nanoparticles inhibit the phonon transport. (from Ref. [8a], Vineis, C. J.; Shakouri, A.; Majumdar, A.; Kanatzidis, M. G. *Adv. Mater.* **2010**, *22*, 3970).

1.3 Nanostructured Themoelectric Materials with Low Lattice Thermal Conductivities

There have been many attempts to reduce the lattice thermal conductivity by manipulating phonons. Phonons are heat carriers and result from vibrational waves in the lattice structure of the crystal. Many materials with intrinsically low lattice thermal conductivity have an unusual crystal structure. These include cages with rattling atoms inside,[9] highly anisotropic structures,[10] copper ionic liquid-like structures,[11] and ternary or quaternary compounds with increased lattice period.[12] In this introductory review, we will not cover all the recent advances of thermoelectric materials which are mentioned above. Instead we herein focus on the nanostructured composite materials that utilize interface scattering of phonons. Many of the recent improvements to thermoelectric properties come from nanostructuring of materials. In the late 1900s, the theory that reducing the dimension of the crystal would enhance *ZT* was proved experimentally in thin-films and nanowires.[13] It is clear that low dimensional materials decrease the lattice thermal conductivity, however, maintaining the high power factor is a great challenge. Successful enhancement of *ZT* was

accomplished in Bi_2Te_3-Sb_2Te_3 superlattice thin film (Figure 1.7),[14] PbSeTe-PbTe thin film (Figure 1.8),[1c] and Si nanowires (Figure 1.9),[15]. However, their delicate structures are very difficult to replicate and scale-up, excluding their commercial application possibility. This suggests that thermoelectric materials should have stable crystal structure and coherent interface for scattering of phonons in bulk scale.

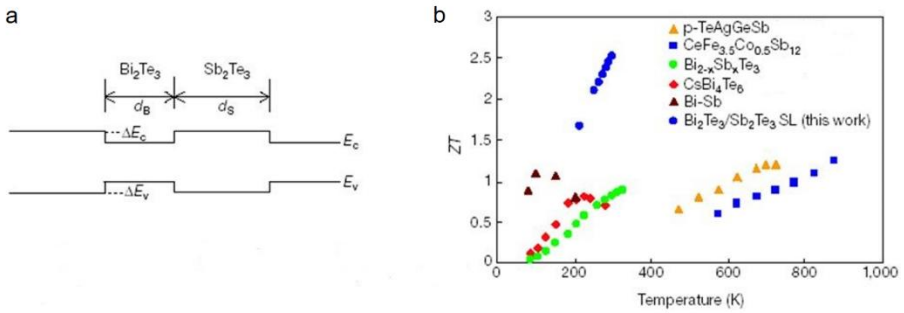

Figure 1.7 (a) The heterojuction band diagram. **(b)** Temperature dependence of *ZT* of 10Å/50Å p-type Bi_2Te_3/Sb_2Te_3 superlattice compared to those of several reported thermoelectric materials. (from Ref. [14], Venkatasubramanian, R.; Siivola, E.; Colpitts, T.; O`Quinn, B. *Nature* **2001**, *413*, 597).

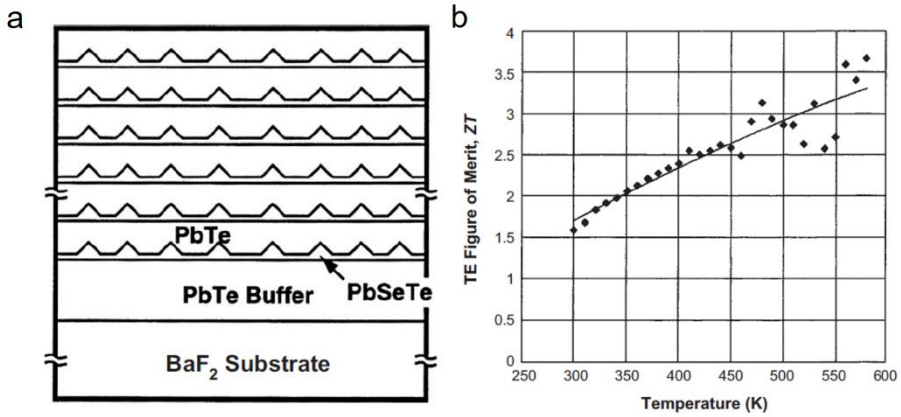

Figure 1.8 (a) Schematic drawing of a quantum-dot superlattice, and **(b)** thermoelectric figure-of-merit *ZT* as a function of temperature for an n-type $PbSe_{0.98}Te_{0.02}$/PbTe superlattice. (from Ref. [1c], Dresselhaus, M. S.; Chen, G.; Tang, M. Y.; Yang, R.; Lee, H.; Wang, D.; Ren, Z.; Fleurial, J.; Gogna, P. *Adv. Mater.* **2007**, *19*, 1043).

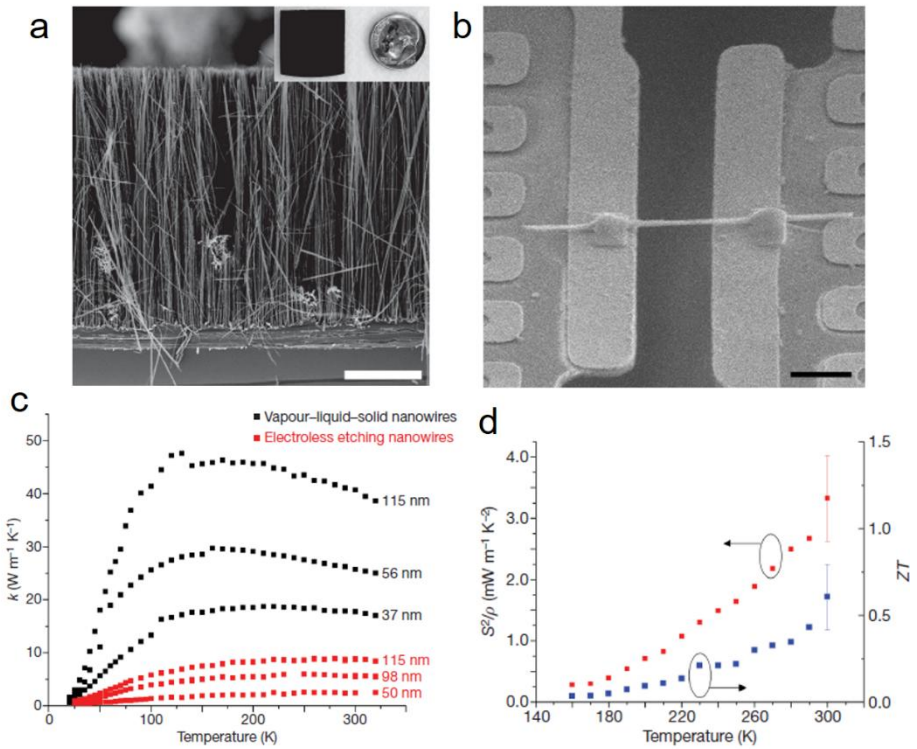

Figure 1.9 (a) SEM image of Si nanowire array. Scale bar, 10um. **(b)** SEM image of a single Si nanowire attached to two pads for measuring the conductivities. **(c)** The temperature-dependent thermal conductivity of Si nanowire with different thickness. **(d)** Single Si nanowire power factor and calculated *ZT*. (from Ref. [15a], Hochbaum, A. I.; Chen, R.; Delgado, R. D.; Liang, W.; Garnett, E. C.; Najarian, M.; Majumdar, A.; Yang, P. *Nature* **2007**, *451*, 163).

1.3.1 Nanostructuring with Different Phases

The theory that low dimensional structures would have increased thermoelectric *ZT* was successfully proved in thin-films. However, scalability is very important to be applicable in real solid-state devices. Therefore, ideal thermoelectric materials are bulk materials that have nanoscale properties. Here, we call these materials as nanostructured bulk materials. Incorporation of nanoscale defects in the bulk material has been demonstrated by using thermal processing techniques.[16] Non-stoichiometric compounds were melted to form nanostructures inside a host material by a rapid cooling process. This approach has been applied to $Ag_nPb_mSb_nTe_{2+m}$ (LAST) and PbTe-PbS-PbSe.

The LAST compounds have a cubic NaCl structure with isotropic morphology and high crystal symmetry.[16a] This material (n=1, m=18) showed a high power factor of 28 μW cm^{-1} K^{-2}, which is one of the highest among known materials, by maintaining good electrical conductivity without a noticeable loss in the Seebeck coefficient (Figure 1.10). Also, very low thermal conductivity was observed, attributed to the inhomogeneity of the material. This resulted in the *ZT* value of ≈ 1.7 at ~ 700 K. In TEM analysis, quantum dot inclusions, which are generated during the synthesis, have an Ag-Sb-rich

composition; these quantum dots and their surrounding structures are epitaxially coherent. These small precipitates are believed to play a key role in the thermal conductivity reduction of the lattice, and for obtaining high *ZT*.

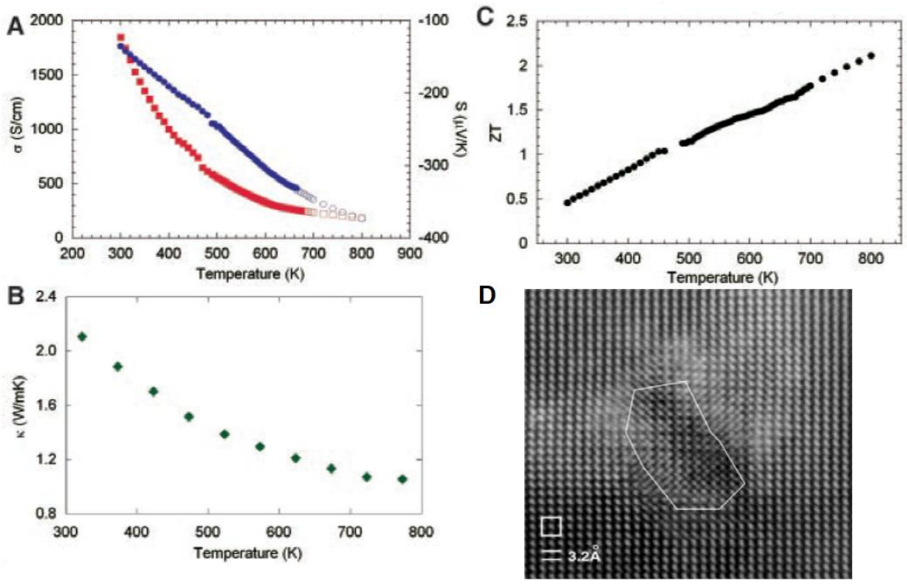

Figure 1.10 Temperature-dependent transport properties for $AgPb_{18}SbTe_{20}$. **(a)** Electrical conductivity and Seebeck coefficient, **(b)** thermal conductivity, and **(c)** *ZT*. **(d)** High resolution TEM image of $AgPb_{18}SbTe_{20}$ sample showing "nanodot" inside. (from Ref. [16a], Hsu, K. F.; Loo, S.; Guo, F.; Chen, W.; Dyck, J. S.; Uher, C.; Hogan, T.; Polychroniadis, E. K.; Kanatzidis, M. G. *Science* **2004**, *303*, 818).

Pristine PbTe is one of the best thermoelectric materials, showing good performance at mid-range temperatures of ~ 600 K. As in the case of LAST, manipulation of PbTe materials by alloying or doping with appropriate guest materials has many advantages. Among many dopants, Tl and Sn are effective for enhancing the thermoelectric *ZT*.[17] For example, the PbTe:Tl system showed a large *ZT* value of 1.5 at 773 K, which was attributed to an increase in the Seebeck coefficient.[17a]

Inspired by the discovery that the generation of nano-inclusions enhances *ZT*, nanostructuring PbTe has been rigorously explored. Various kinds of chalcogenides, such as M-Te, M-S, M-Se (M=Sr, Ag, Ca, Cd, and Hg) may act as inclusions embedded in PbS, PbSe, and PbTe matrices and have been successfully shown to decrease the lattice thermal conductivity.[4]

PbTe-PbS is a representative example showing that the lattice thermal conductivity can be greatly reduced by preservation of nanostructure in the matrix (Figure 1.11).[16b] The HRTEM image shows that PbTe sample containing 16% PbS consists of many strips with 3 -10 nm sized particles in the matrix, which are formed by a nucleation and growth mechanism. From measurements of the properties, it has been shown that this phase separation is responsible for the very low thermal

conductivity. We can see the *ZT* value was improved in nanophase PbS containing PbTe, relative to that in PbTe alone, by almost a factor of two. This work further demonstrates that nanostructuring can lead to significant improvements in thermoelectric properties.

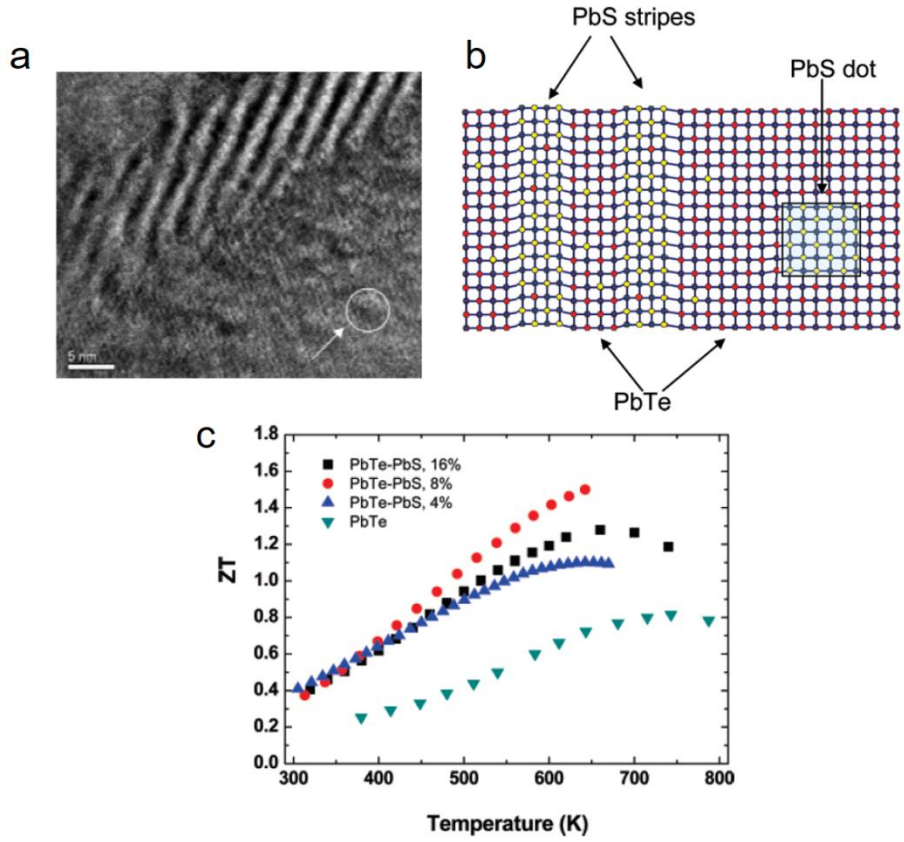

Figure 1.11 (a) HRTEM image showing PbTe-PbS mixed matrix. **(b)** Structure of the mixture which shows PbS stripes and dots. **(c)** Dimensionless figure-of-merit as a function of temperature. *ZT* peak of 1.5 at 642 K for $x = 0.08$. (from Ref. [16b], Androulakis, J.; Lin, C.; Kong, H.; Uher, C.; Wu, C.; Hogan, T.; Cook, B. A.; Caillat, T.; Paraskevopoulos, K. M.; Kanatzidis, M. G. *J. Am. Chem. Soc.* **2007**, *129*, 9780).

1.3.2 Nanostructured Bulk Materials from Bottom-Up Process

In the previous examples, nanoscale manipulation was successfully employed to improve the thermoelectric performance of various types materials prepared by different methods. Here, we discuss a simple and cheap method of introducing nanostructures into thermoelectric materials with bulk scale by the compaction of nanocrystals into dense nanostructured bulk materials. Typically, bulk materials are produced by hot pressing or spark plasma sintering process of fine nano-sized powders, which are produced from ball-milling or chemically synthesized via colloidal method. Unlike nano-inclusions in a matrix model, which was previously discussed, this process forms a homogeneous polycrystalline material with a huge amount of interface between the compacted nanocrystals that can lower the thermal conductivity of the material.[8d, 18] This method can easily produce a large scale of bulk materials with decreased thermal conductivity at a relatively low-cost. However, many challenges still remain in this method. One of the problems is obtaining high density. Impurities in

the particles or void formation decrease the relative density and lead to a decrease in the electrical transport properties and, thus, the *ZT* value.

Recent success in producing nanostructured bulk materials using this bottom-up fabrication is shown in a p-type BiSbTe alloy ($Bi_{0.5}Sb_{1.5}Te_3$) (Figure 1.12).[18a] This material was produced by hot-pressing of ball-milled powders, and exhibited a *ZT* value of 1.4 at 373 K, which is much higher than the state-of-the-art p-type BiSbTe ingots. The increase in *ZT* value is mainly attributed to a large decrease of the thermal conductivity. Also, a slightly increased power factor was observed, which is assumed to be due to the changes in carrier concentration and the mobility.

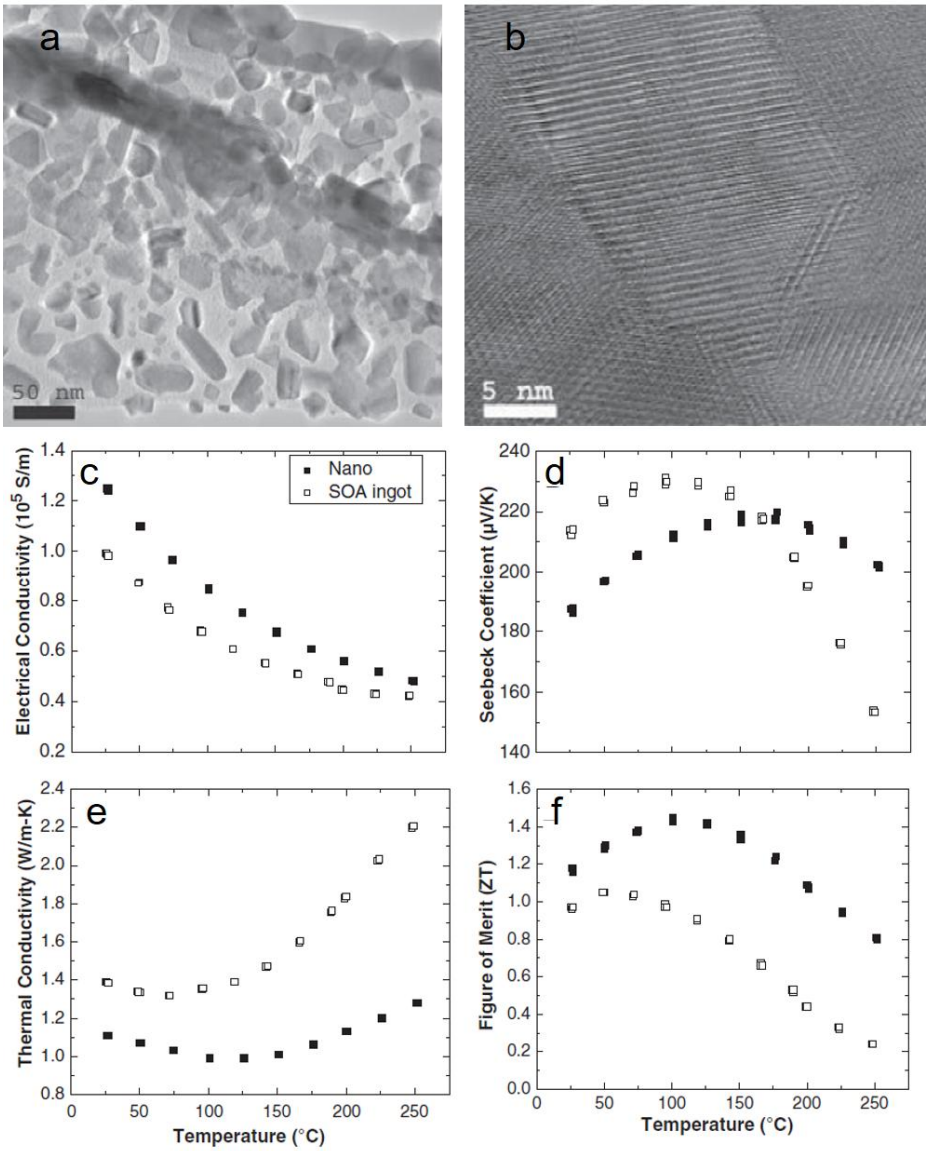

Figure 1.12 (a) TEM image of as-milled nanopowder of BiSbTe. **(b)** High resolution TEM image of hot-pressed nanostructured bulk showing the nanograins inside the matrix. Nanograins have high

crystallinity, random orientation, and clear grain broundaries. Temperature dependence of **(c)** the electrical conductivity, **(d)** the Seebeck coefficient, **(e)** the thermal conductivity, and **(f)** *ZT* value as compared with that of commercial ingot (white square). (from Ref. [18a], Poudel, B.; Hao, Q.; Ma, Y.; Lan, Y.; Minnich, A.; Yu, B.; Yan, X.; Wang, D.; Muto, A.; Vashaee, D.; Chen, X.; Liu, J.; Dresselhaus, M. S.; Chen, G.; Ren, Z. *Science* **2008**, *320*, 634).

1.3.3 Chemically Synthesized Colloidal Nanocrystals for Nanostructured Bulk Assembly

The development of nanocrystals synthesized over the last 20~30 years has greatly advanced the whole materials science field. The physical and chemical properties of nanocrystals can be modified by changing their size, shape, and composition. Also, colloidal chemistry allows nanocrystals to be synthesized in a large scale and at low-cost, which is very desirable for further applications. The advantages of colloidal snthesis of nanocrystals suggest a new efficient method for the formation of nanostructured thermoelectric materials.

As discussed earlier, it has been shown that nanostructuring reduces the lattice thermal conductivity and increases the *ZT* value. Furthermore, fabricating nanostructured bulk materials using nanocrystals has become a hot topic in the thermoelectric field for its cost-effectiveness and reliability.[19] Therefore, it is not surprising that well-developed nanocrystal synthesis methods have come together with nanostructured bulk materials in thermoelectric field. Carefully designed nanocrystals, which are the basic elements of nanostructured bulk materials, can adjust the thermoelectric properties of the final bulk

material, which is difficult using ball-milled powders (Figures 1.13 and 1.14).

Generally, organic surfactants are used to control the size growth and determine the shape of inorganic nanocrystals. However, the organic compound remains in the grain boundaries of compacted nanostructured bulk materials and acts as an electrical transport barrier. Therefore, it is important to remove organic surfactants that are attached to the surface of nanocrystals after the synthesis. Various ways of post treatment of nanocrystals, such as using a strong base like hydrazine[20] or super-hydride,[21] heat treatment,[22] plasma treatment,[23] chemical reaction,[18b] and ligand exchange,[24] are well exploited in the surfactant removal process.

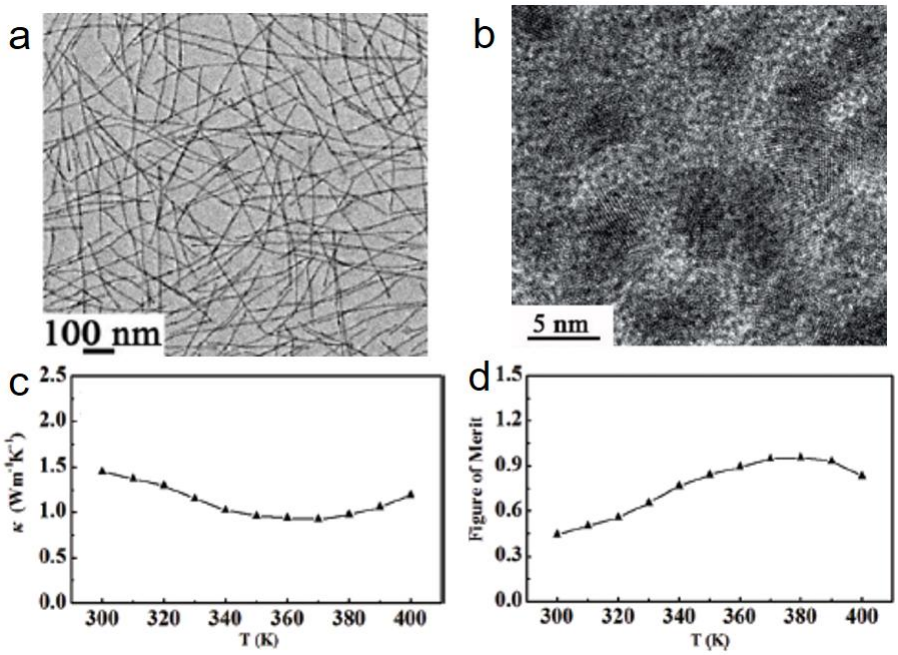

Figure 1.13 (a) TEM image of Bi_2Te_3 nanowires and **(b)** their nanostructured bulk made from SPS. **(c)** The thermal conductivity and **(d)** *ZT* value of Bi_2Te_3 nanostructured bulk. (from Ref. [20a], Zhang, G.; Kirk, B.; Jauregui, L. A.; Yang, H.; Xu, X.; Chen, Y. P.; Wu, Y. *Nano Lett.* **2012**, *12*, 56).

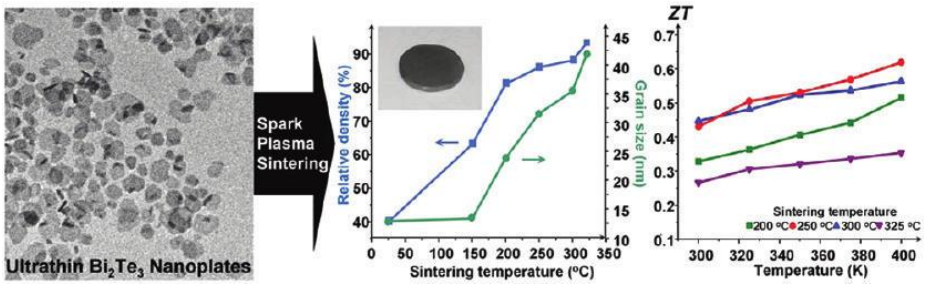

Figure 1.14 Nanostructured bulk of ultrathin Bi_2Te_3 nanoplates by SPS. The samples show grain size-dependent *ZT* values. (from Ref. [18b], Son, J. S.; Choi, M. K.; Han, M.; Park, K.; Kim, J.; Lim, S. J.; Oh, M.; Kuk, Y.; Park, C.; Kim, S.; Hyeon, T. *Nano Lett.* **2012**, *12*, 640).

1.3.4 Doping Nanostructured Bulk Materials using Chemically Synthesized Nanocrystals

There are many examples of reducing lattice thermal conductivity by using nanostructured bulk materials consisted of colloidal nanocrystals. Most of those studies follow a strategy to decrease the thermal conductivity, while maintaining or slightly decreasing electrical conductivity. Interestingly, a few studies report that power factor manipulation is also possible by nanoscale doping using chemically synthesized nanocrystals.[25]

Mehta, *et al*. reported a S-doped nanostructured bulk of pnictogen chalcogenide (Figure 1.15). They observed that the S ions, adsorbed on the surface of nanoplates as surfactants, could be further doped into the lattice which consequently improved the thermoelectric properties. The high power factor and *ZT* value were achieved through a combination of nanostructuring and the surface-induced doping. S-doping plays a key role because S ions act as additional carriers and influence the electrical conductivity and the Seebeck coefficient. This allows us to control the transport properties by selective doping at the surface of the nanocrystals.

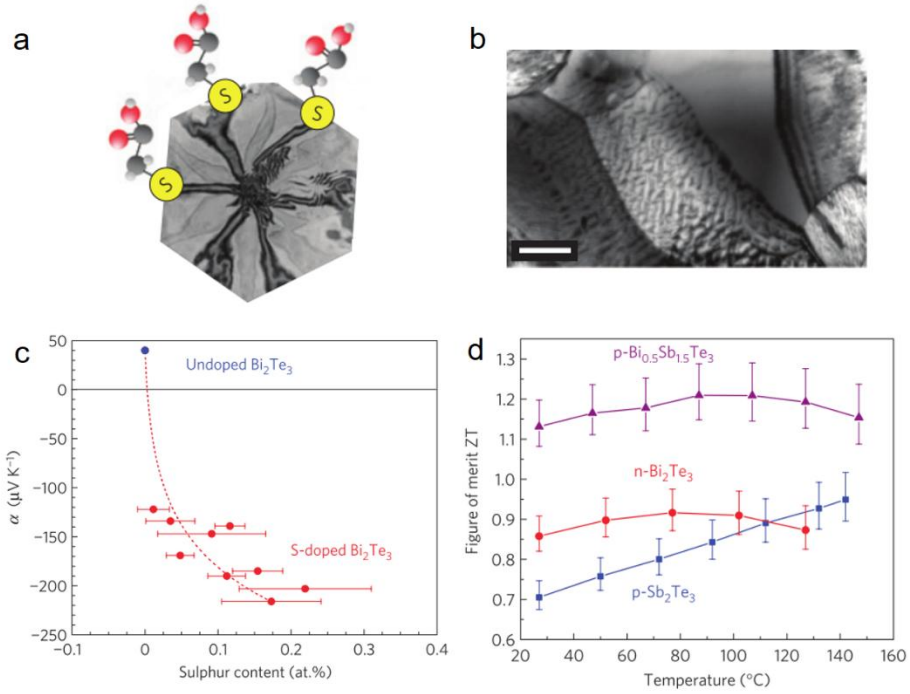

Figure 1.15 (a) Synthesized sulphur-doped nanoplates. **(b)** TEM image of hot-pressed nanostructured bulk showing nanograins and nanopores. **(c)** Seebeck coefficient versus the sulphur content for sulphur-doped and undoped Bi_2Te_3. **(d)** Temperature-dependent *ZT* of an n-type Bi_2Te_3, p-type Sb_2Te_3 and p-type $Bi_{0.5}Sb_{1.5}Te_3$ sintered pellet. (from Ref. [25b], Mehta, R. J.; Zhang, Y.; Karthik, C.; Singh, B.; Siegel, R. W.; Borca-Tasciuc, T.; Ramanath, G. *Nat. Mater.* **2012**, *11*, 233).

1.4 Dissertation Overview

Thermoelectric materials have drawn great attention as novel renewable energy sources. Recent developments of nanotechnology have elevated the thermoelectric conversion efficiency so that application in various field is expected. To date, nanostructuring has been exploited in thermoelectrics, mainly for the reduction of the thermal conductivity, whereas their potential for enhancing the power factor has been neglected. The current dissertation is focused on doped nanostructured bulk materials for thermoelectric enhancement.

The first part (Chapter 2) describes the thermoelectric properties of nanostructured bulk materials consisting of n-type nanostructured La-doped $SrTiO_3$ materials, produced by spark plasma sintering of chemically synthesized colloidal nanocrystals. The La doping levels were varied from 3.0 to 9.0 at% by varying the experimental conditions. An enhanced thermoelectric efficiency was observed and attributed to the large decrease in thermal conductivity, with no significant change in the Seebeck coefficient or electrical conductivity observed. The nanostructured bulk of the La-doped $SrTiO_3$ exhibited a maximum ZT of ~0.37 at 937 K with 9.0 at% La doping, which is one of the highest values reported for doped $SrTiO_3$.

The second part (Chapter 3) describes nanostructuring to improve electrical transport properties. We use nanochemistry to stabilize bulk bismuth telluride (Bi_2Te_3) in a non-equilibrium phase, namely, the phase-pure n-type $K_{0.06}Bi_2Te_{3.18}$. The incorporated potassium and tellurium in Bi_2Te_3 far exceeds their solubility limit, inducing a simultaneous increase in the electrical conductivity and the Seebeck coefficient, along with a decrease in the thermal conductivity. Consequently, a high power factor of ~43 μW cm^{-1} K^{-2} and a high ZT > 1.1 at 323 K were achieved.

1.5 References

[1] a) Bell, L. E. *Science* **2008**, *321*, 1457. b) DiSalvo, F. J. *Science* **1999**, *285*, 703. c) Dresselhaus, M. S.; Chen, G.; Tang, M. Y.; Yang, R. G.; Lee, H.; Wang, D. Z.; Ren, Z. F.; Fleurial, J. P.; Gogna, P. *Adv. Mater.* **2007**, *19*, 1043. d) Tritt, T. M.; Subramanian, M. A. *MRS Bull.* **2006**, *31*, 188.

[2] a) Sootsman, J. R.; Chung, D. Y.; Kanatzidis, M. G. *Angew. Chem. Int. Ed.* **2009**, *48*, 8616. b) Minnich, A. J.; Dresselhaus, M. S.; Ren, Z. F.; Chen, G. *Energy Environ. Sci.* **2009**, *2*, 466.

[3] Snyder, G. J.; Toberer, E. S. *Nat. Mater.* **2008**, *7*, 105.

[4] Tan, G.; Zhao, L. D.; Kanatzidis, M. G. *Chem. Rev.* **2016**, *116*, 12123.

[5] Tritt, T. M. *Annu. Rev. Mater. Res.* **2011**, *41*, 433.

[6] Rowe, D. M., *Thermoelectrics handbook : Macro to Nano*, CRC/Taylor & Francis, Boca Raton, FL, **2006**.

[7] a) Liu, W.; Tan, X.; Yin, K.; Liu, H.; Tang, X.; Shi, J.; Zhang, Q.; Uher, C. *Phys. Rev. Lett.* **2012**, *108*, 166601. b) Pei, Y.; Wang, H.; Snyder, G. J. *Adv. Mater.* **2012**, *24*, 6125. c) Zhang, Q.; Cao, F.; Liu, W.; Lukas, K.; Yu, B.; Chen, S.; Opeil, C.; Broido, D.; Chen, G.; Ren, Z. *J. Am. Chem. Soc.* **2012**, *134*, 10031.

[8] a) Vineis, C. J.; Shakouri, A.; Majumdar, A.; Kanatzidis, M. G. *Adv. Mater.* **2010**, *22*, 3970. b) Biswas, K.; He, J. Q.; Zhang, Q. C.; Wang, G. Y.; Uher, C.; Dravid, V. P.; Kanatzidis, M. G. *Nat. Chem.* **2011**, *3*, 160. c) Biswas, K.; He, J. Q.; Blum, I. D.; Wu, C. I.; Hogan, T. P.; Seidman, D. N.; Dravid, V. P.; Kanatzidis, M. G. *Nature* **2012**, *489*, 414. d) Kim, S. I.; Lee, K. H.; Mun, H. A.; Kim, H. S.; Hwang, S. W.; Roh, J. W.; Yang, D. J.; Shin, W. H.; Li, X. S.; Lee, Y. H.; Snyder, G. J.; Kim, S. W. *Science* **2015**, *348*, 109.

[9] a) Sales, B. C.; Mandrus, D.; Williams, R. K. *Science* **1996**, *272*, 1325. b) Paschen, S.; Carrillo-Cabrera, W.; Bentien, A.; Tran, V. H.;

Baenitz, M.; Grin, Y.; Steglich, F. *Phys. Rev. B* **2001**, *64*, 214404. c) Christensen, M.; Abrahamsen, A. B.; Christensen, N. B.; Juranyi, F.; Andersen, N. H.; Lefmann, K.; Andreasson, J.; Bahl, C. R. H.; Iversen, B. B. *Nat. Mater.* **2008**, *7*, 811. d) Rogl, G.; Grytsiv, A.; Rogl, P.; Peranio, N.; Bauer, E.; Zehetbauer, M.; Eibl, O. *Acta Mater.* **2014**, *63*, 30. e) Prokofiev, A.; Sidorenko, A.; Hradil, K.; Ikeda, M.; Svagera, R.; Waas, M.; Winkler, H.; Neumaier, K.; Paschen, S. *Nat. Mater.* **2013**, *12*, 1096. f) Beekman, M.; Morelli, D. T.; Nolas, G. S. *Nat. Mater.* **2015**, *14*, 1182.

[10] a) Zhao, L. D.; Lo, S. H.; Zhang, Y. S.; Sun, H.; Tan, G. J.; Uher, C.; Wolverton, C.; Dravid, V. P.; Kanatzidis, M. G. *Nature* **2014**, *508*, 373. b) Zhao, L. D.; Tan, G. J.; Hao, S. Q.; He, J. Q.; Pei, Y. L.; Chi, H.; Wang, H.; Gong, S. K.; Xu, H. B.; Dravid, V. P.; Uher, C.; Snyder, G. J.; Wolverton, C.; Kanatzidis, M. G. *Science* **2016**, *351*, 141. c) Wei, T. R.; Tan, G.; Zhang, X.; Wu, C. F.; Li, J. F.; Dravid, V. P.; Snyder, G. J.; Kanatzidis, M. G. *J. Am. Chem. Soc.* **2016**, *138*, 8875.

[11] Liu, H. L.; Shi, X.; Xu, F. F.; Zhang, L. L.; Zhang, W. Q.; Chen, L. D.; Li, Q.; Uher, C.; Day, T.; Snyder, G. J. *Nat. Mater.* **2012**, *11*, 422.

[12] a) Nolas, G. S.; Poon, J.; Kanatzidis, M. G. *MRS Bull.* **2006**, *31*, 199. b) Zhao, L. D.; Berardan, D.; Pei, Y. L.; Byl, C.; Pinsard-Gaudart, L.; Dragoe, N. *Appl. Phys. Lett.* **2010**, *97*, 092118.

[13] a) Hicks, L.; Dresselhaus, M. S. *Phys. Rev. B: Condens. Matter Mater. Phys.* **1993**, *47*, 12727. b) Hicks, L.; Dresselhaus, M. S. *Phys. Rev. B: Condens. Matter Mater. Phys.* **1993**, *47*, 16631.

[14] Venkatasubramanian, R.; Siivola, E.; Colpitts, T.; O'Quinn, B. *Nature* **2001**, *413*, 597.

[15] a) Hochbaum, A. I.; Chen, R. K.; Delgado, R. D.; Liang, W. J.; Garnett, E. C.; Najarian, M.; Majumdar, A.; Yang, P. D. *Nature* **2008**, *451*, 163. b) Boukai, A. I.; Bunimovich, Y.; Tahir-Kheli, J.; Yu, J.; Goddard III, W. A.; Heath, J. R. *Nature* **2008**, *451*, 168.

[16] a) Hsu, K. F.; Loo, S.; Guo, F.; Chen, W.; Dyck, J. S.; Uher, C.; Hogan, T.; Polychroniadis, E. K.; Kanatzidis, M. G. *Science* **2004**, *303*, 818. b) Androulakis, J.; Lin, C.; Kong, H.; Uher, C.; Wu, C.; Hogan, T.; Cook, B. A.; Caillat, T.; Paraskevopoulos, K. M.; Kanatzidis, M. G. *J. Am. Chem. Soc.* **2007**, *129*, 9780. c) He, J. Q.; Zhao, L. D.; Zheng, J. C.; Doak, J. W.; Wu, H. J.; Wang, H. Q.; Lee, Y.; Wolverton, C.; Kanatzidis, M. G.; Dravid, V. P. *J. Am. Chem. Soc.* **2013**, *135*, 4624. d) Zeier, W. G.; Zevalkink, A.; Gibbs,

Z. M.; Hautier, G.; Kanatzidis, M. G.; Snyder, G. J. *Angew. Chem. Int. Ed.* **2016**, *55*, 6826. e) Ma, J.; Delaire, O.; May, A. F.; Carlton, C. E.; McGuire, M. A.; VanBebber, L. H.; Abernathy, D. L.; Ehlers, G.; Hong, T.; Huq, A.; Tian, W.; Keppens, V. M.; Shao Horn, Y.; Sales, B. C. *Nat. Nanotech.* **2013**, *8*, 445.

[17] a) Heremans, J. P.; Jovovic, V.; Toberer, E. S.; Saramat, A.; Kurosaki, K.; Charoenphakdee, A.; Yamanaka, S.; Snyder, G. J. *Science* **2008**, *321*, 554. b) Ahmad, S.; Mahanti, S. D.; Hoang, K.; Kanatzidis, M. G. *Phys. Rev. B* **2006**, *74*, 155205. c) Jovovic, V.; Thiagarajan, S. J.; Heremans, J. P.; Komissarova, T.; Khokhlov, D.; Nicorici, A. *J. Appl. Phys.* **2008**, *103*, 053710.

[18] a) Poudel, B.; Hao, Q.; Ma, Y.; Lan, Y. C.; Minnich, A.; Yu, B.; Yan, X. A.; Wang, D. Z.; Muto, A.; Vashaee, D.; Chen, X. Y.; Liu, J. M.; Dresselhaus, M. S.; Chen, G.; Ren, Z. F. *Science* **2008**, *320*, 634. b) Son, J. S.; Choi, M. K.; Han, M. K.; Park, K.; Kim, J. Y.; Lim, S. J.; Oh, M.; Kuk, Y.; Park, C.; Kim, S. J.; Hyeon, T. *Nano Lett*. **2012**, *12*, 640. c) Son, J. S.; Park, K.; Han, M. K.; Kang, C.; Park, S. G.; Kim, J. H.; Kim, W.; Kim, S. J.; Hyeon, T. *Angew. Chem.* **2011**, *50*, 1363. d) Ma, Y.; Hao, Q.; Poudel, B.; Lan, Y.; Yu, B.; Wang, D.; Chen, G.; Ren, Z. *Nano Lett*. **2008**, *8*, 2580. e) Joshi,

G.; Lee, H.; Lan, Y.; Wang, X.; Zhu, G.; Wang, D.; Gould, R. W.; Cuff, D. C.; Tang, M. Y.; Dresselhaus, M. S.; Chen, G.; Ren, Z. *Nano Lett*. **2008**, *8*, 4670. f) Yan, X. A.; Poudel, B.; Ma, Y.; Liu, W. S.; Joshi, G.; Wang, H.; Lan, Y. C.; Wang, D. Z.; Chen, G.; Ren, Z. F. *Nano Lett.* **2010**, *10*, 3373.

[19] a) Zhang, G. Q.; Wang, W.; Li, X. G. *Adv. Mater.* **2008**, *20*, 3654. b) Liu, W. S.; Zhang, Q. Y.; Lan, Y. C.; Chen, S.; Yan, X.; Zhang, Q.; Wang, H.; Wang, D. Z.; Chen, G.; Ren, Z. F. *Adv. Energy Mater.* **2011**, *1*, 577. c) Fan, F. J.; Yu, B.; Wang, Y. X.; Zhu, Y. L.; Liu, X. J.; Yu, S. H.; Ren, Z. *J. Am. Chem. Soc.* **2011**, *133*, 15910. d) Scheele, M.; Oeschler, N.; Veremchuk, I.; Peters, S. O.; Littig, A.; Kornowski, A.; Klinke, C.; Weller, H. *Acs Nano* **2011**, *5*, 8541.

[20] a) Zhang, G. Q.; Kirk, B.; Jauregui, L. A.; Yang, H. R.; Xu, X. F.; Chen, Y. P.; Wu, Y. *Nano Lett*. **2012**, *12*, 56. b) Zhang, G. Q.; Fang, H. Y.; Yang, H. R.; Jauregui, L. A.; Chen, Y. P.; Wu, Y. *Nano Lett*. **2012**, *12*, 3627.

[21] He, M.; Kravchyk, K.; Walter, M.; Kovalenko, M. V. *Nano Lett*. **2014**, *14*, 1255.

[22] Urban, J. J.; Talapin, D. V.; Shevchenko, E. V.; Kagan, C. R.; Murray, C. B. *Nat. Mater.* **2007**, *6*, 115.

[23] Nag, A.; Kovalenko, M. V.; Lee, J. S.; Liu, W.; Spokoyny, B.; Talapin, D. V. *J. Am. Chem. Soc.* **2011**, *133*, 10612.

[24] Son, J. S.; Zhang, H.; Jang, J.; Poudel, B.; Waring, A.; Nally, L.; Talapin, D. V. *Angew. Chem.* **2014**, *53*, 7466.

[25] a) Jood, P.; Mehta, R. J.; Zhang, Y. L.; Peleckis, G.; Wang, X. L.; Siegel, R. W.; Borca-Tasciuc, T.; Dou, S. X.; Ramanath, G. *Nano Lett*. **2011**, *11*, 4337. b) Mehta, R. J.; Zhang, Y. L.; Karthik, C.; Singh, B.; Siegel, R. W.; Borca-Tasciuc, T.; Ramanath, G. *Nat. Mater.* **2012**, *11*, 233. c) Mehta, R. J.; Zhang, Y. L.; Zhu, H.; Parker, D. S.; Belley, M.; Singh, D. J.; Ramprasad, R.; Borca-Tasciuc, T.; Ramanath, G. *Nano Lett.* **2012**, *12*, 4523.

Chapter 2. Enhancement of Thermoelectric Efficiency in Nanostructured Bulk of La-doped $SrTiO_3$

2.1 Introduction

Thermoelectric materials have long attracted a great deal of attention because of their ability to directly interconvert heat and electricity, which allows them to be used as environmentally friendly cooling devices and renewable power generators.[1] Despite these fascinating features, thermoelectric materials have limited applications, mostly because of their low efficiency. The thermoelectric efficiency is quantified as a dimensionless figure-of-merit $ZT = (\sigma S^2/\kappa)T$, where σ is the electrical conductivity, S is the Seebeck coefficient, κ is the thermal conductivity, and T is the absolute temperature. During the past decades, there have been significant efforts to discover high-ZT materials; however, only minimal ZT enhancements have been reported.[2] Recently, the introduction of nanostructures to thermoelectric materials has successfully improved the ZT to higher than 1, since these nanostructures reduce the lattice thermal conductivity while preserving

the electrical conductivity and Seebeck coefficient.[3] Specifically, sintering nanoparticles to fabricate nanostructured bulk materials has been recognized as one of the most effective ways to produce high-*ZT* materials on large scales, which will allow them to be readily employed for commercial thermoelectric devices.[4]

Although various nanostructured materials based on chalcogenides of bismuth and lead have exhibited high *ZT* values, their practical uses have been limited to low-temperature applications in cooling devices, because their low melting points lead to the growth of nanosized grains at high operating temperatures, resulting in the loss of their nanostructural characteristics. Furthermore, these chalcogenide materials are easily oxidized under air at high temperatures, which decreases their thermoelectric efficiency. On the other hand, oxide thermoelectric materials have been known for their good stability at high temperatures as well as their low cost and ease of large-scale production.[5] In particular, the high-temperature stability of oxide materials allows large temperature differences to be maintained within devices, which makes it possible to achieve high conversion efficiencies in spite of their relatively low *ZT* values. Consequently, oxide thermoelectric materials can be considered as the suitable

materials for energy harvesting from hot sources like power plants. To date, various oxide thermoelectric materials have been reported, including the p-type materials, $Ca_3Co_4O_9$[6] and $NaCo_2O_4$,[7] and the n-type materials, electron-doped ZnO,[8] $CaMnO_3$,[9] and $SrTiO_3$.[10–12]

$SrTiO_3$ is a perovskite oxide with a high melting point that exhibits high electrical conductivity upon doping with an electron donor. Undoped $SrTiO_3$ is a band insulator with no d electrons; however, metallic behavior appears upon doping with a small amount of La.[13] Electron-doped $SrTiO_3$ has a large figure-of-merit not only because of its relatively high electrical conductivity but also because of the large Seebeck coefficient induced by its high carrier mobility and large effective mass.[11a,b] A single crystal of bulk La-doped $SrTiO_3$ showed a high power factor of 28–36 $\mu W\ cm^{-1}\ K^{-2}$ at room temperature,[11b] which is comparable to the power factors of Bi_2Te_3 compounds.[1a] Although its *ZT* is less than 1 because of its large thermal conductivity, La-doped $SrTiO_3$ is one of the best n-type oxide thermoelectric materials.[5] Herein we report on n-type nanostructured bulk La-doped $SrTiO_3$ produced by spark plasma sintering (SPS) of chemically synthesized nanoparticles. Furthermore, nanostructured bulk La-doped $SrTiO_3$ materials with various La doping levels were successfully

obtained by adjusting the synthetic conditions, and their thermoelectric properties were systematically investigated.

2.2 Experimental Section

2.2.1 Chemicals

Strontium nitrate was purchased from Chameleon Chemical Reagent. Lanthanum nitrate hexahydrate (99.99%), tetramethylammonium hydroxide (TMAH, 25 wt. % in water), oleic acid (90%), and acetic acid (99.7%) were purchased from Aldrich Chemical Company. Dihydroxybis(ammonium lactato)titanium (TALH, 50 wt. % in water) was purchased from Alfa Aesar.

2.2.2. Synthesis of La-doped $SrTiO_3$ Nanoparticles

La-doped $SrTiO_3$ nanoparticles were synthesized on the multi-gram scale using a conventional hydrothermal method that has been widely used to synthesize various nanocrystals of titanates.[14] In a typical large-scale synthesis, based on 3.1% La-doped $SrTiO_3$, 7.125 mmol of strontium nitrate and 0.375 mmol of lanthanum nitrate hexahydrate were dissolved in 26 mL of deionized water. Then, 7.5 mmol of dihydroxybis(ammonium lactato)titanium (TALH) and 10 mmol of oleic acid were added to the solution, followed by stirring 30 min. 24

mL of tetramethylammonium hydroxide (TMAH) solution was added dropwise to the reaction mixture. The resulting milky solution was readily transferred to a 100 mL Teflon-lined stainless steel autoclave sealed, maintained at 200 ^{o}C for 20 h. The product was collected by centrifugation and washed several times with ethanol and deionized water. To eliminate strontium byproduct, $SrCO_3$, as-prepared La-doped $SrTiO_3$ powder was washed with diluted (5%) acetic acid and washed again with deionized water.[21] The resulting product was dried and kept for further experiments.

2.2.3 Nanostructured Bulk Fabrication

Before fabrication of nanostructured pellet, La-doped $SrTiO_3$ nanocrystals were sintered in air at 500 °C for 5 h to remove the organic surfactant coating on the surface of nanoparticles. La-doped $SrTiO_3$ nanostructured bulk material was fabricated by spark plasma sintering (SPS). Powdery nanocrystal was pressed into a pellet under a pressure of 30 MPa and a vacuum environment. The sintering temperature was controlled from room temperature to 1400 °C at a heating rate of 100 °C /min, and held at desired temperature for 5 min. After sintering, a disk-shaped pellet with a diameter of 12.7 mm and a thickness of 3 mm was obtained.

2.2.4 Sample Characterization and Thermoelectric Properties Measurement

The La-doped $SrTiO_3$ nanocrystals were characterized by the transmission electron microscopy (TEM), scanning electron microscopy (SEM), electron diffraction (ED), X-ray diffraction (XRD), X-ray photoelectron spectroscopy (XPS), energy-dispersive X-ray spectroscopy (EDS), and elemental analysis. The TEM images and ED patterns were collected on a JEOL JEM-2010 electron microscope. The SEM images and EDX result were collected on a JEOL JSM-6701F scanning electron microscope. The powder XRD patterns were obtained with a Rigaku D/Max-3C diffractometer equipped with a rotating anode and a Cu Kα radiation source (λ= 0.15418 nm) and Riveld refinement was conducted with Jade 6.0 software (Materials Data Incoporated). The XPS data were obtained with Thermo Scientific Sigma Probe spectrometer. Elemental analysis was performed by using ICP-AES (JP/ICPS-7500, Shimdzu) and a CHNS analyzer (CHNS-932, LECO Corp).

The electrical conductivity and the Seebeck coefficient was measured by a static dc method based on the slope of the voltage versus the temperature-difference curves using commercial equipment (ZEM-3,

Ulvac-Riko) under a low-pressure helium atmosphere. The carrier concentration and the mobility were measured by a Hall measurement system (HL5500PC, BIO-RAD) at room temperature in the air. The thermal conductivity was calculated using thermal diffusivity, specific heat capacity, and density. The thermal diffusivity was measured by a laser flash analysis (LFA 457, Netzsch) on the disk-shaped pellets. The specific heat capacity was measured using a differential scanning calorimeter (DSC 204 F1, Netzsch).

2.3 Results and Discussion

2.3.1 La-doped $SrTiO_3$ Nanoparticles

The transmission electron microscopy (TEM) image (Figure 2.1a) and scanning electron microscopy (SEM) image (Figure 2.1b) show nanoparticles with sizes of 10–20 nm. The lattice fringes of 0.27 nm shown in the high-resolution TEM image (Figure 2.1c) correspond to typical (110) facets of cubic perovskite $SrTiO_3$, and the electron diffraction (ED) pattern (Figure 2.1d) confirmed the highly crystalline nature of the nanoparticles. Size distribution analysis showed that variations in the La content had no evident influence on the shape or size of the LSTO nanoparticles (Figure 2.2). To investigate the actual

doping content, elemental analysis of the La-doped $SrTiO_3$ nanoparticles was performed using energy-dispersive X-ray spectroscopy (EDS, Figure 2.3), X-ray photoelectron spectroscopy (XPS, Figure 2.4), and inductively coupled plasma atomic emission spectroscopy (ICP-AES, Table 2.1). ICP-AES analysis showed that the amount of La precursor in the reaction mixture was directly related to the doping level. The XRD patterns of the La-doped $SrTiO_3$ nanoparticles in Figure 2.5a show that they have cubic $SrTiO_3$ (JCPDS 35–0734) structures at all La doping levels.

The particle size estimated from the XRD patterns using the Scherrer equation was found to be ~15 nm, which is consistent with the TEM data. To investigate the effect of the doping level on the crystal structure, Rietveld refinement was conducted on the X-ray diffraction data. We found that continuous shrinkage of the unit cell volume occurred with increasing dopant concentration (Figure 2.5b), which can be explained by the replacement of the larger-sized Sr^{2+} ions (118 pm) in the A-sites of the perovskite structure with the smaller La^{3+} ions (103.2 pm).

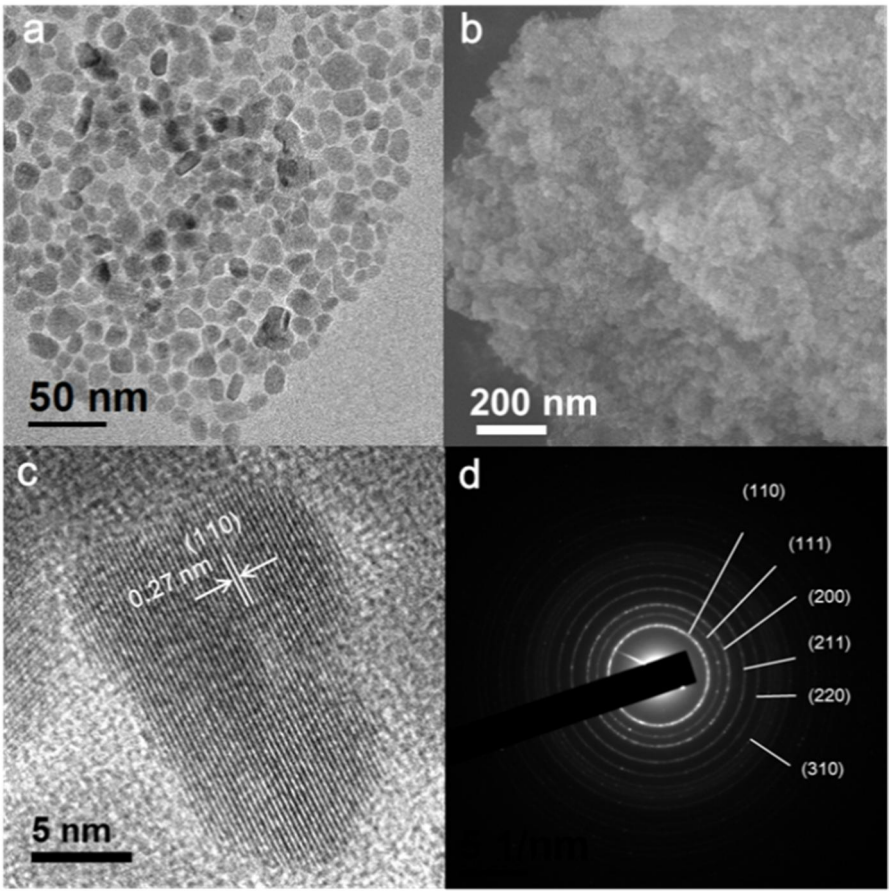

Figure 2.1. (a) TEM image, **(b)** SEM image, **(c)** HRTEM image, and **(d)** electron diffraction pattern of $SrTiO_3$ nanoparticles with 7.7% La doping

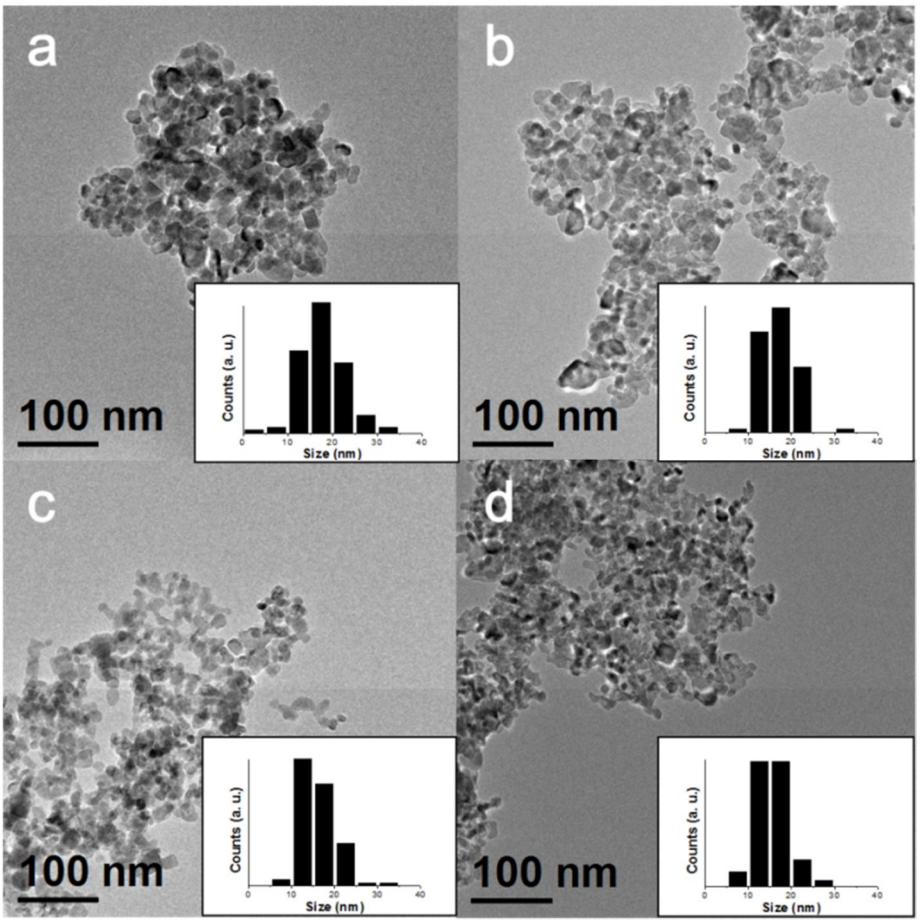

Figure 2.2. TEM images of synthesized $SrTiO_3$ doped with **(a)** 3.1%, **(b)** 4.7%, **(c)** 7.7%, and **(d)** 9.0% La. Insets show the size distribution histograms which were collected by measuring the sizes of randomly selected 200 particles.

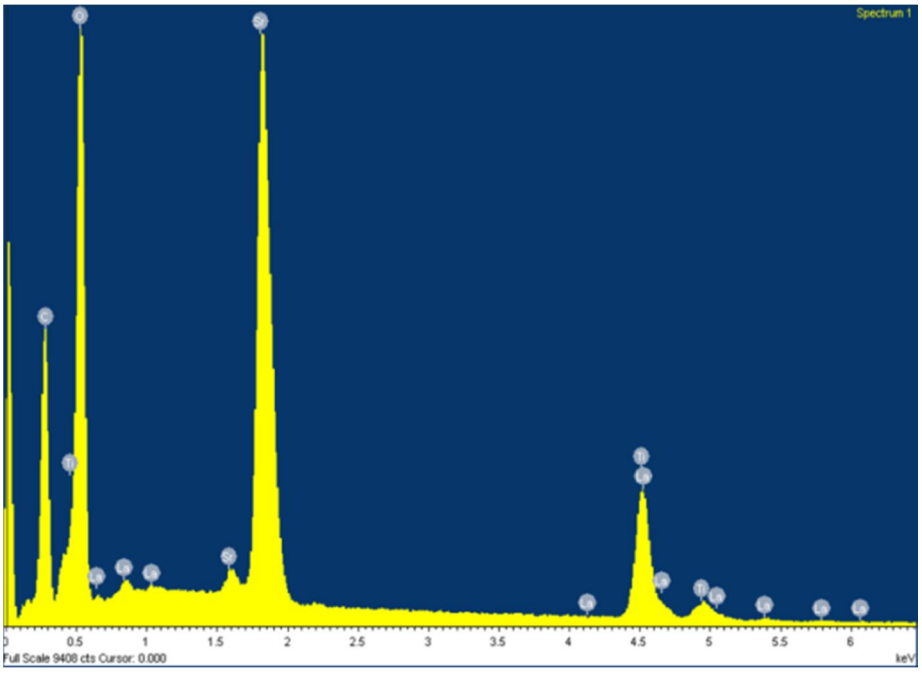

Figure 2.3. Energy-dispersive X-ray spectroscopy (EDS) of 9.0% La-doped $SrTiO_3$ nanoparticles.

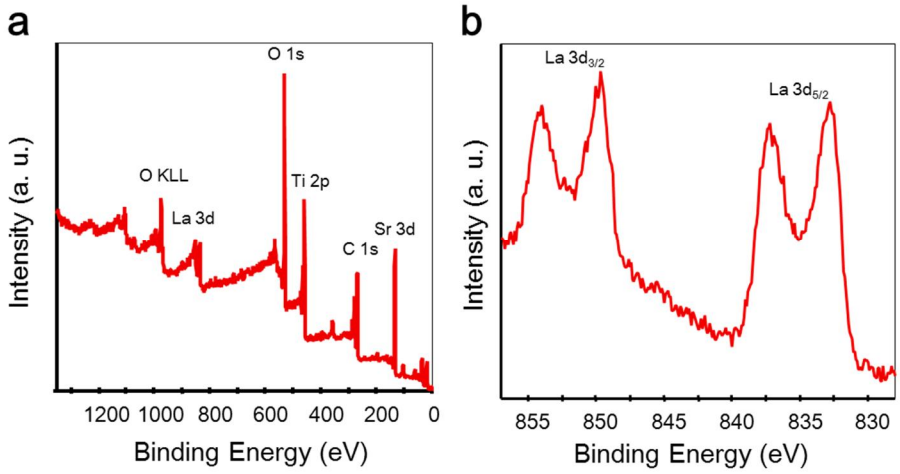

Figure 2.4. X-ray photoelectron spectroscopy (XPS) of 9.0% La-doped $SrTiO_3$ nanoparticles.

Initial concentration of $La(NO_3)_3 \cdot 6H_2O$ relative to TALH	Doped La concentration confirmed by ICP-AES
5	3.1
8	4.7
10	7.7
12	9.0

Table 2.1. ICP-AES analysis of synthesized La-doped $SrTiO_3$ nanoparticles with different metal precursor ratios (atomic %).

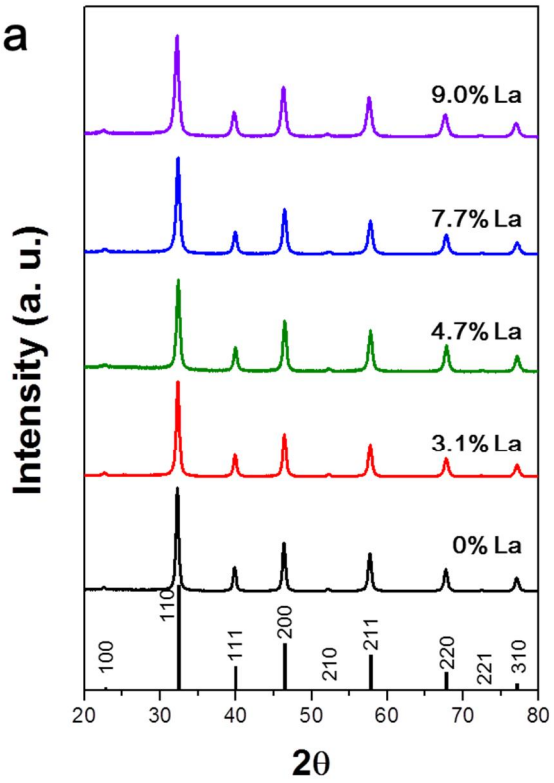
a
9.0% La
7.7% La
4.7% La
3.1% La
0% La
Intensity (a. u.)
100
110
111
200
210
211
220
221
310
20
30
40
50
60
70
80
2θ

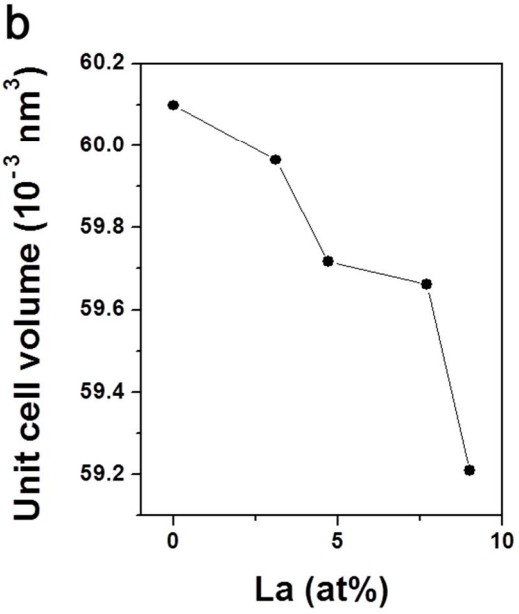
b
Unit cell volume (10-3 nm3)
60.2
60.0
59.8
59.6
59.4
59.2
0
5
10
La (at%)

Figure 2.5. (a) X-ray diffraction pattern of La-doped $SrTiO_3$. The vertical lines indicate the reference pattern of $SrTiO_3$ (JPCD 35-0734). **(b)** Unit cell volume derived from the Rietveld lattice parameter refinement plotted as a function of La content.

2.3.2 Synthetic Mechanism of La-doped $SrTiO_3$

While synthesizing the La-doped $SrTiO_3$ nanoparticles, we found two particular reaction parameters to be important for obtaining high-quality nanoparticles: the concentration of oleic acid surfactant and the base concentration. When the reaction was conducted without oleic acid, severely aggregated particles with relatively large sizes were obtained (Figure 2.6). With increasing oleic acid concentration, the size of the particles became gradually smaller and more uniform. The base concentration of the solution was also critical in the synthesis of nanocrystals. According to the synthetic mechanism,[15] in the presence of base, the Ti precursor is readily transformed into a titanium dioxide gel that has poor solubility in water. Subsequently, the La and Sr species diffuse into the Ti gel during the hydrothermal reaction, and the nanoparticles are generated as the temperature increases. In the current synthesis, an optimal amount of base is required to form $SrTiO_3$ nanoparticles, because the crystallization rate depends on the base concentration. When the synthesis was performed with a TMAH concentration lower than 0.66 M, no crystalline particles were formed. For example, at a TMAH concentration of 0.6 M, a mixture of amorphous TiO_2 and by-products of Sr and La were generated (Figure

2.6c). As the base concentration increased, highly crystalline La-doped $SrTiO_3$ nanoparticles were successfully produced. We used a TMAH concentration of 1.32 M because the nanoparticles synthesized with concentrations of 1.32 M or higher were nearly identical.

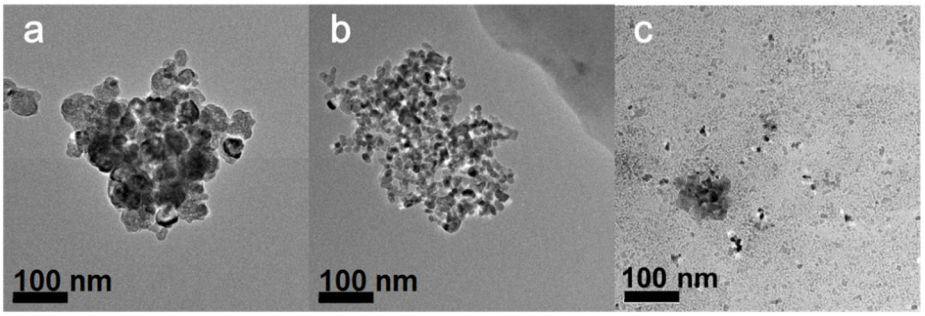

Figure 2.6. TEM images of 3.1% La-doped $SrTiO_3$ synthesized with **(a)** no oleic acid, **(b)** 20 mmol of oleic acid, and **(c)** 0.6 M TMAH.

2.3.3 Preparation of Bulk Nanostructured Pellets

To measure the thermoelectric properties, we prepared bulk nanostructured pellets by sintering the as-synthesized La-doped $SrTiO_3$ nanoparticles using the SPS process. Large-scale synthesis of nanoparticles enables consolidating them into a pellet and measuring the thermoelectric properties (Figure 2.7). SPS is advantageous for consolidating nanoparticles because it requires only a short holding time at high temperature, which can inhibit undesired grain growth. Before the sintering process, organic surfactants, which can reduce the electrical conductivity by acting as insulating barriers, were removed by heat treatment under air at 500 °C. During the heat treatment process, the size and shape of the nanoparticles was nearly unchanged because of the very high melting point (~1500 °C) of the La-doped $SrTiO_3$ nanoparticles, which is a typical characteristic of perovskites. After the surfactant removal process, La-doped $SrTiO_3$ nanoparticles were consolidated by SPS into a pellet of 12.7 mm in diameter and 3 mm in thickness (Figure 2.8). The density and the grain size of the nanostructured bulk pellet were affected by the sintering temperature at the sustained axial pressure of 30 MPa (Table 2.2). The pellets sintered at the low temperatures of <600 °C had only 38% of the theoretical

density of bulk La-doped $SrTiO_3$, and the grain size of the pellet was similar to the size of the nanoparticles. And the measured electrical conductivity of the pellet was too low to exhibit any significant thermoelectric efficiency. As the sintering temperature increased, the density and the grain size of the pellet gradually increased, and the electrical conductivity also increased. At the sintering temperature of 1400 °C, a relative density of 92% and a calculated grain size of 69 nm were achieved, which resulted in the maximum obtained electrical conductivity. A typical SEM image of the nanostructured bulk La-doped $SrTiO_3$ sintered at 1400 °C was consistent with the grain size calculated from the XRD pattern (Figure 2.9). Consequently, the sintering temperature was fixed at 1400 °C in order to obtain a high relative density and electrical conductivity.

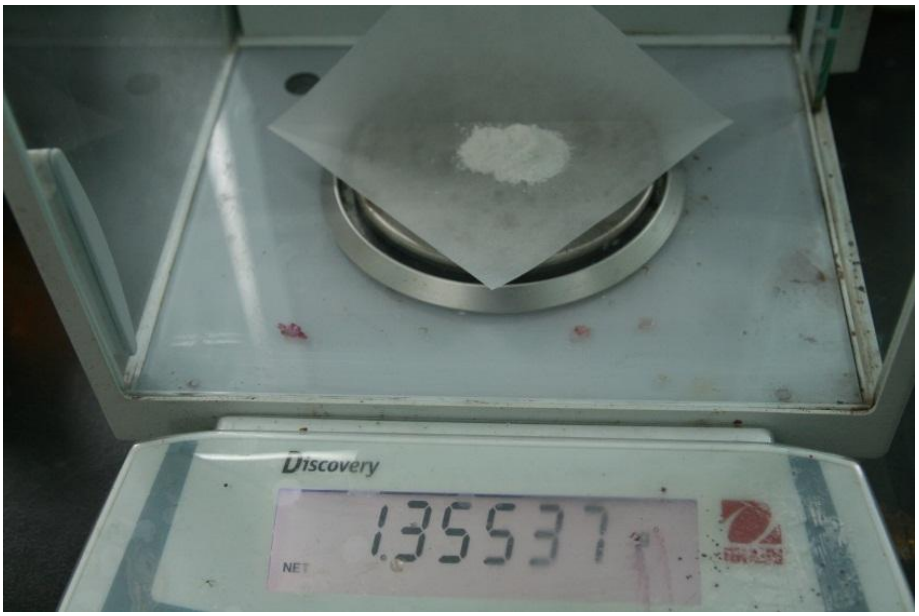

Figure 2.7. A photograph showing 1.35g of La-doped $SrTiO_3$ nanoparticles treated surfactant-removal process.

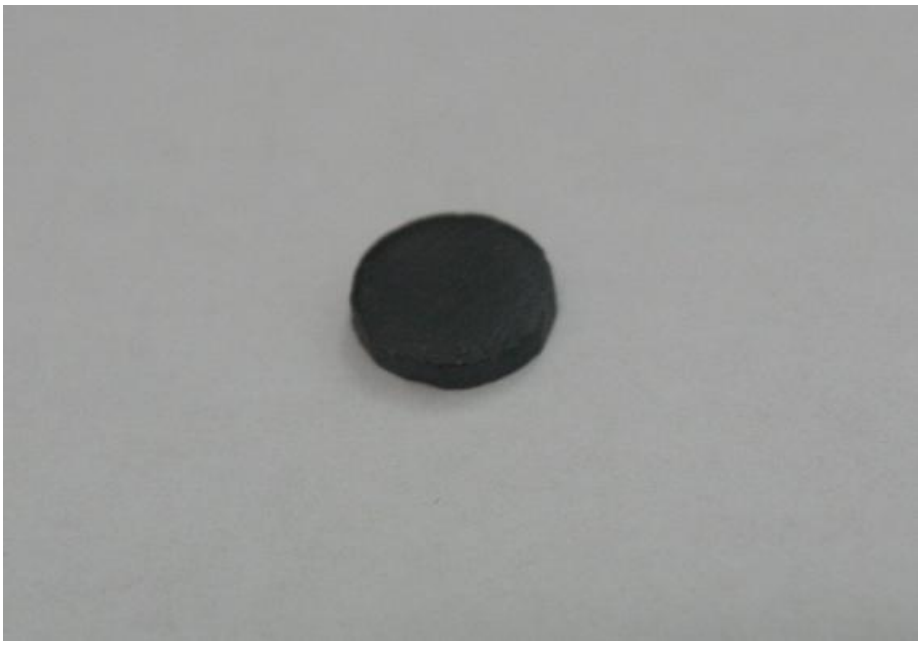

Figure 2.8. A photograph showing La-doped $SrTiO_3$ nanostructured bulk pellet (9.0% La) prepared by SPS.

Temperature (℃)	Density (g/cm^3)	Grain size (nm)
400	2 (38%)[a]	16
600	2 (38%)	16
800	2.3 (45%)	20
1000	4.3 (83%)	26
1200	4.6 (88%)	34
1300	4.7 (90%)	50
1400	4.8 (92%)	69

Table 2.2. Sintering temperature dependent density and grain size of nanostructured bulk La-doped $SrTiO_3$. [a]The relative density (%T.D.) are shown on the table.

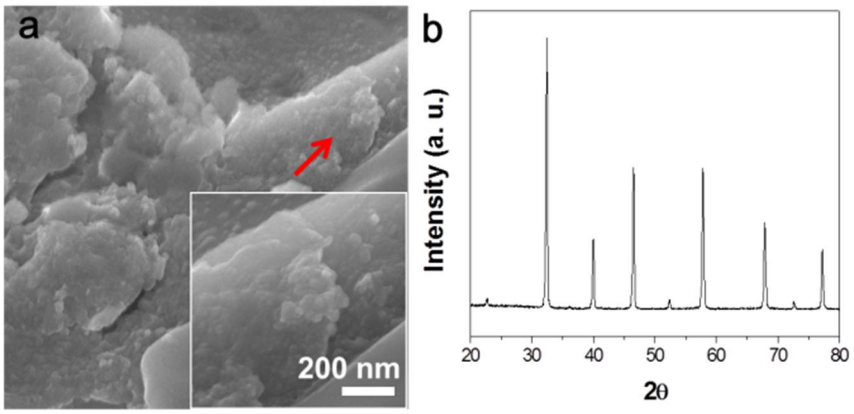

Figure 2.9. (a) SEM image, and **(b)** XRD pattern of nanostructured bulk La-doped $SrTiO_3$ with 9.0% La doping sintered at 1400 °C.

2.3.4 Thermoelectric Properties of Nanostructured La-doped $SrTiO_3$

2.3.4.1 Electrical Conductivity

The electrical conductivity (σ) of nanostructured bulk La-doped $SrTiO_3$ materials with various La doping levels was measured as a function of temperature from 323 K to 973 K (Figure 2.10a). Bulk La-doped $SrTiO_3$ is known to exhibit a negative correlation between temperature and electrical conductivity.[11] At the high temperatures above 500 K, the electrical conductivity of La-doped $SrTiO_3$ decreased in proportion to T^{-2} at all doping levels, indicating that phonon scattering was the dominant mechanism above that temperature.[16] At the low doping levels (3.1 and 4.7 at%), the electrical properties followed the general metallic behavior. However, in the sample with the higher doping level of 7.7 at%, the electrical conductivity started to decrease below 500 K. Furthermore, in the sample with highest doping level of 9.0 at%, the electrical conductivity near room temperature dropped suddenly, and the material unexpectedly became semiconductor-like.

To understand these unexpected behaviors, we measured the electron concentration and mobility using a Hall measurement system (Figure

2.10b). The electrical conductivity (σ) satisfies the equation, $\sigma = en\mu$ where e is the electron charge, n is the electron concentration, and μ is the carrier mobility. As shown in the graph, the electron concentration gradually increased from 2.8×10^{19} cm^{-3} to 1.5×10^{20} cm^{-3} with increasing La doping concentration at room temperature. This confirms that the La dopant ionized fairly well at all doping levels. On the other hand, when the doping concentration was higher than 4.7 at%, the mobility sharply decreased, which is responsible for the decrease in electrical conductivity at low temperatures. We think this reduction of the carrier mobility is originated from structural distortion by the doping. In perovskite system, it has been shown that La doping in A-site relax oxygen octahedra, leading to the supressed stability of ABO_3 perovskite structure.[17] At electron concentration of ~ 10^{20} cm^{-1}, t_{2g} and e_g orbitals of Ti^{3+} ion 3d electron overlaps the Fermi level of doped $SrTiO_3$.[18] Therefore, with the increase of La dopant, more structural distortion happens and that induces changes of Fermi level energy states. This structural distortion induced localized states is often observed in polycrystalline and nanocrystalline materials rather than single bulk crystal because the reducing the size of crystal accelerates the structural distortion.[19] However, with the increase of the

temperature the electrical conductivity of the heavily doped $SrTiO_3$ seemed to follow the general metallic behavior, since charge carrier concentration increases and thus phonon-electron interaction dominates the carrier transport at high temperature.

2.3.4.2 Seebeck Coefficient

The Seebeck coefficients (*S*) of samples with various doping levels were found to range from –80 to –300 μV K^{-1} at all temperatures; these values are consistent with those previously reported for bulk La-doped $SrTiO_3$ (Figure 2.10c).[11a] Negative Seebeck coefficients indicate that the samples have n-type character. The La doping level was closely correlated with the Seebeck coefficient as well as with the electrical conductivity. Furthermore, we theoretically calculated the Seebeck coefficient for comparison with the experimental results. We assumed parabolic bands, so the Seebeck coefficient could be expressed as

$$S = -\frac{k_B}{e}\left(\frac{(r+2)F_{r+1}(\eta)}{(r+1)F_r(\eta)} - \eta\right) \qquad \text{(Eq. 2.1)}$$

where k_B is the Boltzmann constant, r is the scattering parameter of the relaxation time, η is the reduced chemical potential (μ/k_BT), and Fr is the Fermi integral,

$$F_r(\eta) = \int_0^\infty \frac{x^r}{1+e^{x-\eta}} dx \qquad \text{(Eq. 2.2)}$$

The Fermi integral is related to the carrier concentration by

$$n = 4\pi \left(\frac{2m^* k_B T}{h^2}\right)^{3/2} F_{1/2}(\eta) \qquad \text{(Eq. 2.3)}$$

where m^* is the effective mass and h is the Planck constant. We assumed that m^* has the same value as that in the case of the La-doped $SrTiO_3$ bulk.[11b] We also assumed that the acoustic phonon-electron interaction is the dominant scattering mechanism and that the scattering parameter of relaxation time becomes zero (r = 0).[16] The calculated results are shown as the dashed lines in Figure 2.10c. The measured Seebeck coefficients match very well with the calculated data at all temperatures, indicating that other scattering mechanisms including those occurring at partially ionized or neutral impurities or at the nanoscale interfaces of the nanostructured bulk were absent.[20]

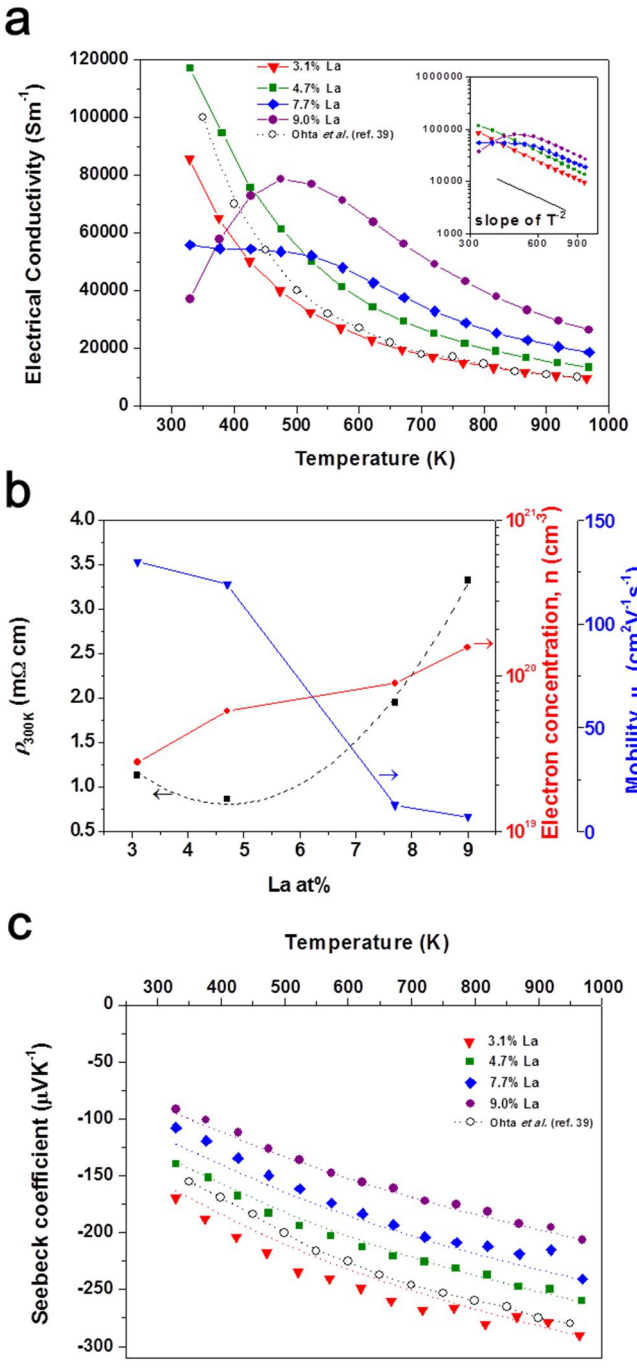
a
Electrical Conductivity (Sm^{-1})
Temperature (K)
3.1% La
4.7% La
7.7% La
9.0% La
Ohta et al. (ref. 39)
slope of T^{-2}
b
ρ_{300K} (mΩ cm)
Electron concentration, n (cm^{-3})
Mobility, μ_e (cm^{2}V^{-1}s^{-1})
La at%
c
Temperature (K)
Seebeck coefficient (μVK^{-1})
3.1% La
4.7% La
7.7% La
9.0% La
Ohta et al. (ref. 39)

Figure 2.10. Temperature dependence of **(a)** electrical conductivity (σ), and **(c)** Seebeck coefficient (S) of La-doped $SrTiO_3$ samples with various La doping levels. Inset shows that σ decreases in proportion to T^{-2}. **(b)** Plots of room-temperature resistivity (black), electron concentration (red), and mobility (blue) of La-doped $SrTiO_3$ as a function of La content.

2.3.4.3 Thermal Conductivity

The thermal diffusivity, specific heat capacity, and geometric density were measured so that the total thermal conductivity (κ) could be plotted as a function of temperature (Figure 2.11a). The thermal conductivity is directly correlated with the dopant concentration, because the doped impurity atoms can act as scattering sites disturbing the phonon conduction. The total thermal conductivity consists of the contributions of the lattice thermal conductivity (κ_L) and the electronic thermal conductivity (κ_e), i.e., $\kappa = \kappa_L + \kappa_e$. To obtain the lattice thermal conductivity, we first calculated the electronic thermal conductivity using the Wiedemann-Franz law, $\kappa/\sigma=LT$, where L is the Lorenz number (2.44×10^{-8} V^2 K^{-2} for the degenerate semiconductor system), and then we subtracted it from the total thermal conductivity. The temperature dependence of the lattice thermal conductivity is shown in Figure 2.11b. The 9.0 at% La-doped $SrTiO_3$ exhibits κ_L ~4.5 W m^{-1} K^{-1} at room temperature, and its κ_L decreased to the lowest value of ~2.3 W m^{-1} K^{-1} at 973 K, which is ~25% less than that reported for a La-doped $SrTiO_3$ single crystal.[11a] This decrease in the lattice thermal conductivity was induced by scattering events at the grain boundaries of the nanostructured bulk, as has been shown in other nanostructured

bulk materials.[2a,4]

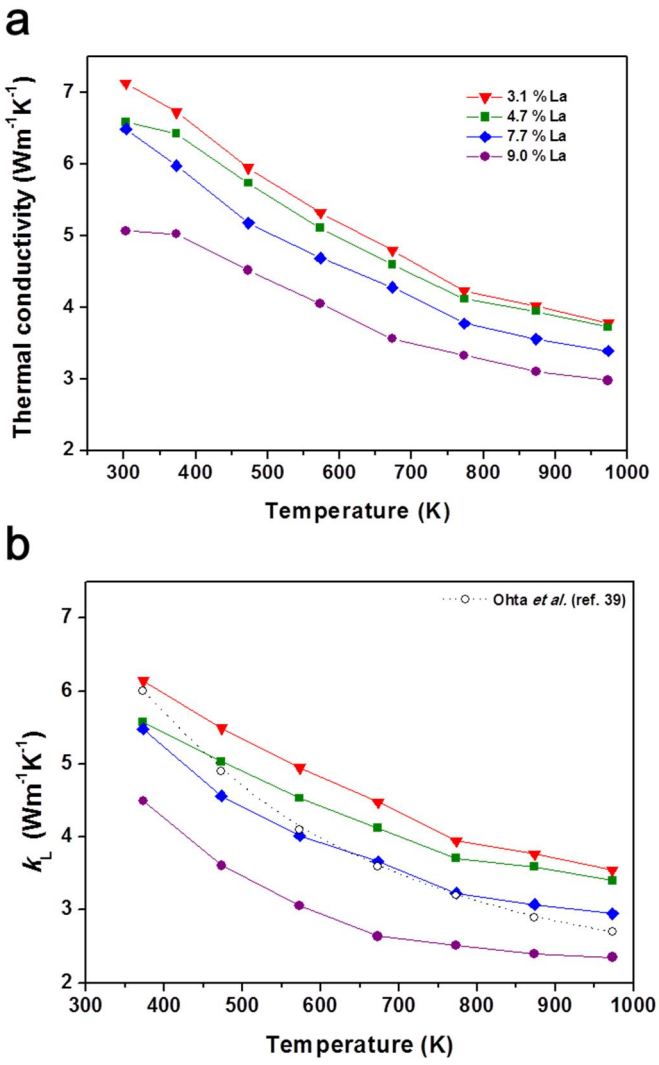

Figure 2.11. Temperature dependence of **(a)** total thermal conductivity (κ), and **(b)** lattice thermal conductivity (κ_L) of La-doped $SrTiO_3$ samples with various La doping levels.

2.3.4.4 Dimensionless Figure-of-merit, ZT

From the measured electrical conductivity, Seebeck coefficient, and thermal conductivity, we estimated the dimensionless figure-of-merit *ZT* of the nanostructured bulk La-doped $SrTiO_3$ in the temperature range from 373 K to 973 K (Figure 2.12a). The highest achieved *ZT* value was ~0.37 for the 9.0 at% La-doped $SrTiO_3$ at 973 K, which is ~25% higher than the *ZT* value of a bulk La-doped $SrTiO_3$ single crystal,[11a] and is among the highest values reported for doped $SrTiO_3$. The *ZT* values of the samples with high La dopant concentrations (7.7 or 9.0% La doping) were lower than those of the samples with low La dopant concentrations (3.1 or 4.7% La doping) below 600 K because of the unexpected reduction of the electrical conductivity. However, the *ZT* values obtained at high temperatures increased as the doping level increased. This high *ZT* was accomplished because the electrical conductivity was conserved while the thermal conductivity was reduced by the introduction of nanoscale interfaces. In general, nanostructured bulk materials fabricated by consolidating small nanocrystals will exhibit poor electrical transport properties because organic residues or pores can act as carrier scattering sites. In contrast, in this study we obtained nanostructured bulk samples of La-doped

$SrTiO_3$ with electrical conductivity as high as that of bulk La-doped $SrTiO_3$ by using nanoparticles without residual surfactant and by optimizing the sintering conditions.

2.3.5 Thermal Stability of Nanostructured La-doped $SrTiO_3$

In order to be commercially applicable, thermoelectric materials must be thermally stable at typical operating temperatures. Conventional thermoelectric materials based on chalcogenides of bismuth or lead have reasonable *ZT* values, but the durability of the devices including them cannot be guaranteed at high temperatures. Although there have been numerous reports on the thermoelectric properties of nanomaterials, their thermal stability has rarely been investigated. Because nanoparticles generally have lower melting points than their bulk counterparts, it has been hard to maintain their nanoscale features at high temperatures.[4m] On the other hand, oxide nanomaterials have advantages for high-temperature applications because of their high melting points. The La-doped $SrTiO_3$ nanoparticles studied here had a melting point of ~1500 °C and did not exhibit any growth at the measurement temperature of 973 K. To verify their thermal stability, we compared the dimensionless figures-of-merit, *ZT* of the as-prepared and heat-treated 9.0% La-doped $SrTiO_3$ nanostructured bulk pellets (Figure

2.12b). The heat treatment was performed at 973 K for 24 h. The nanostructured bulk La-doped $SrTiO_3$ exhibited almost the same *ZT* before and after the heat treatment, demonstrating its potential for high-temperature applications.

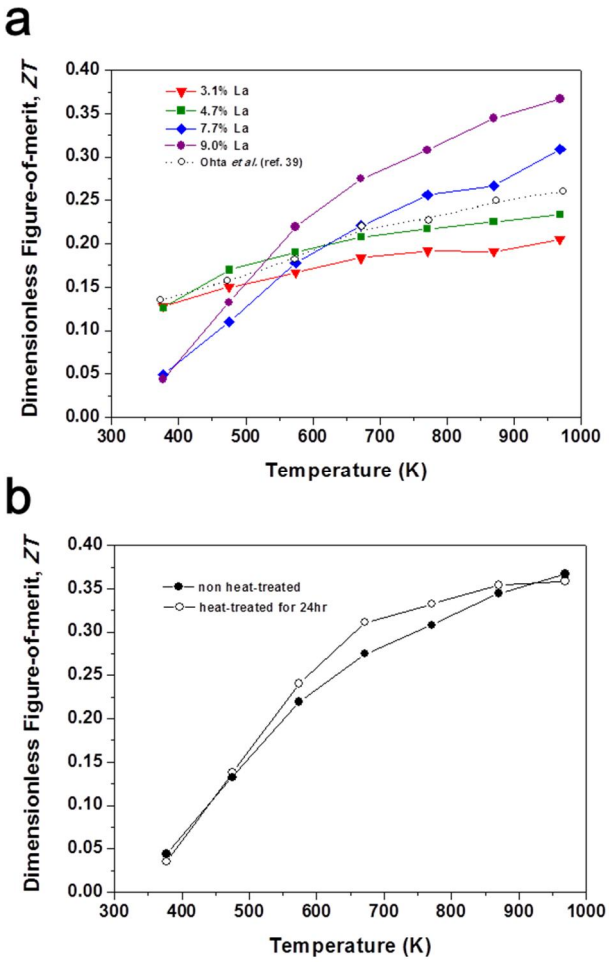

Figure 2.12. (a) Temperature dependence of dimensionless figure-of-merit (*ZT*) of La-doped $SrTiO_3$ samples with different La content, together with reported data.[11a] **(b)** Comparison of *ZT* of the as-prepared and heat-treated (973 K) nanostructured bulk pellets of 9.0% La-doped $SrTiO_3$.

2.4 Conclusion

In summary, we synthesized La-doped $SrTiO_3$ nanoparticles with controlled La doping levels. After the surfactants were removed, these nanoparticles were sintered using the SPS process to fabricate nanostructured bulk materials whose thermoelectric properties were then characterized. We have demonstrated that the thermoelectric properties in the nanostructured bulk materials are enhanced by the introduction of nanoscale interfaces that can reduce the thermal conductivity. The dimensionless figure-of-merit, *ZT* reached a maximum of ~0.37 at 973 K, which is ~25% higher than the *ZT* of the single-crystal bulk material. We found that it was possible to control the thermal conductivity independently while maintaining the electrical conductivity and Seebeck coefficient. We also investigated the effect of the dopant concentration on the thermoelectric efficiency, which is essential for improving the thermoelectric efficiency. The nanostructured bulk materials exhibited nearly identical thermoelectric efficiencies even after they were heat treated at 973 K, which demonstrates their suitability for high-temperature applications. In the current research, we demonstrated that colloidal synthetic method can be used to inexpensively prepare La-doped $SrTiO_3$ nanoparticles that

can be used to produce highly stable and efficient thermoelectric materials.

Parts of this research were published in "Colloidal Synthesis and Thermoelectric Properties of La-doped $SrTiO_3$ Nanoparticles" *Journal of Materials Chemistry A*, **2014**, 2, 4217.

2.5 References

[1] a) Disalvo, F. J. *Science* **1999**, *285*, 703. b) Bell, L. E. *Science* **2008**, *321*, 1457. c) Snyder, G. J.; Toberer, E. S. *Nat. Mater*. **2008**, *7*, 105. d) Tritt, T. M.; Subramanian, M. A. *MRS Bull*. **2006**, *31*, 188.

[2] a) Dresselhaus, M. S.; Chen, G.; Tang, M. Y.; Yang, R. G.; Lee, H.; Wang, D. Z.; Ren, Z. F.; Fleurial, J. P.; Gogna, P. *Adv. Mater*. **2007**, *19*, 1043. b) Chen, G.; Dresselhaus, M. S.; Dresselhaus, G.; Fleurial, J. P.; Caillat, T. *Int. Mater. Rev*. **2003**, *48*, 45.

[3] a) Venkatasubramanian, R.; Siivola, E.; Colpitts, T.; O`Quinn, B. *Nature*, **2001**, *413*, 597. b) Hsu, K. F.; Loo, S.; Guo, F.; Chen, W.; Dyck, J. S.; Uher, C.; Hogan, T.; Polychroniadis, E. K.; Kanatzidis, M. G. *Science*, **2004**, *303*, 818. c) Majumdar, A. *Science*, **2004**, *303*, 777. d) Harman, T. C.; Taylor, P. J.; Walsh, M. P.; LaForge, B. E. *Science*, **2002**, *297*, 2229. e) Hochbaum, A. I.; Chem, R.; Delgado,

R. D.; Liang, W.; Garnett, E. C.; Najarian, M. Majumdar, A.; Yang, P. *Nature*, **2008**, *451*, 163. f) Boukai, A. I.; Bunimovich, Y.; Tahir-Kheli, J.; Yu, J.-K.; Goddard, A.; Heath, J. R. *Nature* **2008**, *451*, 168. g) Han, M.-K.; Ahn, K.; Kim, H.; Rhyee, J.-S.; Kim, S.-J. *J. Mater. Chem*. **2011**, *21*, 11365. h) Zhao, Y.; Dyck, J. S.; Burda, C. *J. Mater. Chem*. **2011**, *21*, 17049. i) Saleemi, M.; Toprak, M. S.; Li, S.; Johnsson, M.; Muhammed, M. *J. Mater. Chem*. **2012**, *22*, 725. j) Toprak, M. S.; Stiewe, C.; Platzek, D.; Williams, S.; Bertini, L.; Muller, E.; Gatti, C.; Zhang, Y.; Rowe, M.; Muhammed, M. *Adv. Funct. Mater.* **2004**, *14*, 1189. k) Ibanez, M.; Cadavid, D.; Zamani, R.; Garcia-Castello, N.; Izquierdo-Roca, V.; Li, W.; Fairbrother, A.; Prades, J. D.; Shavel, A.; Arbiol, J.; Perez-Rodriguez, A.; Morante, J. R.; Cabot, A. *Chem. Mater*. **2012**, *24*, 562.

[4] a) Poudel, B.; Hao, Q.; Ma, Y.; Lan, Y.; Minnich, A.; Yu, B.; Yan, X.; Wang, D.; Muto, A.; Vashaee, D.; Chen, X.; Liu, J.; Dresselhaus, M. S.; Chen, G.; Ren, Z. *Science* **2008**, *320*, 634. b) Dong, G.-H.; Zhu, Y.-J.; Cheng, G.-F.; Ruan, Y.-J. *J. Alloys Compd*. **2013**, *550*, 164. c) Mehta, R. J.; Zhang, Y.; Karthik, C.; Singh, B.; Siegel, R. W.; Borca-Tasciuc, T.; Ramanath, G. *Nat. Mater*. **2012**, *11*, 233. d) Han, M.-K.; Kim, S.; Kim, H.-Y.; Kim, S.-J. *RSC Adv*.

2013, *3*, 4673. e) Liang, D.; Yang, H.; Finefrock, S. W.; Wu, Y. *Nano Lett*. **2012**, *12*, 540. f) Fan, F.-J.; Yu, B.; Wnag, Y.-X.; Zhu, Y.-L.; Liu, X.-J.; Yu, S.-H.; Ren, Z. *J. Am. Chem. Soc*. **2011**, *133*, 15910. g) Son, J. S.; Park, K.; Han, M.-K.; Kang, C.; Park, S.-G.; Kim, J.-H.; Kim, W.; Kim, S.-J.; Hyeon, T. *Angew. Chem. Int. Ed*. **2011**, *50*, 1363. h) Son, J. S.; Choi, M. K.; Han, M.-K.; Park, K.; Kim, J.-Y.; Lim, S. J.; Oh, M.; Kuk, Y.; Park, C.; Kim, S.-J.; Hyeon, T. *Nano Lett*. **2012**, *12*, 640. i) Ibanez, M.; Zamani, R.; LaLonde, A.; Cadavid, D.; Li, W.; Shavel, A.; Arbiol, J.; Morante, J. R.; Gorsse, S.; Snyder, G. J.; Cabot, A. *J. Am. Chem. Soc*. **2012**, *134*, 4060. j) Ibanez, M.; Cadavid, D.; Anselmi-Tamburini, U.; Zamani, R.; Gorsse, S.; Li, W.; Lopez, A. M.; Morante, J. R.; Arbiol, J.; Cabot, A. *J. Mater. Chem. A* **2013**, *1*, 1421. k) Dong, G.-H.; Zhu, Y.-J.; Chen, L.-D. *J. Mater. Chem*. **2010**, *20*, 1976. l) Dyck, J. S.; Mao, B.; Wang, J.; Dorroh, S.; Burda, C. *J. Electron. Mater*. **2012**, *41*, 1408. m) Scheele, M.; Oeschler, N.; Veremchuk, I.; Peters, S.-O.; Littig, A.; Kornowski, A.; Klinke, C.; Weller, H. *ACS Nano* **2011**, *5*, 8541.

[5] a) Ohtaki, M. *J. Ceram. Soc. Jpn*. **2011**, *114*, 102. b) Fergus, J. W. *J. Eur. Ceram. Soc*. **2012**, *32*, 525.

[6] Karppinen, M.; Fjellvag, H.; Konno, T.; Morita, Y.; Motohashi, T.; Yamauchi, H. *Chem. Mater*. **2004**, *16*, 2790.

[7] Terasaki, I.; Sasago, Y.; Uchinokura, K. *Phys. Rev. B* **1997**, *56*, R12685.

[8] a) Ohtaki, M.; Tsubota, T.; Eguchi, K.; Arai, H. *J. Appl. Phys*. **1996**, *79*, 1816. b) Jood, P.; Mehta, R. J.; Zhang, Y.; Peleckis, G.; Wang, X.; Siegel, R. W.; Borca-Tauciuc, T.; Dou, S. X.; Ramanath, G. *Nano Lett*. **2011**, *11*, 4337.

[9] Wang, Y.; Sui, Y.; Fan, H.; Wang, X.; Su, Y.; Su, W.; Liu, X. *Chem. Mater*. **2009**, *21*, 4653.

[10] Cui, Y.; He, J.; Amow, G.; Kleinke, H. *Dalton Trans*. **2010**, *39*, 1031.

[11] a) Ohta, S.; Nomura, T.; Ohta, H.; Koumoto, K. *J. Appl. Phys*. **2005**, *97*, 034106. b) Okuda, T.; Nakanishi, K.; Miyasaka, S.; Tokura, Y. *Phys. Rev. B* **2001**, *63*, 113104. c) Liu, J.; Wang, C. L.; Su, W. B.; Wang, H. C.; Zheng, P.; Li, J. C.; Zhang, J. L.; Mei, L. M. *Appl. Phys. Lett*. **2009**, *95*, 162110.

[12] Ravichandran, J.; Siemons, W.; Oh, D.-W.; Kardel, J. T.; Chari, A.; Heijmerikx, H.; Scullin, M. L.; Majumdar, A.; Ramesh, R.; Cahill, D. G. *Phys. Rev. B* **2010**, *82*, 165126.

[13] Suzuki, H.; Bando, H.; Ootuka, Y.; Inoue, I. H.; Yamamoto, T.; Takahashi, K.; Nishihara, Y. *J. Phys. Soc. Jpn*. **1996**, *65*, 1529.

[14] a) Wang, X.; Zhuang, J.; Peng, Q.; Li, Y. *Nature* **2005**, *437*, 121. b) Fujinami, K.; Katagiri, K.; Kamiya, J.; Hamanaka, T.; Koumoto, K. *Nanoscale* **2010**, *2*, 2080.

[15] Eckert, J. O.; Hung-Houston, C. C; Gersten, B. L.; Lencka, M. M.; Riman, R. E. *J. Am. Ceram. Soc*. **1996**, *79*, 2929.

[16] Ohta, S.; Nomura, T.; Ohta, H.; Hirano, M.; Hosono, H.; Koumoto, K. *Appl. Phys. Lett*. **2005**, *87*, 092108.

[17] a) Dai, X.; Xu, Z.; Li, J.-F.; Viehland, D. *J. Mater. Res*. **1996**, *11*, 718. b) Yi, J. Y.; Lee, J.-K. *J. Phys. D: Appl. Phys*. **2011**, *44*, 415302.

[18] Santander-Syro, A. F.; Copie, O.; Kondo, T.; Fortuna, F.; Pailhes, S.; Weht, R.; Qiu, X. G.; Bertran, F.; Nicolaou, A.; Taleb-Ibrahimi, A.; LeFevre, P.; Herranz, G.; Bibes, M.; Reyren, N.; Apertet, Y.; Lecoeur, P.; Barthelemy, A.; Rozanberg, M. J. *Nature* **2011**, *469*, 189.

[19] a) Muta, H.; Kurosaki, K.; Yamanaka, S. *J. Alloys Compd*. **2004**, *368*, 22. b) Wang, H. C.; Wang, C. L.; Su, W. B.; Liu, J.; Peng, H.; Sun, Y.; Zhang, J. L.; Zhao, M. L.; Li, J. C.; Yin, N.; Mei, L. M.

Ceram. Int. **2011**, *37*, 2609. c) Kosuga, A.; Wang, Y.; Yubuta, K.; Koumoto, K.; Funahashi, R. *Jpn. J. Appl. Phys*. **2010**, *49*, 071101. d) Cui, Y.; Salvador, J. R.; Yang, J.; Wang, H.; Amow, G.; Kleinke, H. *J. Electron. Mater*. **2009**, *38*, 1002.

[20] Androulakis, J.; Todorov, I.; He, J.; Chung, D.-Y.; Dravid, V.; Kanatzidis, M. *J. Am. Chem. Soc*. **2011**, *133*, 10920.

[21] Adireddy, S.; Lin, C.; Cao, B.; Zhou, W.; Caruntu, G. *Chem. Mater*. **2010**, *22*, 1946.

Chapter 3. Extraordinary off-stoichiometric bismuth telluride for enhanced n-type thermoelectric performance

3.1 Introduction

Physical and chemical properties of inorganic solids can be remarkably enhanced or tuned by introducing appropriate dopants or by partially substituting specific constituent elements. Such chemical approaches have been extensively applied to a wide range of technologically important materials to achieve desired optical, electrical, catalytic, and magnetic properties for various applications.[1] However, the chemical composition of solid-state materials is determined by the phase equilibria of constituent elements at a given temperature and pressure. Only specific compositions are allowed for not only stoichiometric solids, but also nonstoichiometric ones, with the exception of solid solutions. As a result, formation of new structures, doping, and substitutional alloying are strictly restricted, thereby seriously hindering the synthesis of novel materials with desired properties for various applications. Indeed, not all classes of

compounds are eligible for these doping or substitution processes. One notorious example is Bi_2Te_3-based compounds that are representative thermoelectric (TE) materials operating near room temperature.[2]

TE technology enables direct conversion between heat and electricity and is consequently considered a promising means of sustainable power generation and energy saving. The efficiency of TE conversion is defined by the dimensionless figure of merit $ZT = \sigma S^2 T/\kappa$, where σ is the electrical conductivity, S is the Seebeck coefficient, κ is the thermal conductivity, T is the absolute temperature, and the product σS^2 is the power factor (PF).[3] Very few dopants and substituents have proven effective in improving the TE properties of Bi_2Te_3-based compounds, severely restricting the adaptation of traditional semiconductor fabrication processes. Rare successful examples include the alloying of Bi_2Te_3-based compounds with Sb or Se to form solid solutions of $Bi_xSb_{2-x}Te_3$ for p-type TE materials and $Bi_2Te_{3-y}Se_y$ for n-type TE materials.[4] Copper is one of the few dopants to increase the ZT of n-type $Bi_2Te_{3-y}Se_y$.[5]

The problems described above are in striking contrast to other TE materials working at high temperatures, where the ZT values have been remarkably enhanced by innovative strategies.[6] They primarily

involve reduction in thermal conductivity, especially, lattice thermal conductivity (κ_{latt}). Representative examples are the introduction of nanostructuring to $AgPb_mSbTe_{m+2}$ (LAST)[7] and SrTe-doped PbTe[8] and the inclusion of guest species in the cages of intermetallic clathrates and skutterudites.[9] Unfortunately, κ_{latt} of these materials approaches a lower fundamental limit. Furthermore, nearly none of these strategies are effective for Bi_2Te_3-based systems. Accordingly, most of the recent advances made in the enhancement of the *ZT* of Bi_2Te_3-based TE materials rely on ball-milling or melt-spinning powder processes followed by pelletization. These procedures give rise to decrease in κ_{latt} by scattering heat-carrying phonons at the grain boundaries.[10] However, these strategies mostly work for p-type, not for n-type Bi_2Te_3-based TE materials, because the *PF* of n-type TE materials is so sensitive to the crystallographic direction that the reduced κ_{latt} is compromised by the decreased *PF*.[5] The poorer performance of n-type Bi_2Te_3-based materials than that of p-type materials severely limits their practical applications because TE modules consist of junctions of n- and p-type TE materials, and the worse counterpart determines the overall efficiency. Furthermore, there are very few strategies for the enhancement of *PF*s of both p- and n-

type TE materials,[11] and this is regarded as one of the most important issues for all TE materials. High *PF* is essential for achieving high performance during power generation. In contrast to κ_{latt} that has a lower bound, *PF* does not have a theoretical upper bound.

Here we report that we go beyond compositional limitations stringently regulated by phase equilibrium and stabilize extraordinary off-stoichiometric compounds through a nanochemical synthetic method. Remarkably, the resulting bulk $K_{0.06}Bi_2Te_{3.18}$ (bulk KBT), despite considerable deviation from the elemental ratio permitted by the phase diagram, shows high phase homogeneity and thermal stability. In contrast, the sample with a similar nominal composition prepared using a conventional high-temperature solid-state reaction contains excess tellurium that decomposes upon heating. The polycrystalline bulk KBT sample with a highly preferential orientation exhibits a surprisingly high *PF* of ~43 μW cm^{-1} K^{-2} due to electron donating potassium dopants, rivalling that of a single crystal $Bi_2Te_{3-x}Se_x$, and one of the highest *ZT* (>1.1) among n-type TE materials that operate near room temperature. Very importantly, we use spherical aberration-corrected high-angle annular dark-field scanning transmission electron microscopy (Cs-corrected HAADF-STEM) combined with energy

dispersive X-ray spectroscopy (EDS) and electron energy loss spectroscopy (EELS) to characterize the locations of excess potassium and tellurium atoms, which allows us to clearly explain the unusual compositions and the resulting excellent TE performance. Our new approach enables the synthesis of solid-state materials whose compositions cannot be stabilized according to phase equilibrium and consequently the realization of enhanced properties. Furthermore, this method can be generalized to a wide range of materials for various applications, not just limited to bismuth telluride for TE applications.

3.2 Expeimental Section

3.2.1 Chemicals

Tellurium dioxide (97.0%), bismuth (III) nitrate pentahydrate (98.0%), ethylene glycol (anhydrous, 99.8%), polyvinylpyrrolidone (PVP, average mol. wt. 40000), potassium hydroxide (90%), hydrazine hydrate solution (78-82%), acetone (99.9%), ethanol (99.8%), and potassium chunk (99.5%) were purchased from Aldrich Chemical Company. Bismuth chunk (99.999%) and tellurium shot (99.999%) were purchased from 5N plus.

3.2.2 Synthesis of Bi_2Te_3 Nanotubes and Control Bulk Powder.

All syntheses were carried out under an Ar atmosphere using standard Schlenk line techniques. Bi_2Te_3 nanotubes were synthesized through a two-step solution reaction using a previously reported method after some modifications.[12] To synthesize tellurium-rich Bi_2Te_3 (BT) nanotubes, the precursor solutions of Bi and Te were separately prepared. The Te precursor solution was prepared by reacting 2.394 g of tellurium dioxide, 3 g of PVP, and 5.61 g of potassium hydroxide in 150 ml of ethylene glycol. The Bi precursor solution was prepared by dissolving 4.85 g of bismuth nitrate pentahydrate in 50 ml of ethylene glycol.

Te nanorods were synthesized by injecting 3 ml of hydrazine hydrate solution to the Te solution at 140^{o}C, followed by aging for 1 h. The solution was subsequently heated to 160^{o}C, and the Bi solution was added in a controlled manner. The resulting reaction mixture was aged for 30 min to 60 min and cooled to room temperature. Fine control of the addition of the Bi solution and the reaction time is key to obtaining tellurium-rich Bi_2Te_3 nanotubes. The product was collected by centrifugation at 13000 rpm, followed by washing with ethanol and distilled water several times. To incorporate potassium, the as-synthesized BT nanotubes were reacted with 0.2 M potassium

hydroxide-ethylene glycol solution under vigorous stirring at 140^{o}C for 24 h. Finally, the product was washed with acetone and dried under vacuum.

The control samples of Bi_2Te_3, Bi_2Te_{3+y}, $K_xBi_2Te_{3+y}$ were obtained in bulk ingot form by melting a mixture of K/Bi/Te in an evacuated fused silica tube at 973 K for 12 h, followed by natural cooling to room temperature. The ingot samples were manually ground with a mortar and pestle in an Ar-filled glove box.

3.2.3 Spark Plasma Sintering

The as-synthesized BT and KBT nanotubes and ground bulk powders were loaded into a graphite die in an Ar-filled glove box and cold-compacted manually. The graphite die was taken out of the glove box and placed in a spark plasma sintering system (SPS-211Lx, Fuji Electronic Industrial Co., Japan). The sample chamber was evacuated to a vacuum of ~1.4×10^{-2} Torr, and powder samples in the graphite die were consolidated by spark plasma sintering under an axial pressure in vacuum.

3.2.4 Sample Characterization

3.2.4.1 Powder X-ray Diffraction (XRD) and Infrared Spectroscopy

Powder XRD analysis was performed using a D/Max-2500 Rigaku powder X-ray diffractometer (Cu Kα radiation) operating at 40 kV and 100 mA.

To understand the structurally anisotropic nature of bulk KBT, we estimated its degree of preferential orientation based on the in-plane and out-of-plane XRD patterns of bulk KBT (Figure 3.13). The Lotgering factor (*LF*) is commonly employed to quantify the degree of preferential orientation (texture) of a given material.[13] *LF* is defined by Eq. 3.1:

$$LF = \frac{(p-p_0)}{(1-p_0)} p = \frac{\sum I_{00l}}{\sum I_{hkl}} \qquad \text{(Eq. 3.1)}$$

where p is the degree of orientation for a preferential orientation, p_0 is the degree of orientation for a random orientation, and ΣI_{00l} and ΣI_{hkl} are the sums of peak intensities of the (00*l*) and (*hkl*) reflections in the 2θ range of 10° to 60°. For example, *LF* is 1 for a perfect (00*l*)-plane preferential orientation according to Eq. 3.1. For bulk KBT, the *LF* of reflections taken along the in-plane and out-of-plane are determined to be 0.78 and 0.11, respectively, indicating a highly anisotropic feature of bulk KBT.

Fourier transform infrared spectroscopy (FT-IR) spectra were recorded using a Vertex 70 Bruker FT-IR spectrometer equipped with a DLATGS detector and a KBr substrate with a multilayer coating beam splitter.

3.2.4.2 Thermal Analysis

Thermogravimetric analysis experiments were carried out on a Netzsch TG 209 F1 thermogravimetric analyzer by heating the samples in an alumina boat to 823 K at a rate of 10 K min^{-1} under Ar flow. The differential scanning calorimeter (DSC) measurements were performed on a Netzsch STA 449 F3 Jupiter DSC in an aluminum crucible with a lid under Ar flow to 973 K at a heating rate of 10 K min^{-1}.

3.2.4.3 Chemical Analysis

Chemical compositions were determined by inductively coupled plasma atomic emission spectroscopy (ICP-AES) using Shimadzu ICPS-7500. To optimize the accuracy of the ICP-AES analysis of Bi and Te, we prepared stoichiometric Bi_2Te_3 by a high-temperature solid-state reaction to serve as the reference sample. For the preparation of the reference, the weight of Bi and Te elements was measured at a 10^{-4} gram scale. Using the Bi_2Te_3 reference, calibration curves were drawn for Bi and Te. More than 20 independent specimens per each material were measured and corrected by the calibration curve. The obtained

values were averaged to give the chemical compositions of the materials. Carbon content was determined by CHNS analysis using LECO CHNS-932.

3.2.4.4 Transmission Electron Microscopy (TEM) and Scanning Electron Microscopy (SEM)

Cross-sectional samples for scanning TEM (STEM) were prepared for bulk BT and KBT by focused ion beams (FIB, Helios 650, FEG, FEI) with a dual beam microscope using gallium ion milling. Before the ion milling process, carbon was sputtered to preserve the sample by surface coating. The samples were further polished with a low-voltage and low-angle argon ion beam milling apparatus (NANO MILL, Model 1040, FISCHIONE). The atomic structures and chemical composition were examined using a spherical aberration-corrected JEM ARM-200F microscope (Cold FEG Type, JEOL) equipped with a SDD type energy dispersive X-ray spectroscopy (EDS) detector (Solid Angle 0.9-sr, X-MaxN 100TLE, OXFORD) and electron energy loss spectroscopy (EELS) detector (965 GIF Quantum ER, GATAN) at 200 kV.

In the high-angle annular dark-field (HAADF) STEM images, the point-to-point resolution was about 80 pm after the Cs-correction, and the angular range of the annular detector used was 68 mrad to 280 mrad.

All images were acquired by a high-resolution CCD detector using a 2k × 2k pixel device (UltraScan 1000, GATAN).

For STEM-EDS analyses, chemical maps were acquired with a probe size of 0.13 nm and a probe current of 40 pA. For STEM-EELS measurements, the energy dispersion was set at 0.1 eV ch^{-1}. The full-width at half-maximum of the zero-loss peak in vacuum was 0.6 eV. The convergence and collection semi-angles were 19 mrad and 52 mrad, respectively.

The field emission scanning electron microscopy (FESEM) images were obtained on a JSM-6701F microscope.

3.2.5 Thermoelectric Properties Measurement

3.2.5.1. Electrical Transport Properties

The samples after SPS were cut for electrical and thermal property measurements using a diamond saw and polished with ethanol using a polishing machine under N_2 atmosphere. The polished samples are rectangular-shaped with dimensions of ~3 mm × 3 mm × 9 mm. The longer direction coincides with the direction in which the electrical conductivity is measured. The electrical conductivity σ and the Seebeck coefficient S were measured simultaneously under a He atmosphere from room temperature to ~470 K on a ULVAC-RIKO ZEM-3

instrument system.

3.2.5.2. Thermal Conductivity

Thermal diffusivity (D) was directly measured under an Ar atmosphere, and the specific heat (C_P) was indirectly derived using a standard sample (Pyroceram) as a function of temperature from room temperature to ~470 K using a flash diffusivity method in a Netzsch LFA 457 MicroFlash instrument. In a flash diffusivity method, the front face of a disk-shaped sample is irradiated by a short laser burst, and the resulting rear face temperature rise is recorded and analyzed by an IR detector. The thermal conductivity (κ) was calculated from the equation $\kappa = DC_P\rho$, where ρ is the density of the sample.

The total thermal conductivity κ_{tot} is the sum of the lattice (κ_{latt}) and electronic thermal (κ_{elec}) conductivities. κ_{elec} is proportional to the electrical conductivity (σ) according to the Wiedemann-Franz law ($\kappa_{elec} = L\sigma T$), where L is the temperature-dependent Lorenz number and T is the absolute temperature. An L value is estimated in the single parabolic band (SPB) model[14] from the temperature-dependent Seebeck coefficient, which is based on the assumption of acoustic phonon scattering. κ_{latt} is calculated from the relations described above.

3.2.5.3 Hall Measurement

The electron concentration (n_e) and the Hall coefficient (R_H) were measured by a Hall effect measurement system in the temperature range of ~173 K to ~ 373 K using a Quantum Design physical property measurement system (PPMS-ECII). The samples were connected with four Pt wires using silver paste and loaded into a magnetic cryostat. The electron mobility (μ_e) was calculated from the carrier concentration and the resistivity based on the assumptions of a single band model.

3.2.6 Density Functional Theory (DFT) Calculation

The total energies and the optimized crystal structures were calculated by DFT with PBEsol exchange-correlation functional[15] using the projector augmented wave method[16] implemented in the Vienna ab initio simulation package.[17] To calculate the defect formation energy, we used supercells of Bi_2Te_3 accommodating 90 atoms. Spin-orbit coupling was included in our electronic structure calculations. A plane-wave energy cutoff of 400 eV was used with the 6 × 6 × 4 k-points in the first Brillouin zone. Structural optimizations were performed with the force criterion of 1 meV $Å^{-1}$. For an accurate description of formation energy, we applied correction schemes for finite cell effects.[18]

To understand the conduction behavior of bulk BT and KBT, we

calculated their electronic structures based on DFT by employing the same defect conditions confirmed by the EELS-EDS results. For bulk BT, we used $Bi_{35}Te_{55}$, a supercell of $Bi_2Te_{3.14}$, with the defects of Te_{Bi} (Te at the Bi site). For bulk KBT, we used $KBi_{35}Te_{55}$ with the defects of K_{int1} (potassium at the interlayer space of the Bi_2Te_3 lattices) and Te_{Bi}. DFT calculations result in n-type electronic structures for both bulk BT and bulk KBT. In comparison, we calculated the electronic structure of K-doped bismuth telluride that possesses different types of defects: K_{Bi} (potassium substituting Bi) and V_{Bi} (Bi vacancy) along with that of undoped Bi_2Te_3. With this defect condition, $KBi_{34}Te_{54}$, a supercell of $K_{0.06}Bi_2Te_{3.18}$, reveals a p-type electronic structure by DFT.

To determine the solubility limit of potassium, we additionally calculated formation energy of potassium impurity. For simplicity, we only considered the single point-defect configurations of K_{int1}, K_{int2} (potassium at the interstitial site), and K_{Bi}. Based on the formation energies, concentrations of potassium impurities were calculated under a tellurium-rich condition and a growth temperature at 800 K. The calculation results show that K_{Bi} is the most stable defect with a maximum solubility of 0.02% in the cationic site ($K_{0.0004}Bi_{1.9996}Te_{3.0073}$).

3.3. Result and Discussion

3.3.1 Synthesis of Te-rich and K-incoporated Bi_2Te_3 nanotubes

The seemingly obvious way of obtaining n-type Bi_2Te_3 is the addition of excess tellurium as an electron donor to produce Bi_2Te_{3+y}. However, the phase diagram of the Bi-Te binary system allows limited range of Bi:Te stoichiometry from 2:2.98 to 2:3.02 (Figure 3.1).[19] Therefore, it is very difficult to incorporate a large excess of tellurium to provide enough electron carriers to achieve a high *ZT* by conventional synthetic methods. We overcome this problem by utilizing a nanochemical approach that is kinetically controllable at the atomic level.

$Bi_2Te_{3.14}$ nanotubes were synthesized from Te nanorods using a two-step procedure that was modified from a previously reported method (Scheme 3.1).[12] We synthesized polyvinylpyrrolidone (PVP)-stabilized Te nanorods with a typical length of ~1 μm and a diameter of 50 nm. The as-synthesized Te nanorods were reacted with $Bi(NO_3)_3$ to produce Bi_2Te_3 nanotubes. To achieve a tellurium-rich phase, we performed the synthesis at a relatively low temperature of 160°C to stabilize excess tellurium in the Bi_2Te_3 structure. In addition, PVP ligands act as a diffusion barrier, which slows down the reaction between Bi^{3+} and Te^{2-} ions and causes the Kirkendall effect.[20] The outward diffusion of Te^{2-}

ions proceeds relatively faster than the inward diffusion of Bi^{3+} ions, forming hollow Bi_2Te_3 nanotubes with kinetically stabilized excess tellurium. The chemical composition was determined to be $Bi_2Te_{3.14}$ by inductively coupled plasma atomic emission spectroscopy (ICP-AES), demonstrating the incorporation of excess tellurium. The bismuth telluride nanotubes have a polycrystalline nature, being composed of nanoplates with a thickness of ~10 nm to 20 nm, and they accordingly have a rough and defective morphology. Their typical length and diameter are ~1 μm and ~70 nm to 80 nm, respectively, as shown in transmission electron microscopy (TEM) (Figure 3.2) and scanning electron microscopy (SEM) images (Figure 3.3). Their hollow structures can be clearly seen in scanning transmission electron microscopy (STEM) images and EDS (Figure 3.4). It should be noted that PVP derivatives still remain after washing as observed in the FT-IR spectrum (Figure 3.5). Because such organic residues can give rise to high electrical resistivity, we replaced them with a substituent that can contribute to improving n-type TE performance. $Bi_2Te_{3.14}$ nanotubes were reacted with KOH dissolved in ethylene glycol to facilitate an ion-exchange reaction between residual PVP and potassium cations. This KOH treatment is a critical step for synthesizing the final bulk KBT

because not only does it remove residual PVP, but it also enables the incorporation of potassium cations. Thermogravimetric analysis (TGA) shows ~40% of PVP residues were removed by the reaction (Figure 3.6). ICP-AES analysis gave the composition of "$K_{0.07}Bi_2Te_{3.14}$". Powder X-ray diffraction (XRD) patterns of "$Bi_2Te_{3.14}$" and "$K_{0.07}Bi_2Te_{3.14}$" nanotubes correlate well with those of theoretical calculations, with no evidence of Te and K_2Te impurities (Figure 3.7).

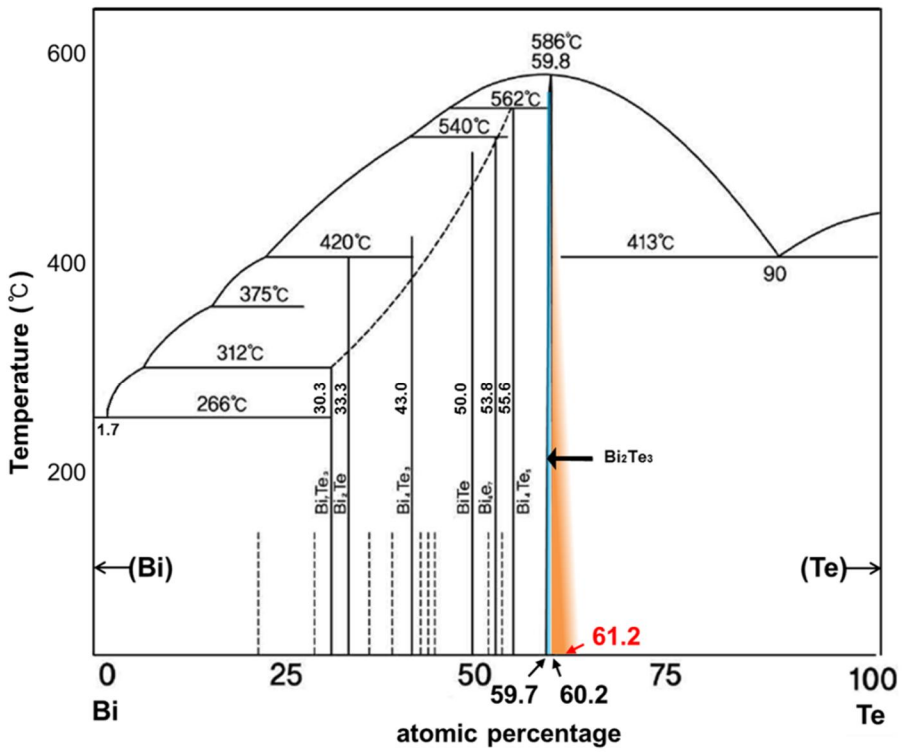

Figure 3.1. A phase diagram of Bi-Te binary system. The blue strip represents the region of phase equilibrium near the molar ratio of Bi:Te = 2:3. This work expanded the solubility limit of Bi to Te from 60.2 to 61.2 atomic percentage, depicted in orange, which cannot be achieved by other synthetic methods.

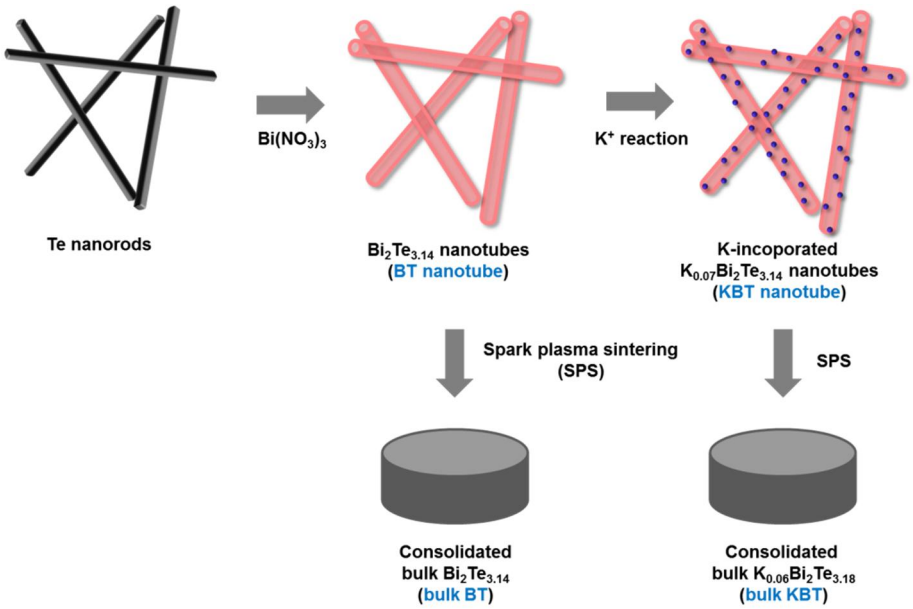

Scheme 3.1. Schematic illustration of syntheses for $Bi_2Te_{3.14}$ nanotubes (BT nanotube), K-incorporated $K_{0.07}Bi_2Te_{3.14}$ nanotubes (KBT nanotube), consolidated bulk $Bi_2Te_{3.14}$ (bulk BT), and consolidated bulk $K_{0.06}Bi_2Te_{3.18}$ (bulk KBT).

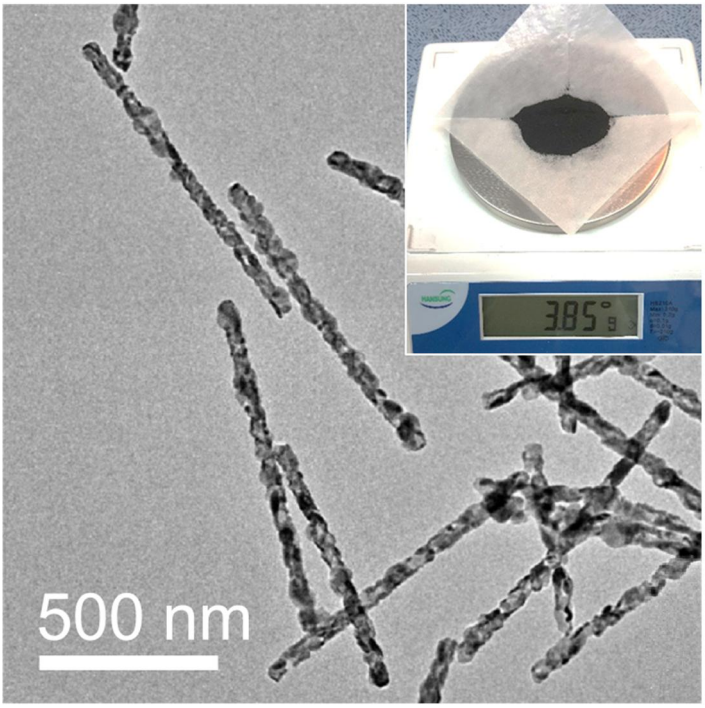

Figure 3.2. A representative transmission electron microscopy (TEM) image of the KBT nanotubes. A typical production scale for the nanotubes is ~4 g per batch (inset).

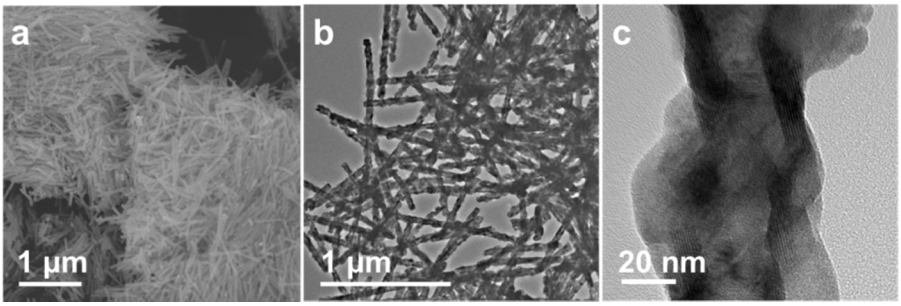

Figure 3.3. Typical **(a)** scanning and **(b and c)** transmision electron microscopy (SEM and TEM) images of BT nanotubes.

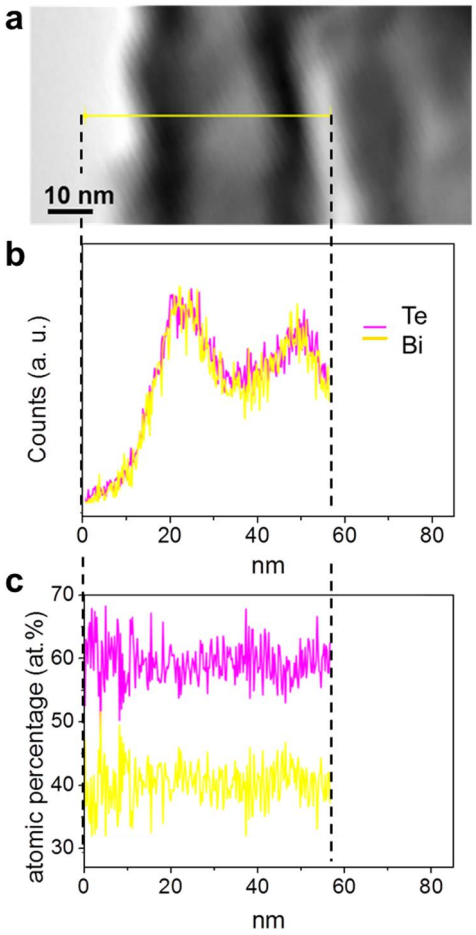

Figure 3.4. Scanning TEM (STEM) and energy dispersive X-ray spectroscopy (EDS) elemental mapping on a BT nanotube showing its hollow nature. **(a)** A STEM image of BT nanotube. **(b)** STEM-EDS result taken along the yellow line in (a) across the BT nanotube confirming hollow nature of BT nanotube. **(c)** STEM-EDS shows the molar ratio of Bi to Te to be approximately 2:3.

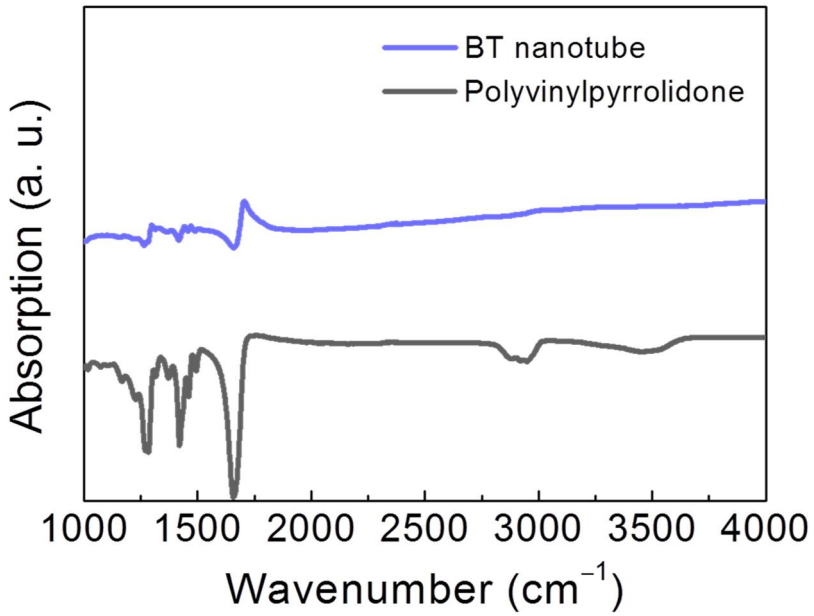

Figure 3.5. Fourier transform infrared spectroscopy (FT-IR) spectra of BT nanotube in comparison with polyvinylpyrrolidone (PVP) showing the presensce of PVP in BT nanotube sample.

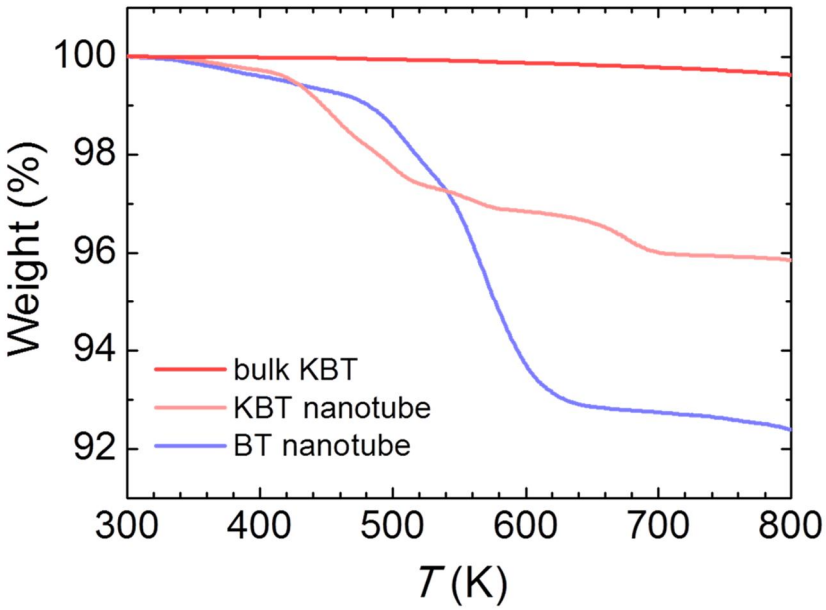

Figure 3.6. Thermogravimetric analysis (TGA) of bulk KBT as well as BT and KBT nanotube samples up to 800 K at a rate of 10 K min^{-1} under Ar flow. The percent weight loss decreases after reaction with KOH.

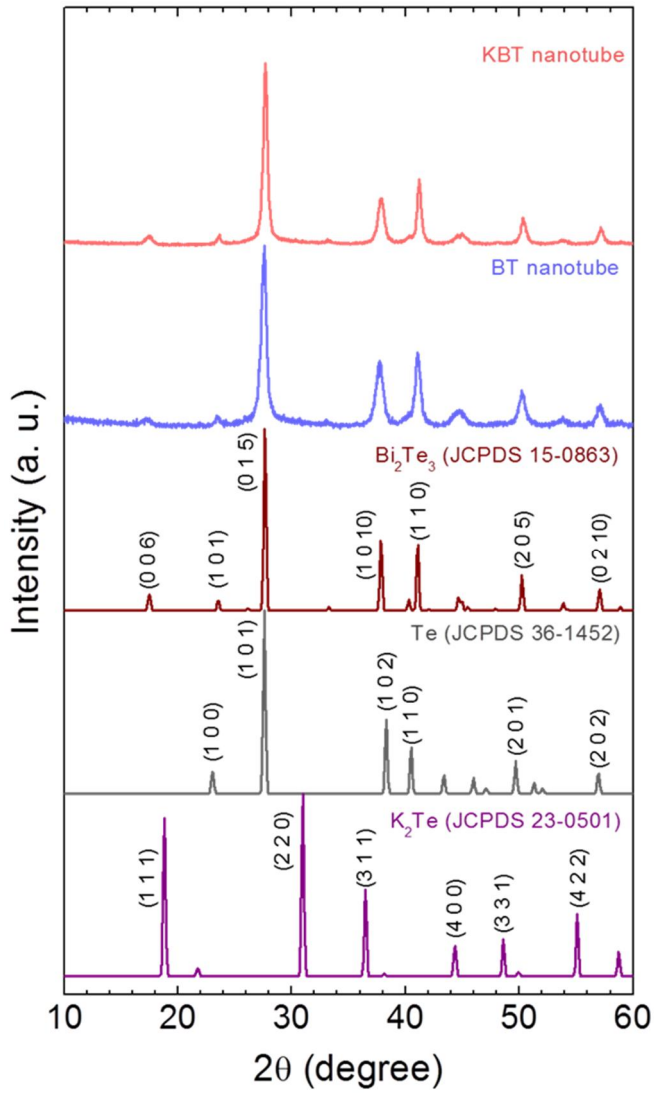

Figure 3.7. Powder X-ray diffraction (XRD) patterns of BT and KBT nanotube samples in comparison to Bi_2Te_3, Te, and K_2Te references.

3.3.2 Fabrication of bulk Bi_2Te_3 using Bi_2Te_3 nanotubes

The synthesis of tellurium-rich and potassium-incorporated bismuth telluride nanotubes is highly reproducible and scalable with production of ~4 g per batch (Figure 3.2, inset). The nanopowder was pressed into a dense bulk pellet with a typical diameter of 13 mm and a thickness of ~6 mm to 7 mm (>95% theoretical density) by spark plasma sintering (SPS), consequently converting the nanopowder into bulk form. The resulting bulk pellet was cut and polished along in-plane and out-of-plane directions for further characterization (Figure 3.8). We also prepared control samples of stoichiometric Bi_2Te_3 as well as tellurium-excess $Bi_2Te_{3.05}$ and $Bi_2Te_{3.14}$ using high-temperature solid-state reactions. ICP-AES analysis reveals that the bulk samples generated from the SPS of the $Bi_2Te_{3.14}$ nanotubes (BT nanotube) and $K_{0.07}Bi_2Te_{3.14}$ nanotubes (KBT nanotube) have chemical compositions of $Bi_2Te_{3.14}$ (bulk BT) and $K_{0.06}Bi_2Te_{3.18}$ (bulk KBT), respectively. It is surprising that both nanotubes and their bulk counterparts do not show evidence of isolated tellurium according to XRD studies (Figure 3.9). In contrast, the control sample "$Bi_2Te_{3.05}$" prepared using a solid-state reaction shows the peak at 23^o, which corresponds to the (001) reflection of hexagonal tellurium. Furthermore, TGA data reveals that

the control $Bi_2Te_{3.05}$ sample shows a weight loss above ~680 K upon heating under Ar flow as elemental tellurium does, suggesting the decomposition of excess tellurium, which has a melting point of 720 K. In contrast, the bulk KBT sample does not show noticeable weight loss up to 800 K (Figure 3.10). According to differential scanning calorimetry (DSC) data, the bulk BT and KBT as well as the control stoichiometric Bi_2Te_3 show single melting behaviors with onsets at 851 K, 848 K, and 859 K, respectively (Figure 3.11). In contrast, the control tellurium-rich $Bi_2Te_{3.05}$ and $Bi_2Te_{3.14}$ melts incongruently, exhibiting the additional endothermic peak for the melting of tellurium at 687.5 K and 688.0 K, respectively, which is in agreement with TGA results. The thermal analysis of bulk BT and KBT reveals their high thermal stability and phase-homogeneity despite the inclusion of excess potassium and tellurium. These data clearly demonstrate that our nanochemical method enables the synthesis of off-stoichiometric compounds that violate the phase diagram of the constituent elements. It is also noteworthy that the samples after SPS do not contain organic residues that are considered a serious problem of solution-processed materials for TE applications (Figure 3.12). XRD pattern of the bulk KBT taken along the in-plane direction shows a highly preferred

orientation of (00l) reflections in comparison to that measured along the out-of-plane direction (Figure 3.13). This result clearly demonstrates that the one-dimensional nanotubes are well aligned to form a two-dimensional arrangement perpendicular to the pressing direction of SPS. SEM images also show a single crystal-like and highly oriented morphology of the bulk KBT sample (Figure 3.14). Theoretical calculations on the formation energy within the density functional theory (DFT) reveal that the composition corresponding to the highest solubility limit at 800 K is "$K_{0.0004}Bi_{1.9996}Te_{3.0073}$", suggesting that potassium and tellurium-rich Bi_2Te_3 cannot be obtained using conventional high-temperature solid-state reactions (Figure 3.15 to 3.18).

We performed atomic resolution HAADF-STEM, EDS, and EELS studies on bulk BT and KBT samples to characterize how excess potassium and tellurium are stabilized and where they are located. All specimens for TEM studies are pellets that are pressed by SPS, unless otherwise noted. Bi_2Te_3 crystallizes in the rhombohedral space group R-3m, featuring three hexagonally-packed Te atomic layers that are interleaved by octahedral Bi atoms. Each Bi_2Te_3 layer is stacked by van der Waals interaction along the c-axis (Figure 3.19a). Conceptually, it is

a defective NaCl-type (rock salt) structure. If we consider a "Na_3Cl_3" structure viewed along the [110] direction, removal of 1/3 of the Na atomic layer results in the Bi_2Te_3 structure. Consequently, the guest species can be inserted into the octahedral sites located between the layers (Figure 3.19b).

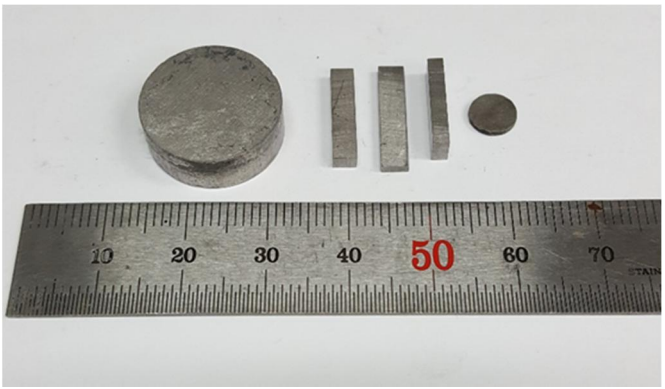

Figure 3.8. A typical dense pellet of bulk KBT by SPS (left) and specimens cut for measuring in-plane electrical (bars, middle) and thermal transport properties (disk, right).

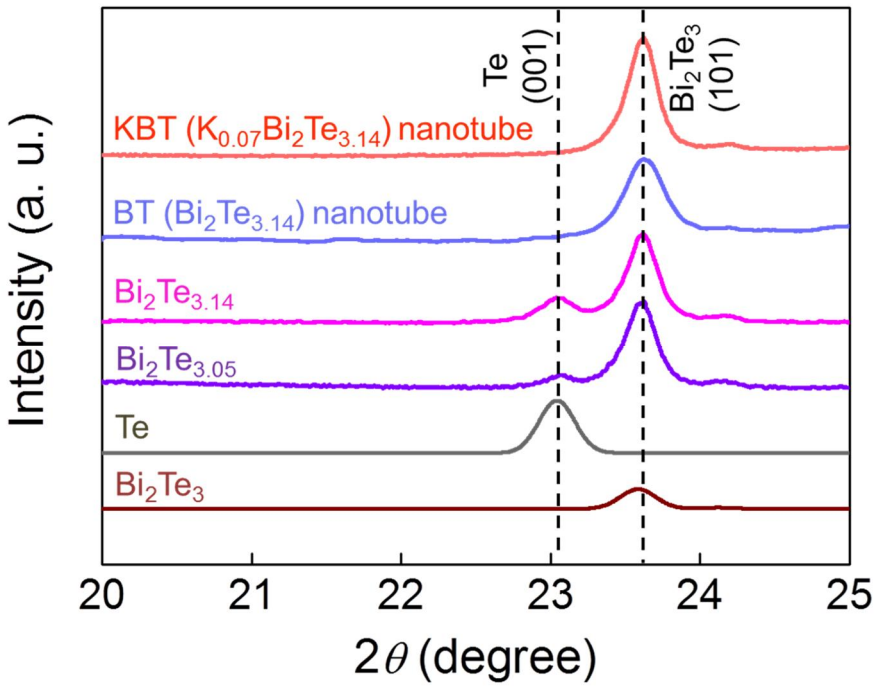

Figure 3.9. Powder X-ray diffraction (XRD) patterns of BT and KBT nanotubes in comparison with those of control $Bi_2Te_{3.05}$ and $Bi_2Te_{3.14}$ samples containing excess tellurium. Theoretical patterns of Bi_2Te_3 (JCPDS 15-0863) and Te (JCPDS 36-1452) are given. The tellurium-rich control samples show the (001) reflection of hexagonal tellurium.

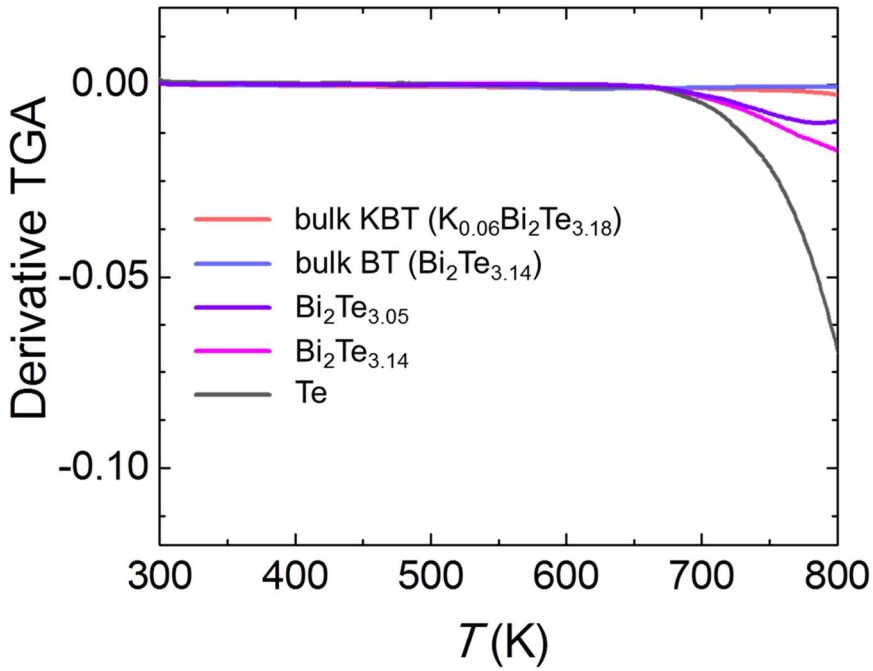

Figure 3.10. The first derivative of the thermogravimetric analysis (TGA) curve showing thermal stability of bulk BT and KBT. The control $Bi_2Te_{3.05}$ and $Bi_2Te_{3.14}$ samples decompose by losing excess tellurium, as confirmed by the thermal behavior of tellurium (melitng point of Te ~ 720 K).

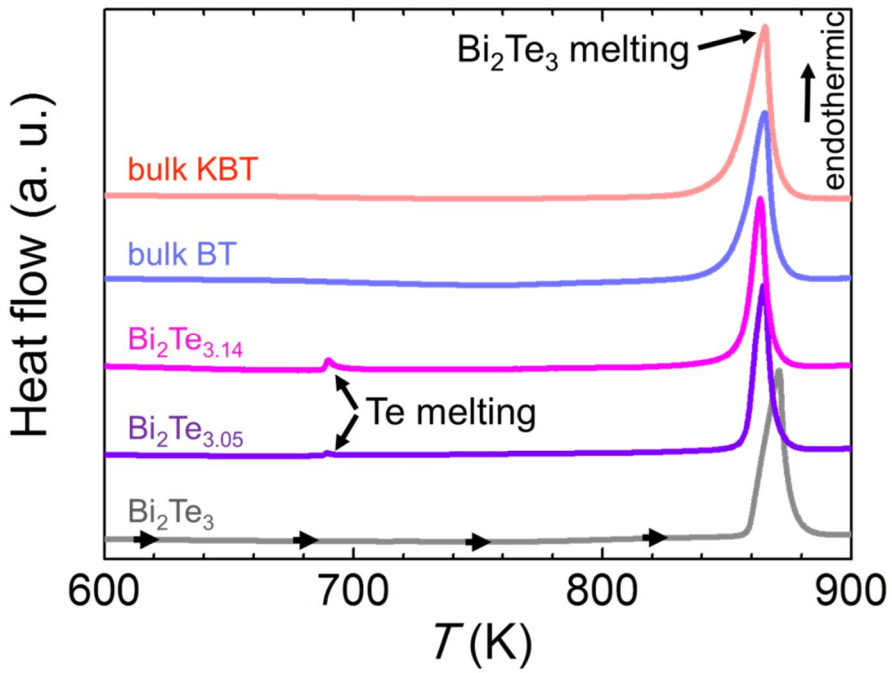

Figure 3.11. Differential scanning calorimetry analysis of Bi_2Te_3, bulk BT, and bulk KBT at a rate of 10 K min^{-1} in comparison with the control $Bi_2Te_{3.05}$ and $Bi_2Te_{3.14}$, demonstrating the phase-homogeneity of bulk BT and KBT.

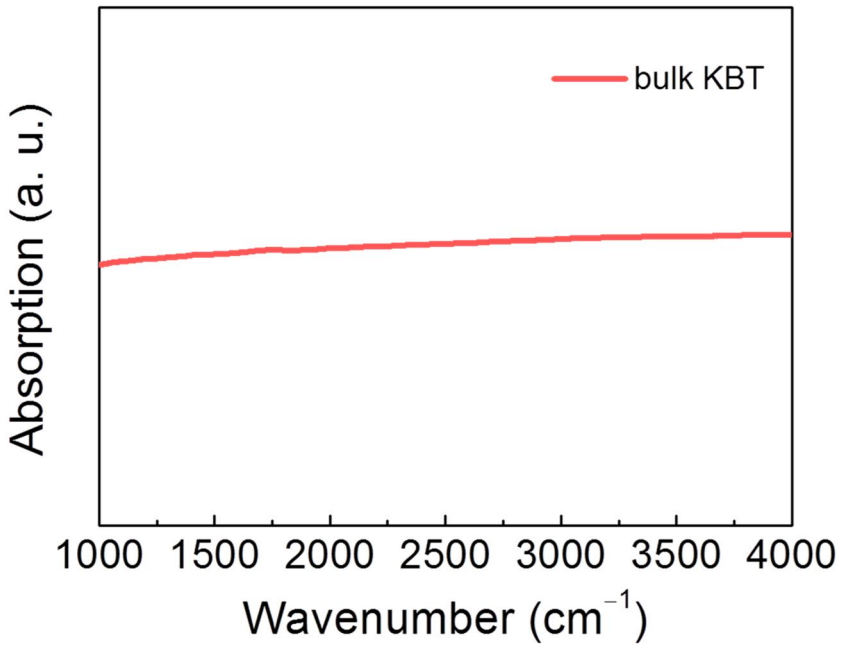

Figure 3.12. FT mid-infrared spectrum of bulk KBT shows no absorption peaks, confirming nearly complete removal of organic residues after spark plasma sintering (SPS).

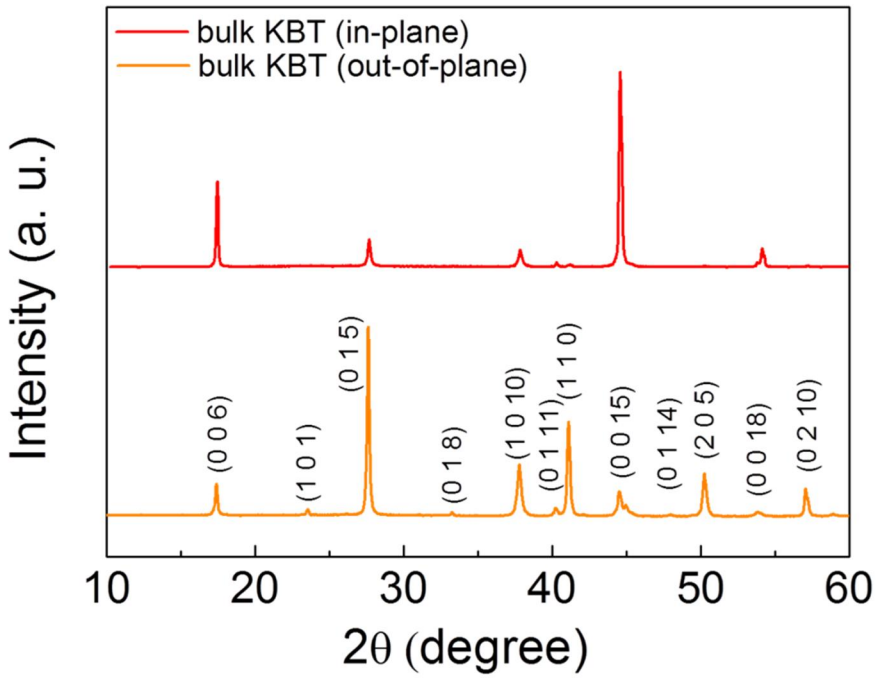

Figure 3.13. In-plane and out-of-plane XRD patterns of bulk KBT, showing highly preferential orientation of the former.

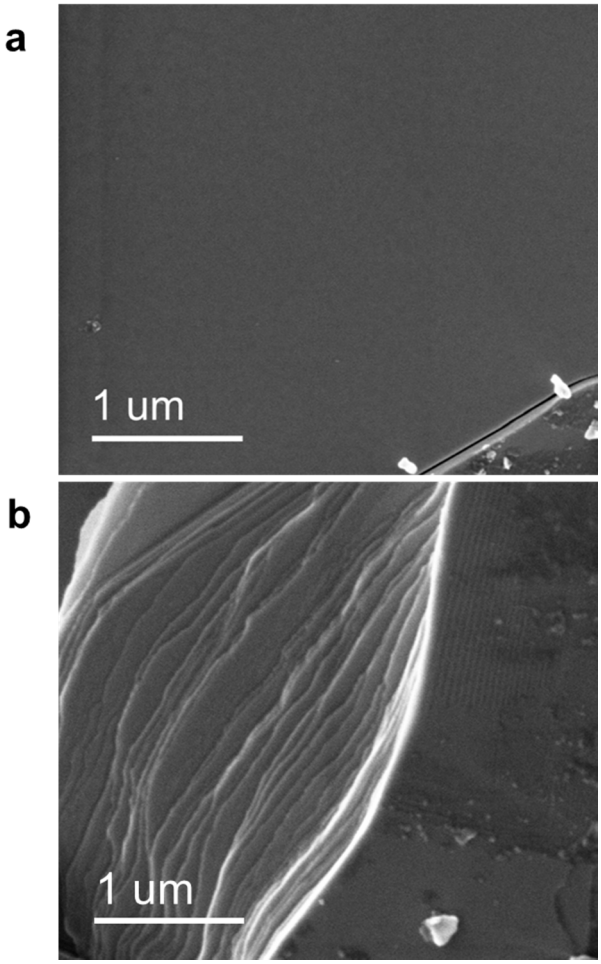

Figure 3.14. Representative SEM images of bulk KBT showing highly oriented two-dimensional morphology of the SPS sample taken along **(a)** the in-plane and **(b)** the out-of-plane directions.

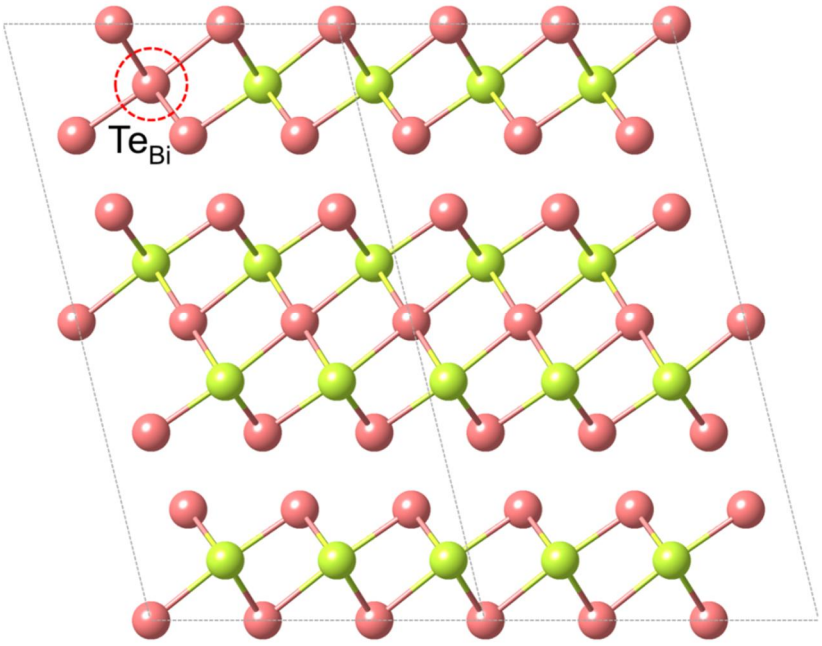

Figure 3.15. The optimized crystal structure of $Bi_{35}Te_{55}$, a supercell of $Bi_2Te_{3.14}$ with Te_{Bi} defect. The red and yellow spheres represent Te and Bi atoms, respectively. Red dotted circle indicates Te_{Bi} antisite, which is a Te atom occupying a Bi site.

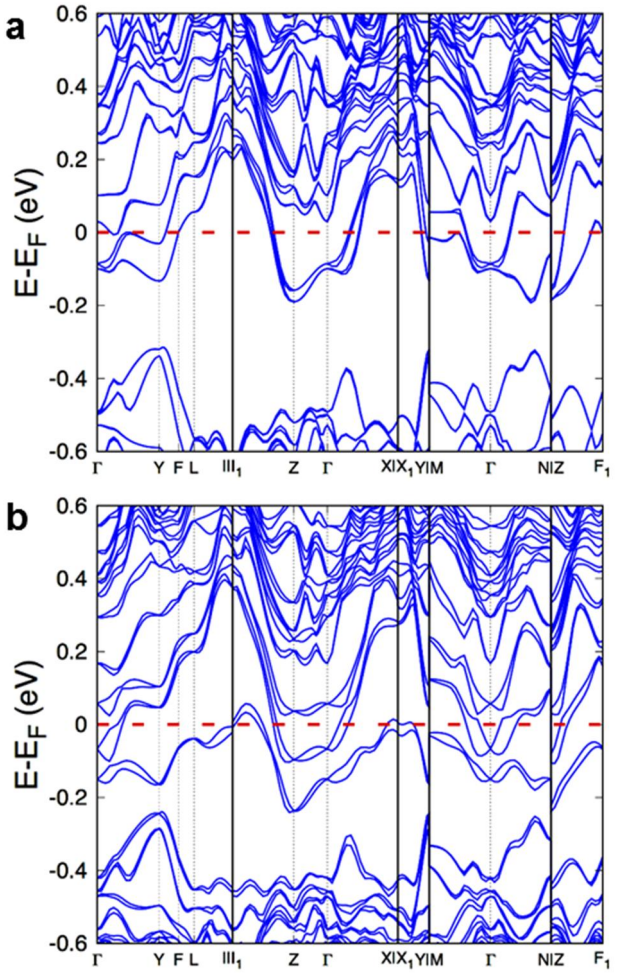

Figure 3.16. The calculated electronic structure of **(a)** $Bi_{35}Te_{55}$, a supercell of $Bi_2Te_{3.14}$ with Te_{Bi} defect and **(b)** $KBi_{35}Te_{55}$, a supercell of $K_{0.057}Bi_2Te_{3.14}$ with K_{int1} (potassium between Bi_2Te_3 layers) and Te_{Bi} defects. The Fermi level is represented by the red dashed line.

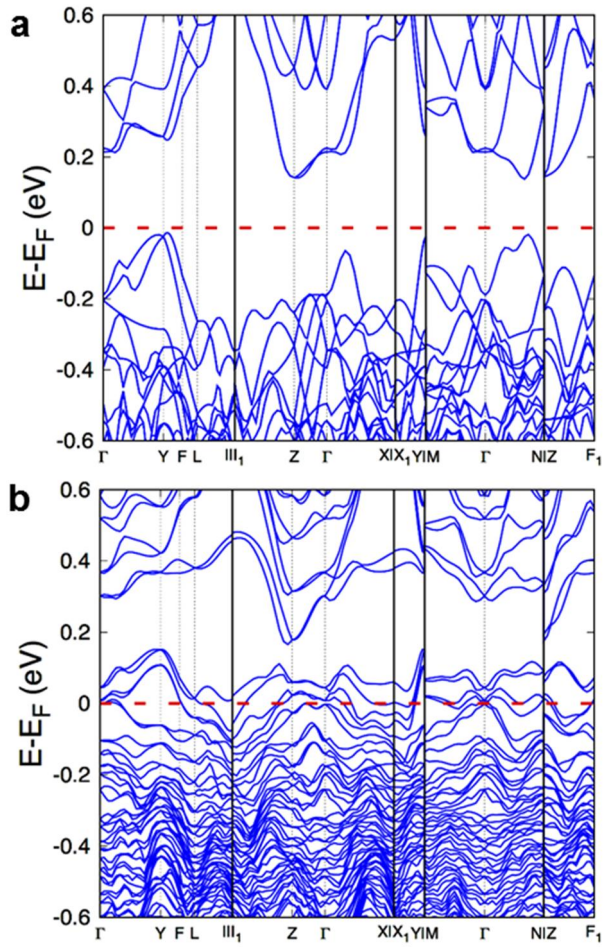

Figure 3.17. The calculated electronic structure of **(a)** $Bi_{36}Te_{54}$, a supercell of Bi_2Te_3 and **(b)** $KBi_{34}Te_{54}$, a supercell of $K_{0.058}Bi_2Te_{3.18}$ with K_{Bi} (potassium substituting Bi) and V_{Bi} (Bi vacancy) defects. The Fermi level is represented by the red dashed line.

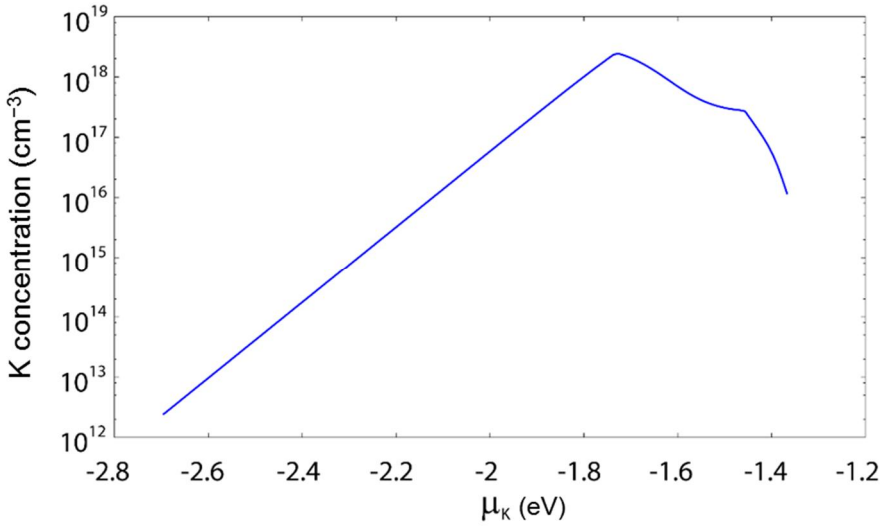

Figure 3.18. The solubility of potassium as a function of chemical potential of potassium (μ_K) in units of eV. The maximum solubility of potassium is achieved at $\mu_K \sim -1.75$ eV.

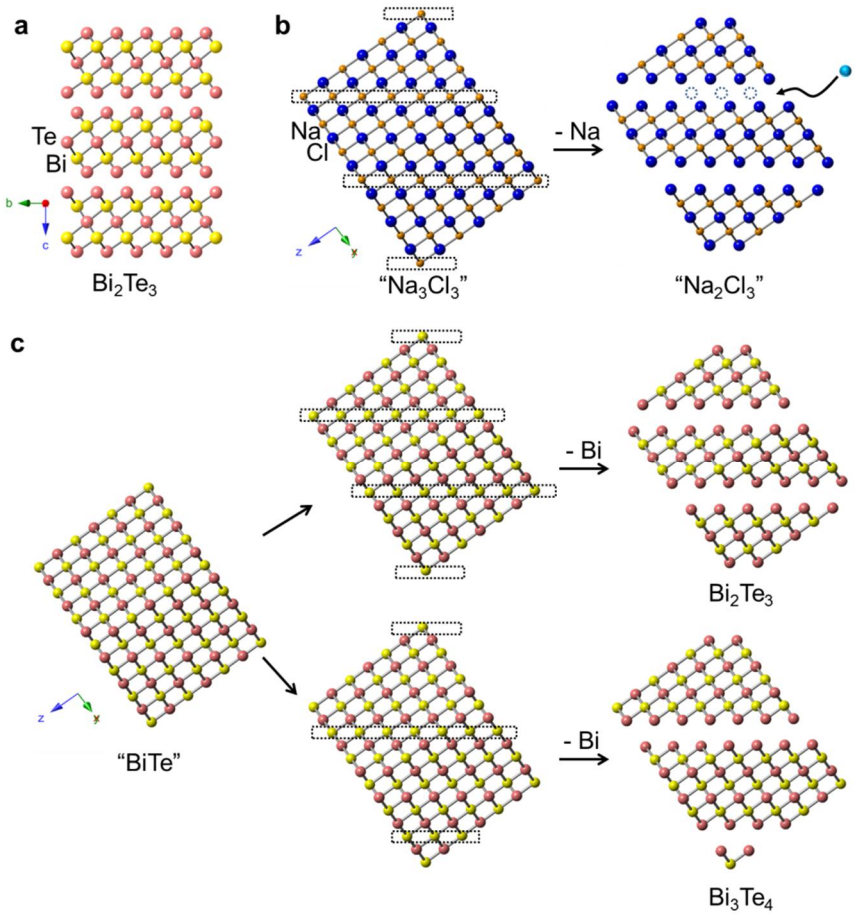

Figure 3.19. **(a)** Crystal structure of Bi_2Te_3. **(b)** Structural relationship between NaCl-type (rock salt) and Bi_2Te_3 showing Bi_2Te_3 is a defective NaCl-type structure and capable of accepting guest species in interlayer space. **(c)** Schematic diagram showing the formation of [Bi_2Te_3] and [Bi_3Te_4] structural motifs from "$Bi_\infty Te_\infty$" by deleting Bi atomic layers periodically.

3.3.3 TEM Analysis

The cross-sectional HAADF-STEM image of the bulk BT viewed down the [-100] axis shows moderate structural dislocations propagating along the in-plane direction (Figure 3.20). The enlarged image on the selected area clearly shows the typical lamellar structure of Bi_2Te_3 that consists of five atomic layers and van der Waals gaps (Figure 3.20, inset and Figure 3.21). Elemental mapping examined by STEM-EDS verifies the locations of Bi and Te atoms (Figure 3.22). In contrast, bulk KBT contains considerable lattice modulations along the in-plane direction, including merged lattices and antisites of Te and Bi (Figure 3.23). We assume that positive potassium ions prefer to locate around the tellurium-rich regions, inducing severe structural distortions. The HAADF-STEM image in Figure 3.24 reveals that excess tellurium is intercalated in the interlayer space, thereby merging individual Bi_2Te_3 layers. Along with ideal quintuple atomic layers, extended septuple layers composed of (Te–Bi–Te–Bi–Te–Bi–Te) atomic arrangements are also frequently observed, and respective Bi and Te atoms are confirmed by elemental mapping using STEM-EDS (Figure 3.25 and 3.26). The observation of the $[Bi_3Te_4]$ layers can be understood in light of the defective NaCl structure of Bi_2Te_3.

Elimination of every third Bi atomic layers from $[Bi_\infty Te_\infty]$ yields $[Bi_3Te_4]$ lattices, whereas elimination of every second Bi atomic layers leads to $[Bi_2Te_3]$ lattices (Figure 3.19c). First principles DFT calculations also support that the formation of septuple layers has a very low formation energy, for example, 0.015 eV and 0.168 eV under bismuth-rich and tellurium-rich conditions, respectively.[21] Moreover, Figure 3.25 demonstrates that a single atomic layer of Te replaces that of Bi to occupy the Bi antisites, forming (Te–Bi–Te–Bi–Te–Te–Bi–Te) atomic arrangements, and EDS analysis in HAADF-STEM maps the locations of Bi and Te atoms. It should be noted that the formation of Q–Q bonds is common for chalcogen atoms (Q = S, Se, and Te), which enables a rich structural chemistry of chalcogenide compounds. Polychalcogenide anions have the –2 formal charge, namely, $[Q_n]^{2-}$ with a nearly zero formal charge on internal Q atoms.[22] Accordingly, the formation of (Te–Te) atomic layers should reduce the net negative charge of bulk BT and KBT samples, which explains the stabilization of excess tellurium. At the macroscopic level, the positively charged bismuth-rich and the negatively charged tellurium-rich region seem to compensate each other. Unusual structural domains found in the bulk KBT sample are unique to our synthetic method that provides kinetic

control over a reaction between premade Te nanorods and a Bi source. As a result of the intercalated tellurium atoms, the interlayer gap increases from 0.27 nm to 0.35 nm.

Potassium atoms are not only much lighter than bismuth and tellurium atoms, but also their EELS spectrum significantly overlaps with that of carbon, making it difficult to directly differentiate the former from the latter. Carbon contamination is inevitable for cross-sectional sample preparation for STEM using focused ion beams. However, a previous study reports the clear differentiation of the carbon *K* edge and the potassium L_{23} edge of the EELS spectrum.[23] To confirm the presence and location of potassium atoms in bulk KBT layers, we carried out STEM-EELS elemental scan profile at the atomic level. They occupy the interlayer space as well as the interstitial sites in Bi_2Te_3 layers according to the HAADF-STEM image coupled with the EELS spectrum (Figure 3.27 and 3.28). Since the contrast of HAADF-STEM images is roughly proportional to the square of atomic number (Z),[24] the atoms marked by arrows can be identified as potassium. Moreover, the EELS spectrum affirms that the intercalated atoms pointed out by orange arrows are potassium. The interlayer gap increases from 0.27 nm to 0.32 nm which provides enough space to adopt potassium at the

octahedral sites (Figure 3.29).

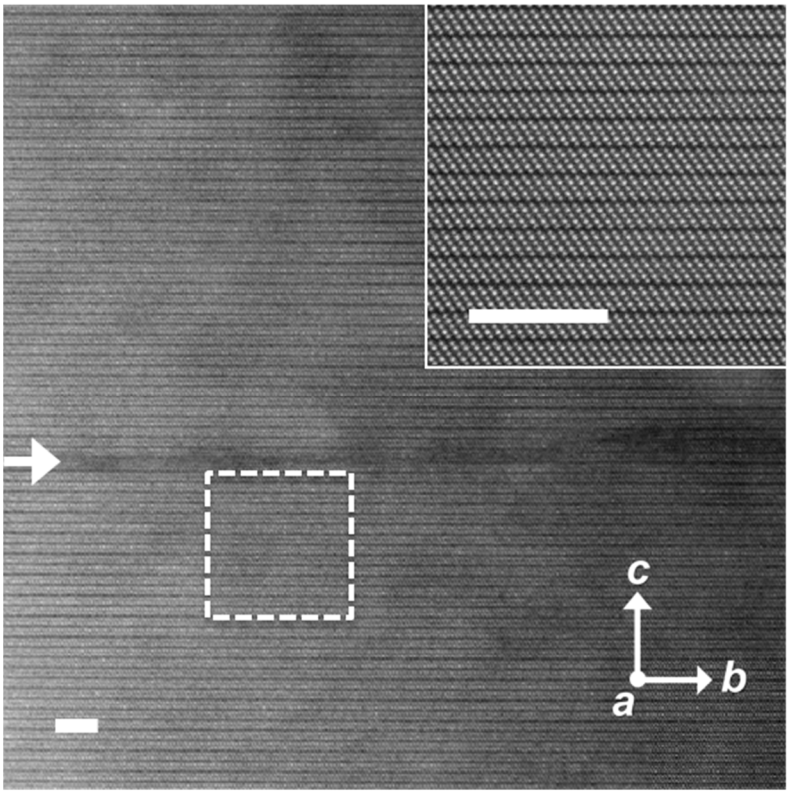

Figure 3.20. A typical low-magnification STEM image of bulk BT showing moderate structural dislocations propagating along the in-plane direction (white arrow). Inset: high-angle annular dark-field STEM (HAADF-STEM) image enlarged from the box showing ideal Bi_2Te_3 structure that consists of quintuple atomic layers of Bi and Te atoms stacked by van der Waals interactions along the *c* axis. Scale bar, 5 nm.

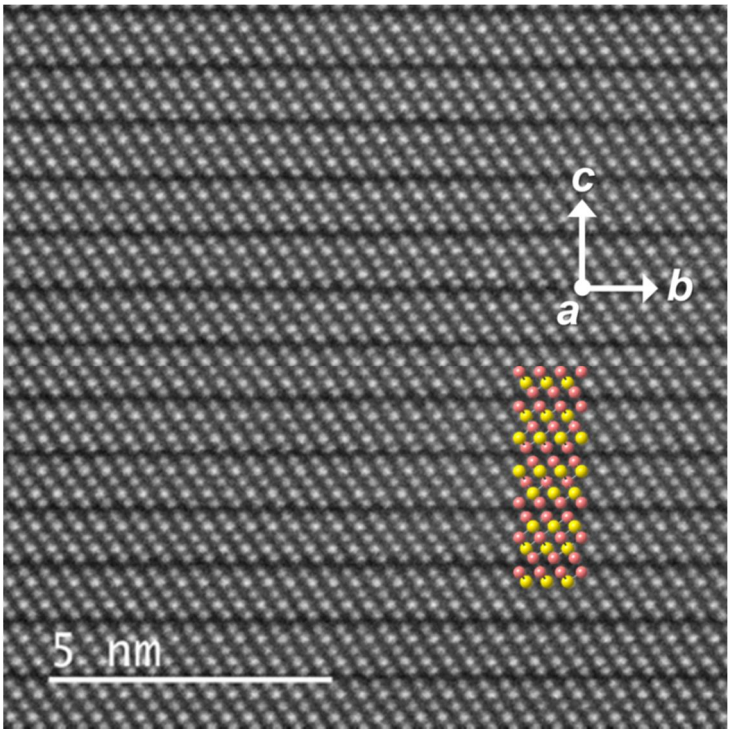

Figure 3.21. A cross-sectional high-angle annular dark-field (HAADF) STEM image of BT down the [-100] axis clearly shows typical lamellar structure of Bi_2Te_3 that is composed of five atomic layers and van der Waals gaps.

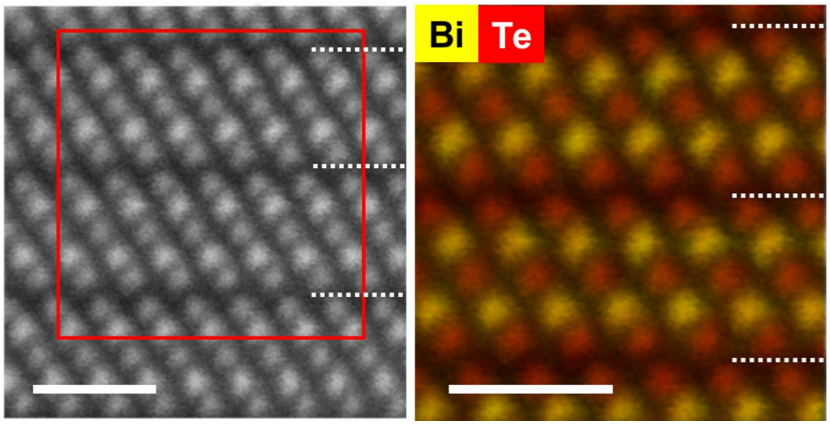

Figure 3.22. Elemental mapping of bulk BT sample by STEM energy dispersive X-ray spectroscopy (STEM-EDS) clearly identifying Bi (yellow) and Te (red) atoms. Van der Waals gaps are shown in dashed lines. Scale bar, 1 nm.

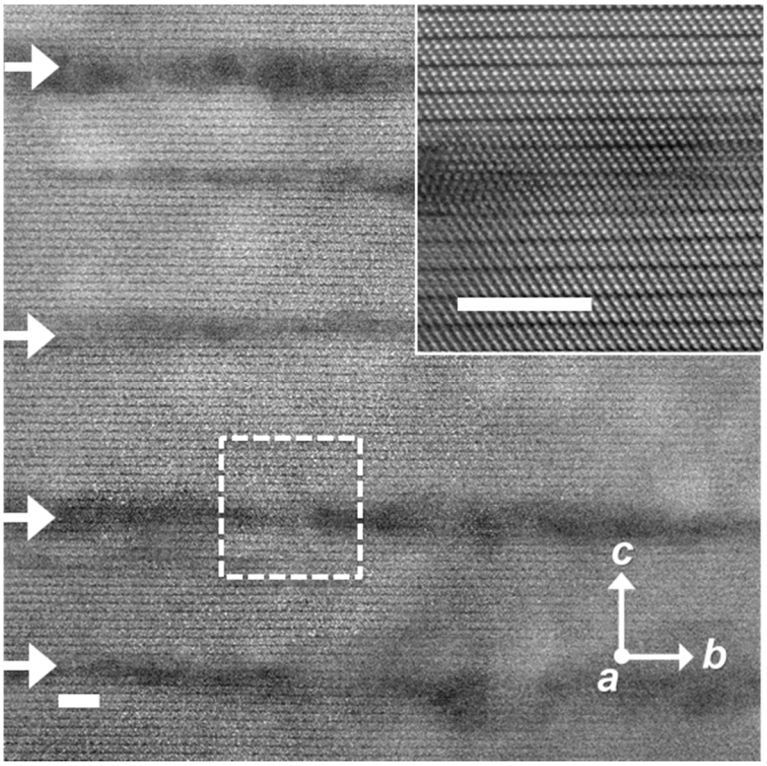

Figure 3.23. A typical low-magnification STEM image of bulk KBT. Structural modulations propagating along the in-plane direction is evident (white arrow). Inset: Enlarged image of the boxed region clearly shows severe structural dislocations. Scale bar, 5 nm.

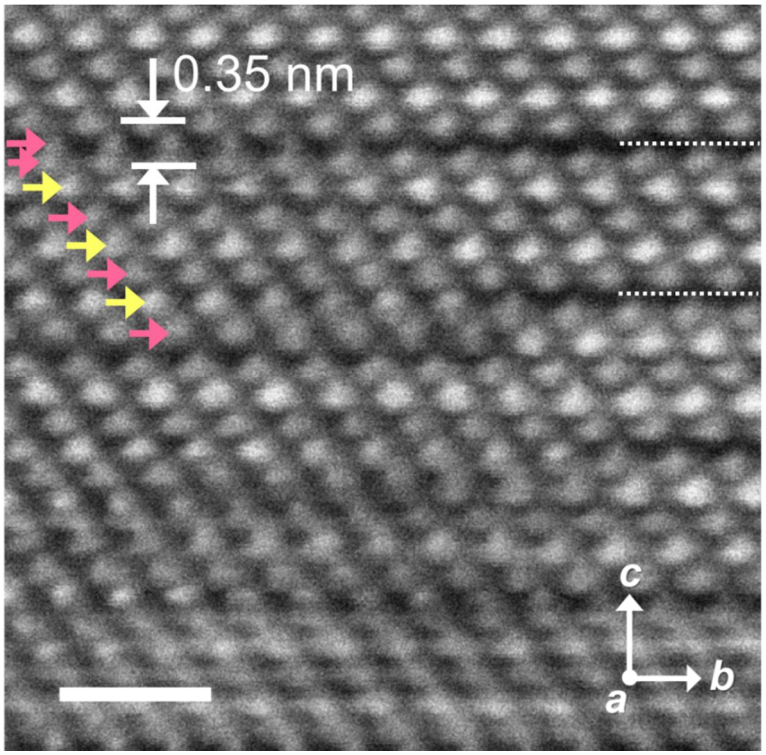

Figure 3.24. A HAADF-STEM image of bulk KBT reveals a septuple atomic layer of [Bi_3Te_4] in a structural motif and Te atoms intercalated in the van der Waals gap (dashed line) of Bi_2Te_3. Expanded interlayer distance of 0.35 nm due to Te intercalation is shown. Te and Bi atoms are indicated by pink and yellow arrows, respectively. Scale bar, 1 nm.

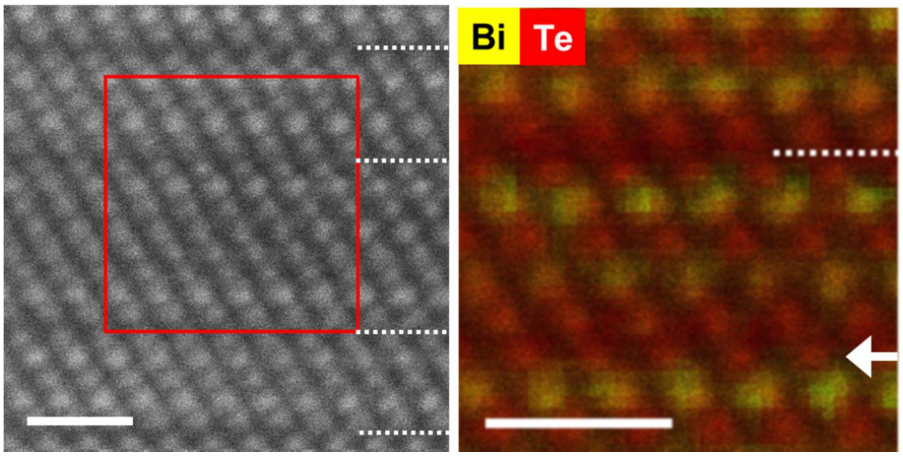

Figure 3.25. Elemental mapping of bulk KBT sample examined by STEM-EDS showing (Te–Bi–Te–Bi–Te–Te–Bi–Te) atomic arrangement. An atomic layer of Te replacing that of Bi to form Te–Te bonds is clearly seen (white arrow). Bi and Te atoms are in colored yellow and red, respectively. Scale bar, 1 nm.

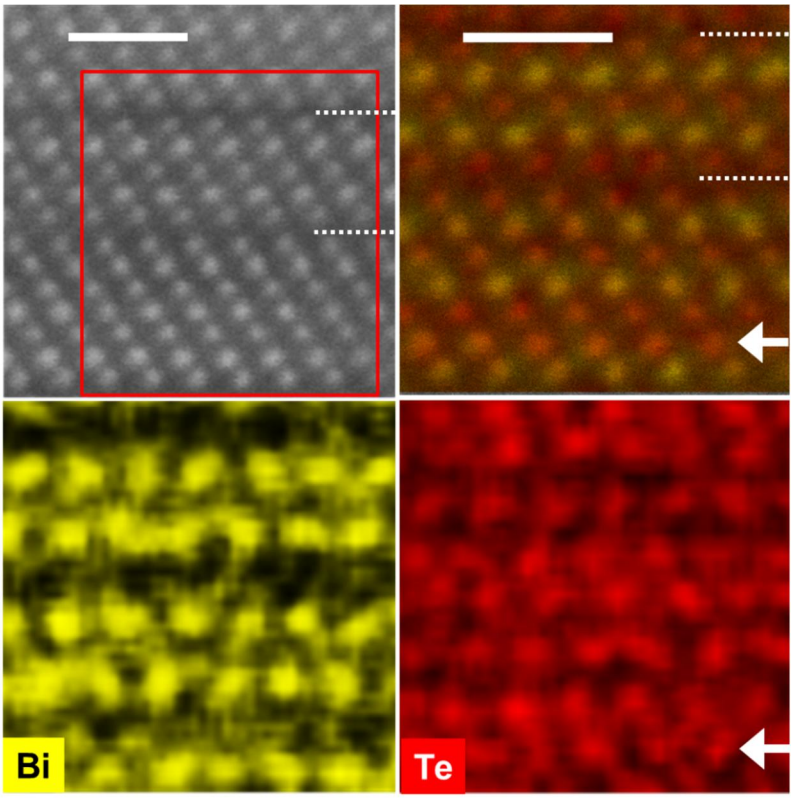

Figure 3.26. Elemental mapping of bulk KBT sample examined by STEM-EDS showing a structural motif of (Te–Bi–Te–Bi–Te–Te–Bi–Te) atomic arrangement (a terminal atomic layer of Te at the bottom was omitted in the image). An atomic layer of Te replacing that of Bi to form Te–Te bonds is clearly shown (white arrow). Bi and Te atoms are in yellow and red colors, respectively. Scale bar, 1 nm.

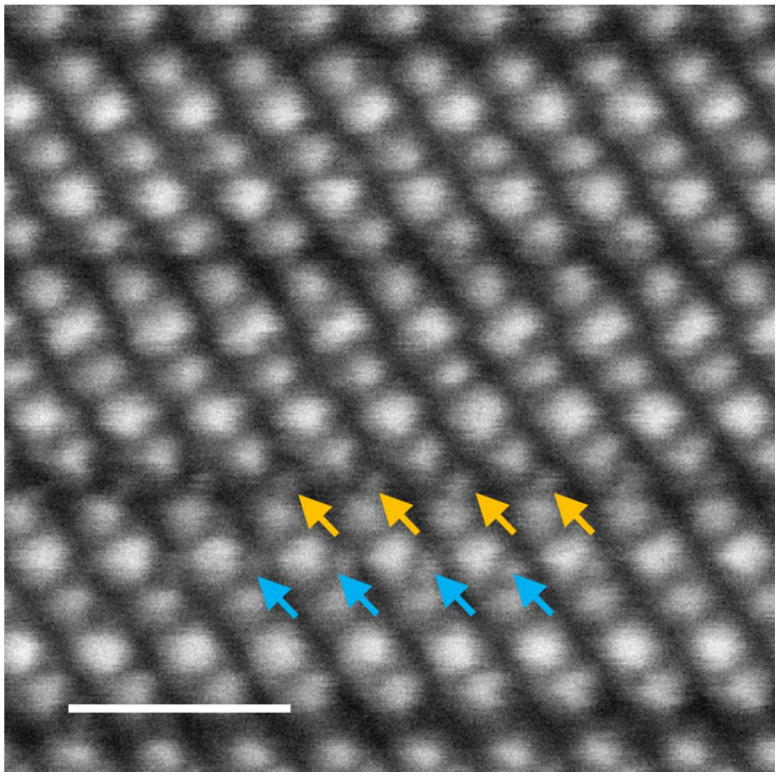

Fig. 3.27. A HAADF-STEM image of bulk KBT showing potassium ions occupying the interstitial (blue arrow) and interlayer (orange arrow) sites of Bi_2Te_3 layers. Scale bar, 1 nm.

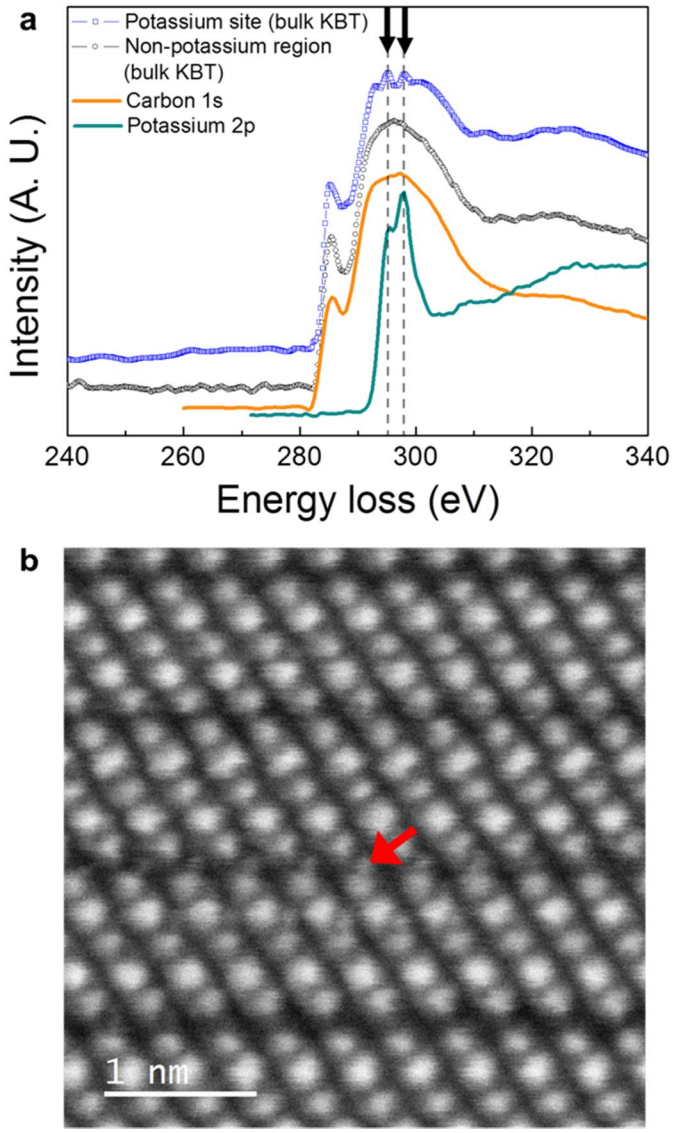

Figure 3.28. STEM-electron energy loss spectroscopy (EELS) spectra of bulk KBT. **(a)** The spectrum obtained by pinpointing the interlayer atom (red arrow in (b)) clearly shows a signal for potassium indicated by black arrows (blue line). In contrast, the spectrum by scanning the

non-potassium area only shows a signal for carbon. The reference spectra for carbon *K* edge (1s) and potassium L_{23} (2p) edge (KCl crystal) are obtained from EELS Atlas (Gatan Inc. 1983). **(b)** The EELS spectrum for potassium was collected at the interlayer atom indicated by the red arrow shown in the HAADF-STEM image.

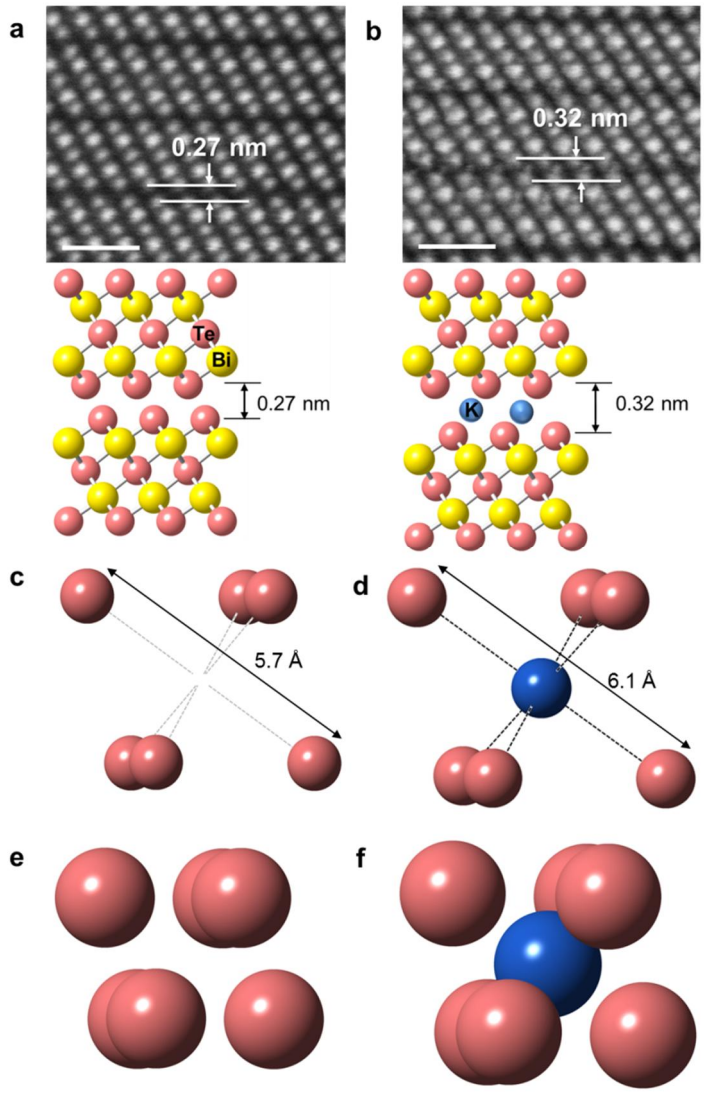

Figure 3.29. HAADF-STEM images of **(a)** bulk BT and **(b)** bulk KBT show the increase in interlayer distance from 0.27 nm to 0.32 nm due to potassium incorporation. Calculated Te–Te interatomic distances from octahedral environment are **(c)** 5.7 Å for bulk BT and **(d)** 6.1 Å for bulk KBT. We consider covalent radius of Te is 1.36 Å and K^+ ionic radius is

1.38 Å at the octahedral environment,[25] and their structural model for interlayer octahedral space for bulk BT and bulk KBT are shown in **(e)** and **(f)**, respectively. The increased Te–Te interatomic distance of 6.1 Å is sufficient for accepting a K^+ ion (2 × (1.36 Å + 1.38 Å) < 6.1 Å). Red, yellow, and blue dots indicate Te, Bi, and K, respectively. Scale bar, 1 nm.

3.3.4 Thermoelectric Peoperties

Afterwards, we conducted TE property characterization of the bulk BT and KBT samples. We also prepared control samples with nominal compositions of Bi_2Te_3 and $K_{0.02}Bi_2Te_3$ in ingot form by the conventional high-temperature solid-state reaction. All of them were SPS processed and measured along the in-plane direction (normal to the pressing direction). The temperature-dependent Seebeck coefficient (*S*) of the bulk BT, bulk KBT, and Bi_2Te_3 in the range of 300 K to 470 K is negative, indicating that electrons are the major charge carrier (Figure 3.30a). Because bulk BT and KBT cannot be obtained by conventional synthetic methods, it is important to understand the origin of their n-type conduction behavior. Accordingly, we calculated their electronic structures based on DFT by using the same defect conditions confirmed by the EELS and EDS results. The n-type characteristics of the bulk BT arise from the antisite defects of Te_{Bi} (Te atoms occupying a Bi lattice site) caused by the tellurium-rich composition ($Bi_2Te_{3.14}$), which is confirmed both experimentally by HAADF-STEM studies (Figure 3.25) and theoretically by DFT calculations. We considered four types of point defects: Bi and Te vacancies denoted as V_{Bi} and V_{Te} and Bi and Te antisites denoted as Bi_{Te} and Te_{Bi}, respectively. Our

calculation verifies that Te_{Bi} is the most stable defect with the low formation energy of 0.379 eV under tellurium-rich condition. Such a defect condition was simulated in $Bi_{35}Te_{55}$, a supercell of $Bi_2Te_{3.14}$ (Figure 3.15). It caused a shift in the Fermi level into the conduction band, and resulted in an n-type electronic structure by DFT (Figure 3.16).

The unusual n-type behavior of bulk KBT is of paramount importance. In general, a high temperature solid-state reaction distributes participating atoms statistically to form a thermodynamically stable phase. As a result, monovalent dopants that substitute higher-valent cations should induce p-type conduction. In fact, alkali metals are effective p-type dopants for TE materials such as SnSe and PbTe.[26] When potassium was introduced to Bi_2Te_3 via a conventional high-temperature solid-state reaction in order to form $K_{0.02}Bi_2Te_3$, the expected p-type conduction was generally observed due to the formation of substitutional acceptor defects (K_{Bi}). In contrast, potassium cations in bulk KBT occupy the interlayer (K_{int1}) and interstitial sites (K_{int2}) according to the STEM-EELS results (Figure 3.27 and 3.28). DFT calculations reveal that K_{int1} pushes the Fermi level up to the conduction band to give an n-type electronic structure,

whereas K_{Bi} shifts it down to the valence band to give a p-type electronic structure (Figure 3.16 and 3.17). To confirm this experimentally, we measured electron concentration (n_e) and mobility (μ_e) by the Hall effect analysis. By incorporating potassium, the n_e value at 300 K rose from ~3.14×10^{19} cm^{-3} to ~4.63×10^{19} cm^{-3}, and the μ_e value at 300 K increased from ~142 cm^2 V^{-1} s^{-1} to ~171 cm^2 V^{-1} s^{-1} (Figure 3.31), verifying that potassium acts as an excellent electron donor.

Importantly, despite ~1.5 times larger electron concentration of bulk KBT than that of bulk BT, both bulk BT and KBT samples have a comparable S value (–182 μV K^{-1}) at 300 K. This is in strong contrast with typical transport behavior of TE materials in that the S value is inversely proportional to carrier concentration for heavily doped semiconductors.[4] Their S values at 300 K are significantly higher than –135 μV K^{-1} of Bi_2Te_3. The absolute magnitude of S for bulk KBT increases with temperature until 350 K and decreases at higher temperature because of bipolar conduction. The unusual carrier type of potassium reflects the uniqueness of our nanochemical synthetic approach to develop bulk materials with unusual properties, which cannot be achievable by conventional preparative methods.

Furthermore, we could incorporate sodium to BT nanotube using a similar synthetic procedure, demonstrating general applicability of our process. The typical composition of Na-doped BT analyzed by ICP-AES is $Na_{0.05}Bi_2Te_{3.11}$ (NaBT), which also exhibits n-type behavior with negative *S* values in the entire temperature range (Figure 3.32).

The temperature dependence of electrical conductivity (σ) for all the samples decreases with increasing temperature, a typical behavior of a heavily doped semiconducting material (Figure 3.30b). The effect of the potassium addition is evident in σ value, nearly twice increase from ~711 S cm^{-1} of bulk BT to ~1265 S cm^{-1} of bulk KBT at 300 K. This enhancement in σ can be attributed to the enhancement in both n_e and μ_e according to the Hall measurement. In contrast, when potassium was doped to Bi_2Te_3 to form $K_{0.02}Bi_2Te_3$ for the control sample, the σ value significantly decreased from ~1142 S cm^{-1} to ~448 S cm^{-1}.

The *PF* as a function of temperature is shown in Figure 3.30c. The *PF* value of bulk KBT at 300 K is ~42.1 μW cm^{-1} K^{-2}, reaches to a maximum ~42.8 μW cm^{-1} K^{-2} at 323 K, and decreases with further increasing temperature. The *PF* value of bulk KBT is substantially larger than that of bulk BT (~23.4 μW cm^{-1} K^{-2} at 300 K), attributed to its higher σ with the comparable *S* value. It should be noted that the

maximum value of bulk KBT is surprisingly close to ~47 μW cm^{-1} K^{-2} of the single crystal sample and larger than ~35 μW cm^{-1} K^{-2} of state-of-the-art n-type $Bi_2Te_{3-x}Se_x$ materials.[5,27] The control sample $K_{0.02}Bi_2Te_3$ exhibited a much lower *PF* value of ~18.5 μW cm^{-1} K^{-2} at 323 K.

The total thermal conductivity (κ_{tot}) in Figure 3.30d shows that κ_{tot} of bulk KBT is lower than those of the other samples. Its κ_{tot} value at 300 K is ~1.30 W m^{-1} K^{-1} and drops to a minimum of ~1.26 W m^{-1} K^{-1} at 350 K in comparison to ~1.57 W m^{-1} K^{-1} at 300 K and ~1.53 W m^{-1} K^{-1} at 350 K of bulk BT. The κ_{tot} value of bulk KBT at 300 K along the out-of-plane direction is much lower at ~0.54 W m^{-1} K^{-1} (Figure 3.33). Its ratio of κ_{tot}, in-plane/κ_{tot}, out-of-plane is ~2.4, which is comparable to ~2 of a $Bi_2Te_{3-x}Se_x$ (x = 0.075, 0.15) single crystal.[27] This is much greater than ~1.5 for the highly oriented $Bi_2Te_{2.7}Se_{0.3}$ nanobulk sample that is ball-milled and then hot-pressed (BM-HP) multiple times to induce a high in-plane orientation.[27] This significantly anisotropic thermal conduction agrees well with the highly oriented bulk KBT, as confirmed by powder X-ray diffraction patterns (Figure 3.13). Above 350 K, the κ_{tot} increases with temperature, indicative of the bipolar contributions from electron and hole carriers that are thermally

generated.[28] We observe that the κ_{latt} value of bulk KBT (~0.66 W m^{-1} K^{-1}) is much lower than that of bulk BT (~1.21 W m^{-1} K^{-1}) at 300K (Figure 3.30e). This can be explained by the cross-sectional HAADF-STEM and SEM images, revealing that various structural dislocations such as strips of modulating Bi_mTe_n layers, broken atomic layers, and defect sites are generated upon the incorporation of potassium (Figure 3.23 and 3.34). These dislocations act as effective scattering centers of heat-carrying phonons at the atomic- and nano-scale.

Figure 3.30f shows a TE figure of merit *ZT* as a function of temperature. A *ZT* value of bulk KBT at 300 K is ~1.0, and increases to a maximum *ZT* of ~1.14 at 350 K, which is higher than the *ZT* values of the state-of-the-art n-type Bi_2Te_3-based materials that operate near room temperature.[5,27] In fact, the ubiquitous tellurium defects in pure n-type Bi_2Te_3 are known to decrease *PF*, resulting in the reduction of *ZT*. High *ZT* n-type Bi_2Te_3-based materials mostly contain Se or S,[29] which partially replaces Te to achieve enhanced *PF* and *ZT* values. However, alloying with smaller congeners of Te shifts the temperature of ZT_{max} higher due to an increase in the band gap energy, resulting in a mismatch with that of the state-of-the-art p-type materials. For example, the best p-type $Bi_{0.5}Sb_{1.5}Te_3$ exhibits ZT_{max} at 340 K.[10c] It should be

noted that the high TE performance of bulk KBT arises mainly from the enhanced *PF* derived from the electron donating potassium dopants, which is in strong contrast with the conventional synthetic methods for producing high *ZT* TE materials.

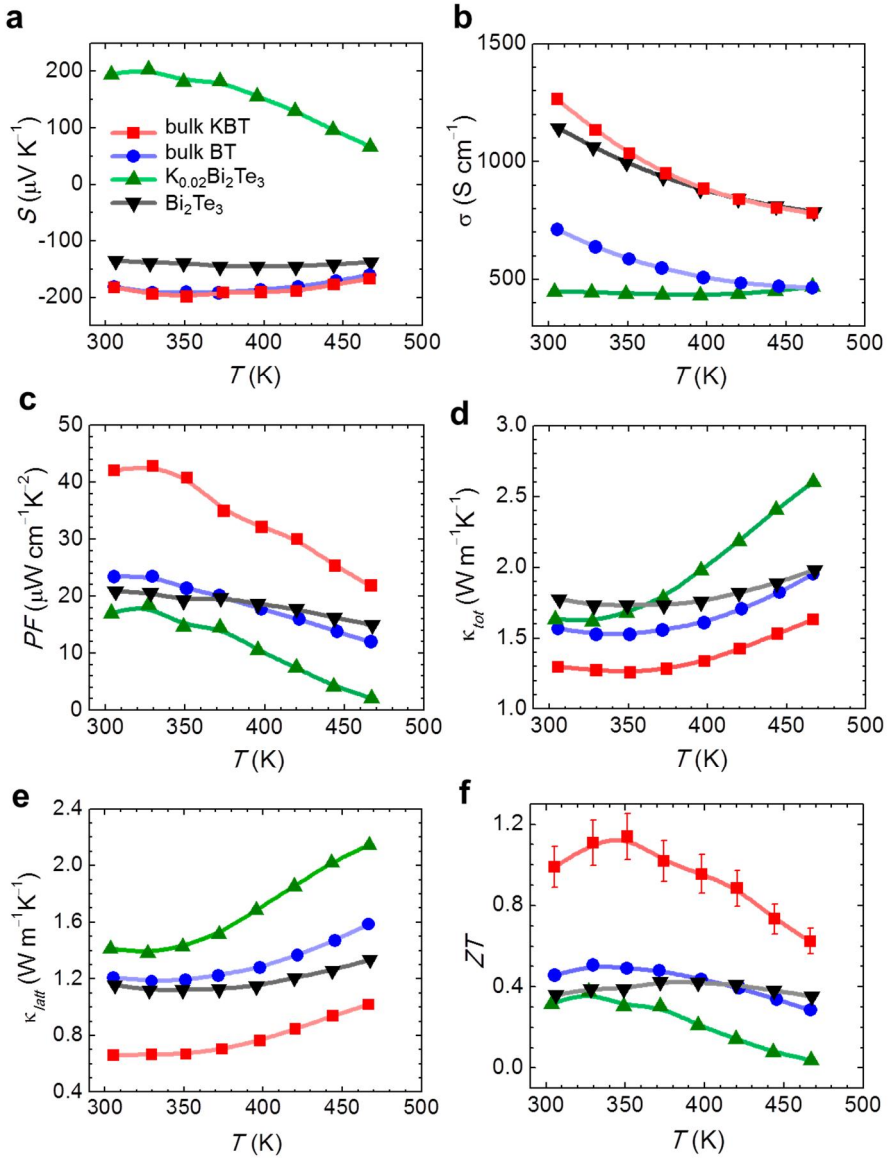

Figure 3.30. Thermoelectric properties along the in-plane direction (*ab* plane) as a fuction of temperature for bulk BT and KBT in comparison with those of the control Bi_2Te_3 and $K_{0.02}Bi_2Te_3$ samples. All samples

are SPS processed. **(a)** Seebeck coefficient (S), **(b)** Electrical conductivity (σ), **(c)** Power factor (PF)**, (d)** Total thermal conductivity (κ_{tot}), **(e)** Lattice thermal conductivity (κ_{latt}), and **(f)** ZT values.

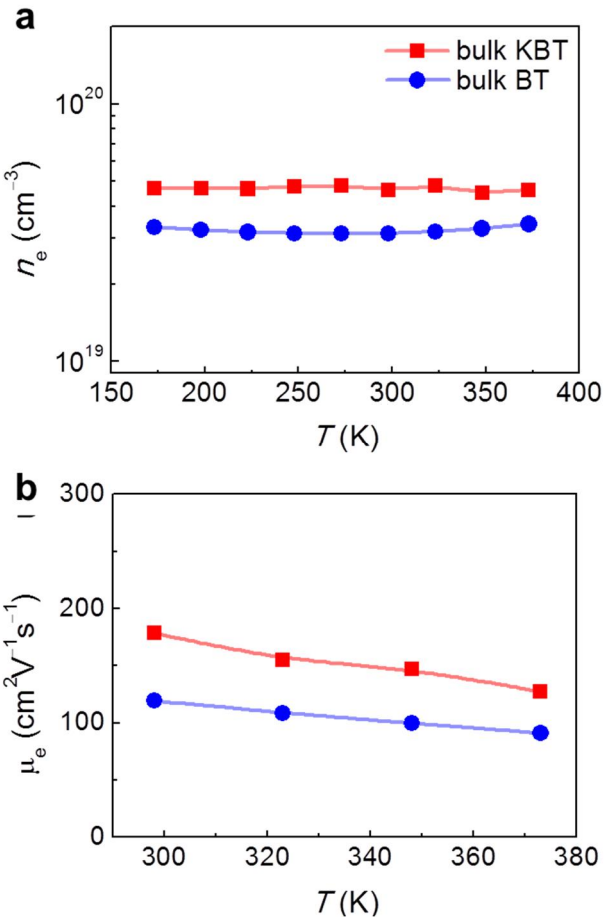

Figure 3.31. Electron concentration and mobility of bulk BT and KBT as a function of temperature showing increase in **(a)** electron concentration (n_e) and **(b)** mobility (μ_e) upon potassium incorporation.

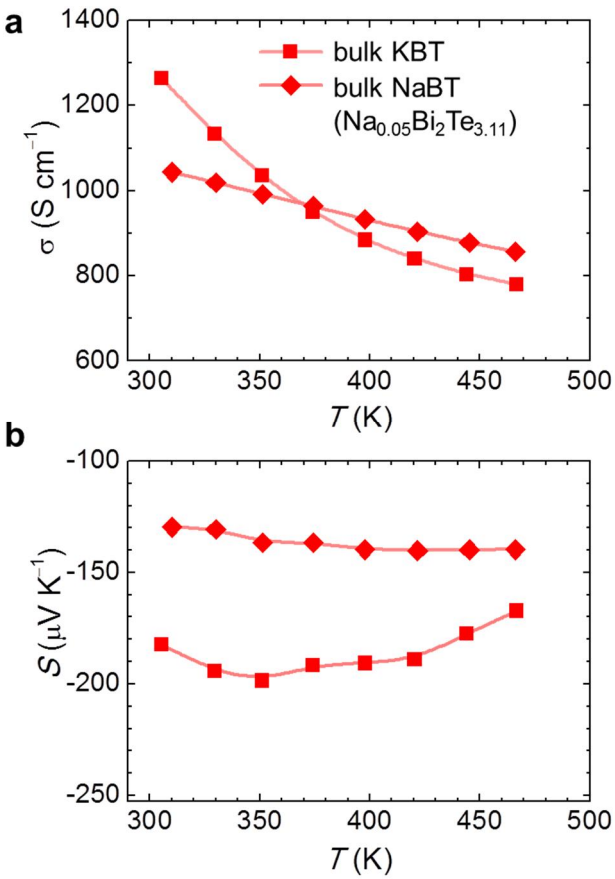

Figure 3.32. Electrical transport properties of bulk $Na_{0.05}Bi_2Te_{3.11}$ (NaBT) in comparison to bulk KBT as a function of temperature. **(a)** Electrical conductivity and **(b)** Seebeck coefficient.

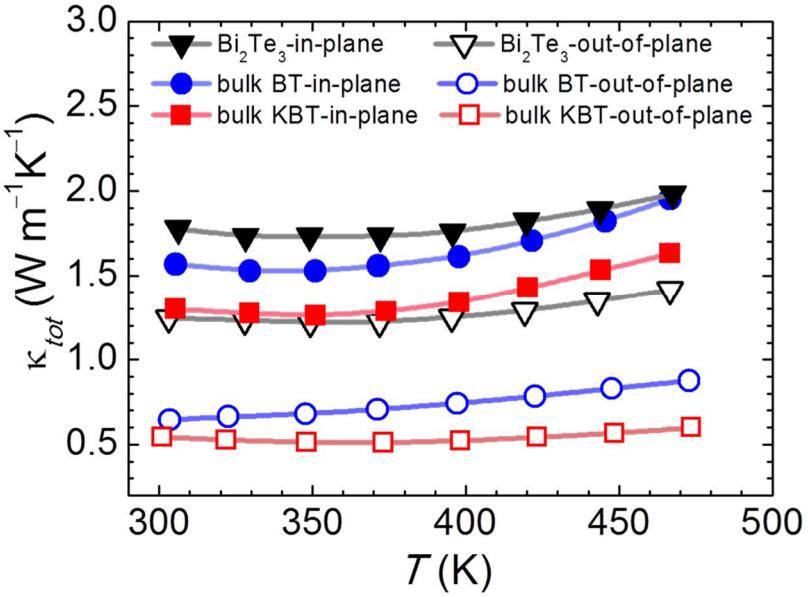

Figure 3.33. Thermal conductivity of Bi_2Te_3, bulk BT, and bulk KBT along the in-plane and out-of-plane directions showing significant anisotropy in thermal transport of the samples.

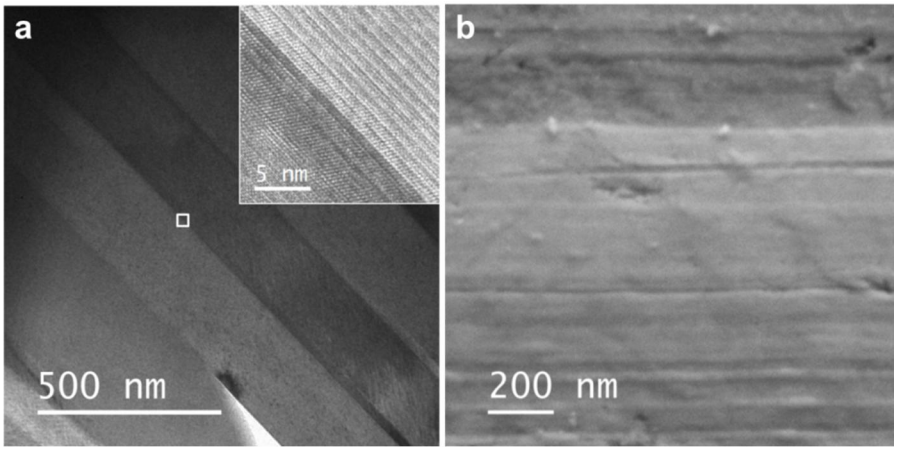

Figure 3.34. The cross-sectional high resolution **(a)** TEM and **(b)** SEM images of bulk KBT. The stripe pattern shown in the images is the crystal domains stacked along the pressing direction of the SPS process.

3.4 Conclusion

We demonstrate that a new class of solid-state bulk compounds that do not obey the compositions dictated by phase equilibrium can be synthesized via nanochemistry. The resulting compounds have never been obtained by other methods and exhibit markedly improved TE performance. Potassium cations, which serve as unconventional electron donors, are key to the surprisingly high *PF* and the resulting high n-type TE performance. With consideration of crystal structures and bonding behaviors, our current synthetic method can be used to produce a new family of materials with novel physical and chemical characteristics. Consequently, phase diagrams of solids can be largely reconstructed with a greatly expanded family of materials on the shelf. This approach can be used to synthesize novel materials with enhanced characteristics for various applications.

Parts of this research were published in "Extraordinary Off-Stoichiometric Bismuth Telluride for Enhanced n-Type Thermoelectric Power Factor" *Journal of American Chemical Society*, **2016**, ASAP.

3.5 References

[1] a) Erwin, S. C.; Zu, L. J.; Haftel, M. I.; Efros, A. L.; Kennedy, T. A.; Norris, D. J. *Nature* **2005**, *436*, 91. b) Boles, M. A.; Ling, D.; Hyeon, T.; Talapin, D. V. *Nat. Mater.* **2016**, *15*, 141. c) Lee, J.; Yang, J.; Kwon, S. G.; Hyeon, T. *Nat. Rev. Mater.* **2016**, *1*, 16034.

[2] Rowe, D. M., *Thermoelectrics handbook : Macro to Nano*. CRC/Taylor & Francis: Boca Raton, FL, **2006**.

[3] a) Dresselhaus, M. S.; Chen, G.; Tang, M. Y.; Yang, R. G.; Lee, H.; Wang, D. Z.; Ren, Z. F.; Fleurial, J. P.; Gogna, P. *Adv. Mater.* **2007**, *19*, 1043. b) Bell, L. E. *Science* **2008**, *321*, 1457. c) Zeier, W. G.; Zevalkink, A.; Gibbs, Z. M.; Hautier, G.; Kanatzidis, M. G.; Snyder, G. J. *Angew. Chem. Int. Ed.* **2016**, *55*, 6826.

[4] Sootsman, J. R.; Chung, D. Y.; Kanatzidis, M. G. *Angew. Chem. Int. Ed.* **2009**, *48*, 8616.

[5] Liu, W. S.; Zhang, Q. Y.; Lan, Y. C.; Chen, S.; Yan, X.; Zhang, Q.; Wang, H.; Wang, D. Z.; Chen, G.; Ren, Z. F. *Adv. Energy Mater.* **2011**, *1*, 577.

[6] a) Hochbaum, A. I.; Chen, R. K.; Delgado, R. D.; Liang, W. J.; Garnett, E. C.; Najarian, M.; Majumdar, A.; Yang, P. D. *Nature* **2008**, *451*, 163. b) Minnich, A. J.; Dresselhaus, M. S.; Ren, Z. F.;

Chen, G. *Energy Environ. Sci.* **2009**, *2*, 466. c) Vineis, C. J.; Shakouri, A.; Majumdar, A.; Kanatzidis, M. G. *Adv. Mater.* **2010**, *22*, 3970. d) Skoug, E. J.; Morelli, D. T. *Phys. Rev. Lett.* **2011**, *107*, 235901. e) Liu, H. L.; Shi, X.; Xu, F. F.; Zhang, L. L.; Zhang, W. Q.; Chen, L. D.; Li, Q.; Uher, C.; Day, T.; Snyder, G. J. *Nat. Mater.* **2012**, *11*, 422. f) Son, J. S.; Choi, M. K.; Han, M. K.; Park, K.; Kim, J. Y.; Lim, S. J.; Oh, M.; Kuk, Y.; Park, C.; Kim, S. J.; Hyeon, T. *Nano Lett.* **2012**, *12*, 640. g) Son, J. S.; Zhang, H.; Jang, J.; Poudel, B.; Waring, A.; Nally, L.; Talapin, D. V. *Angew. Chem. Int. Ed.* **2014**, *53*, 7466. h) Zhao, L. D.; Lo, S. H.; Zhang, Y. S.; Sun, H.; Tan, G. J.; Uher, C.; Wolverton, C.; Dravid, V. P.; Kanatzidis, M. G. *Nature* **2014**, *508*, 373. i) Beekman, M.; Morelli, D. T.; Nolas, G. S. *Nat. Mater.* **2015**, *14*, 1182. j) Wan, C. L.; Gu, X. K.; Dang, F.; Itoh, T.; Wang, Y. F.; Sasaki, H.; Kondo, M.; Koga, K.; Yabuki, K.; Snyder, G. J.; Yang, R. G.; Koumoto, K. *Nat. Mater.* **2015**, *14*, 622. k) Zeier, W. G.; Schmitt, J.; Hautier, G.; Aydemir, U.; Gibbs, Z. M.; Felser, C.; Snyder, G. J. *Nat. Rev. Mater.* **2016**, *1*, 16032. l) Zhao, L. D.; Tan, G. J.; Hao, S. Q.; He, J. Q.; Pei, Y. L.; Chi, H.; Wang, H.; Gong, S. K.; Xu, H. B.; Dravid, V. P.; Uher, C.; Snyder, G. J.; Wolverton, C.; Kanatzidis, M. G. *Science* **2016**, *351*, 141.

[7] Hsu, K. F.; Loo, S.; Guo, F.; Chen, W.; Dyck, J. S.; Uher, C.; Hogan, T.; Polychroniadis, E. K.; Kanatzidis, M. G. *Science* **2004**, *303*, 818.

[8] a) Biswas, K.; He, J. Q.; Zhang, Q. C.; Wang, G. Y.; Uher, C.; Dravid, V. P.; Kanatzidis, M. G. *Nat. Chem.* **2011**, *3*, 160. b) Biswas, K.; He, J. Q.; Blum, I. D.; Wu, C. I.; Hogan, T. P.; Seidman, D. N.; Dravid, V. P.; Kanatzidis, M. G. *Nature* **2012**, *489*, 414.

[9] a) Sales, B. C.; Mandrus, D.; Williams, R. K. *Science* **1996**, *272*, 1325. b) Paschen, S.; Carrillo-Cabrera, W.; Bentien, A.; Tran, V. H.; Baenitz, M.; Grin, Y.; Steglich, F. *Phys. Rev. B* **2001**, *64*, 214404. c) Christensen, M.; Abrahamsen, A. B.; Christensen, N. B.; Juranyi, F.; Andersen, N. H.; Lefmann, K.; Andreasson, J.; Bahl, C. R. H.; Iversen, B. B. *Nat. Mater.* **2008**, *7*, 811. d) Kim, H.; Kaviany, M.; Thomas, J. C.; van der Ven, A.; Uher, C.; Huang, B. L., *Phys. Rev. Lett.* **2010**, *105*, 265901. e) Rogl, G.; Grytsiv, A.; Rogl, P.; Peranio, N.; Bauer, E.; Zehetbauer, M.; Eibl, O. *Acta Mater.* **2014**, *63*, 30.

[10] a) Poudel, B.; Hao, Q.; Ma, Y.; Lan, Y. C.; Minnich, A.; Yu, B.; Yan, X. A.; Wang, D. Z.; Muto, A.; Vashaee, D.; Chen, X. Y.; Liu, J. M.; Dresselhaus, M. S.; Chen, G.; Ren, Z. F. *Science* **2008**, *320*, 634. b) Xie, W. J.; He, J.; Kang, H. J.; Tang, X. F.; Zhu, S.; Laver,

M.; Wang, S. Y.; Copley, J. R. D.; Brown, C. M.; Zhang, Q. J.; Tritt, T. M. *Nano Lett.* **2010**, *10*, 3283. c) Kim, S. I.; Lee, K. H.; Mun, H. A.; Kim, H. S.; Hwang, S. W.; Roh, J. W.; Yang, D. J.; Shin, W. H.; Li, X. S.; Lee, Y. H.; Snyder, G. J.; Kim, S. W. *Science* **2015**, *348*, 109.

[11] a) Heremans, J. P.; Jovovic, V.; Toberer, E. S.; Saramat, A.; Kurosaki, K.; Charoenphakdee, A.; Yamanaka, S.; Snyder, G. J. *Science* **2008**, *321*, 554. b) Pei, Y. Z.; Shi, X. Y.; LaLonde, A.; Wang, H.; Chen, L. D.; Snyder, G. J. *Nature* **2011**, *473*, 66.

[12] Zhang, G.; Yu, Q.; Yao, Z.; Li, X. *Chem. Commun.* **2009**, 2317.

[13] Lotgering, F. K. *J. Inorg. Nucl. Chem.* **1959**, *9*, 113.

[14] May, A. F.; Toberer, E. S.; Saramat, A.; Snyder, G. J. *Phys. Rev. B* **2009**, *80*, 125205.

[15] Perdew, J. P.; Ruzsinszky, A.; Csonka, G. I.; Vydrov, O. A.; Scuseria, G. E.; Constantin, L. A.; Zhou, X. L.; Burke, K. *Phys. Rev. Lett.* **2008**, *100*, 136406.

[16] Blochl, P. E. *Phys. Rev. B* **1994**, *50*, 17953.

[17] Kresse, G.; Joubert, D. *Phys. Rev. B* **1999**, *59*, 1758.

[18] Lany, S.; Zunger, A. *Phys. Rev. B* **2008**, *78*, 235104.

[19] Massalski, T. B.; Okamoto, H.; Subramanian, P. R.; Kacprzak, L.

Alloy Phase Diagrams. ASM International: Materials Park, OH, **1990**.

[20] Yin, Y. D.; Rioux, R. M.; Erdonmez, C. K.; Hughes, S.; Somorjai, G. A.; Alivisatos, A. P. *Science* **2004**, *304*, 711.

[21] Jiang, Y.; Wang, Y.; Sagendorf, J.; West, D.; Kou, X.; Wei, X.; He, L.; Wang, K. L.; Zhang, S.; Zhang, Z. *Nano Lett.* **2013**, *13*, 2851.

[22] Chung, I.; Malliakas, C. D.; Jang, J. I.; Canlas, C. G.; Weliky, D. P.; Kanatzidis, M. G. *J. Am. Chem. Soc.* **2007**, *129*, 14996.

[23] Guan, L. H.; Suenaga, K.; Shi, Z. J.; Gu, Z. N.; Iijima, S. *Phys. Rev. Lett.* **2005**, *94*, 045502.

[24] Pennycook, S. J.; Jesson, D. E. *Phys. Rev. Lett.* **1990**, *64*, 938.

[25] Shannon, R. D. *Acta Cryst. A* **1976**, *32*, 751.

[26] a) Pei, Y. Z.; LaLonde, A.; Iwanaga, S.; Snyder, G. J. *Energy Environ. Sci.* **2011**, *4*, 2085. b) Wei, T. R.; Tan, G.; Zhang, X.; Wu, C. F.; Li, J. F.; Dravid, V. P.; Snyder, G. J.; Kanatzidis, M. G., *J. Am. Chem. Soc.* **2016**, *138*, 8875.

[27] Yan, X. A.; Poudel, B.; Ma, Y.; Liu, W. S.; Joshi, G.; Wang, H.; Lan, Y. C.; Wang, D. Z.; Chen, G.; Ren, Z. F. *Nano Lett.* **2010**, *10*, 3373.

[28] Goldsmid, H. J. *Applications of thermoelectricity*. Methuen,

Wiley: London, NY, **1960**.

[29] Mehta, R. J.; Zhang, Y. L.; Karthik, C.; Singh, B.; Siegel, R. W.; Borca-Tasciuc, T.; Ramanath, G. *Nat. Mater.* **2012**, *11*, 233.

Bibliography

1. International Publications

1) **Kunsu Park**, Kyunghan Ahn, Joonil Cha, Sanghwa Lee, Sue In Chae, Sung-Pyo Cho, Siheon Ryee, Jino Im, Jaeki Lee, Su-Dong Park, Myung Joon Han, In Chung, Taeghwan Hyeon,

"Extraordinary Off-Stoichiometric Bismuth Telluride for Enhanced n-Type Thermoelectric Power Factor"

Journal of American Chemical Society, in press.

2) **Kunsu Park**, Jae Sung Son, Sung Ill Woo, Kwangsoo Shin, Min-Wook Oh, Su-Dong Park, Taeghwan Hyeon,

"Colloidal Synthesis and Thermoelectric Properties of La-doped $SrTiO_3$ Nanoparticles"

Journal of Materials Chemistry A, **2014**, *2*, 4217.

3) **Kunsu Park**, Yuwon Park, Mihyun Park, Euiyeon Jung, Mi-Sook Kwon, Sue In Chae, Sanghwa Lee, Arun Kumar Sinha, Kyu Tae Lee, Taeghwan Hyeon,

"Bulk Nanostructured P2-$Na_{2/3}MnO_2$ for Na-Ion Battery Cathode"

Manuscript in Preparations.

4) Jae Sung Son, **Kunsu Park**, Mi-Kyung Han, Chanyoung Kang, Sung-Geun Park, Jae-Hee Kim, Woochul Kim, Sung-Jin Kim, Taeghwan Hyeon,

"Large-Scale Synthesis and Characterization of the Size-Dependent Thermoelectric Properties of Uniformly Sized Bismuth Nanocrystals"

Angewandte Chemie International Edition, **2011**, *50*, 1363.

5) Jae Sung Son, Xiao-Dong Wen, Jin Joo, Jungseok Chae, Sung-il Baek, **Kunsu Park**, Jeong Hyun Kim, Kwangjin An, Jung Ho Yu, Soon Gu Kwon, Sang-Hyun Choi, ZhongwuWang, Young-Woon Kim, Young Kuk, Roald Hoffmann, Taeghwan Hyeon,

"Large-Scale Soft Colloidal Template Synthesis of 1.4 nm-Thick CdSe Nanosheets"

Angewandte Chemie International Edition, **2009**, *48*, 6861

6) Jae Sung Son, **Kunsu Park**, Soon Gu Kwon, Jiwoong Yang, Moon Kee Choi, Junhyeong Kim, Jung Ho Yu, Jin Joo, Taeghwan Hyeon,

"Dimension-Controlled Synthesis of CdS Nanocrystals: From 0D Quantum Dots to 2D Nanoplates"

Small, **2012**, *8*, 2394.

7) Jae Sung Son, Moon Kee Choi, Mi-Kyung Han, **Kunsu Park**, Seong Joon Lim, Myunghwan Oh, Young Kuk, Chan Park, Sung-Jin Kim, Taeghwan Hyeon,

"n-Type Nanostructured Thermoelectric Materials Prepared from Chemically Synthesized Ultrathin Bi_2Te_3 Nanoplates"

Nano Letters, **2012**, *12*, 640.

8) Donghee Son, Sue In Chae, Myungbin Kim, Moon Kee Choi, Jiwoong Yang, **Kunsu Park**, Vinayak S. Kale, Ja Hoon Koo, Changsoon Choi, Minbaek Lee, Ji Hoon Kim, Taeghwan Hyeon, Dae-Hyeong Kim,

"Colloidal Synthesis of Uniform-Sized Molybdenum Disulfide Nanosheets for Wafer-Scale Flexible Nonvolatile Memory"

Advanced Materials, *in press*.

2. International Conference

1) **Kunsu Park**, Taeghwan Hyeon,

"High Temperature Thermoelectric Properties of La-doped $SrTiO_3$ nanocomposites", (oral presentation)

The 2012 ACS Fall Meeting, Philadephia, U.S.A., August, 19-23, **2012**.

2) **Kunsu Park**, Taeghwan Hyeon

"Colloidal Synthesis and Theromelectric Properties of La-doped $SrTiO_3$ Nanoparticles",

45th IUPAC World Chemistry Congress, BEXCO, Busan, Korea, August 9-14, **2015**.

3) **Kunsu Park**, Sue In Chae, In Chung, Taeghwan

Hyeon

"Synthesis of Doped-Bi_2Te_3 Nanotubes for Enhanced Thermoelectric Performance",

9th International Conference on Quantum Dots, Ramada Hotel, Jeju, Korea, May 22-27, **2016**.

3. Domestic Conference

1) **Kunsu Park**, Taeghwan Hyeon

"Collodial Synthesis and Thermoelectric Properties of La-doped $SrTiO_3$ Nanoparticles"

NANO KOREA 2014 Symposium, COEX, Seoul, Korea, July 2-4, **2014**.

초 록

열전 물질의 성능 향상은 다양한 응용범위로의 확대를 위하여 매우 중요하다. 최근에 열전 물질에 나노 구조를 도입함으로써 열전도도를 낮추어 그 성능 지수 ZT를 높이는 방법이 새롭게 개발되어 각광을 받고 있다. 이 학위 논문은 열전 물질들을 나노 입자로 합성하는 방법에 대하여 논의하고, 그것들의 열전 성능들을 측정하고 기술하였다. 알려진 다양한 열전 물질들 중에 이 논문은 도핑된 다결정 나노벌크 물질의 개발과 그 도핑 기작에 대해 고찰하였으며 차후 유망한 열전 물질들을 개발할 수 있는 비전을 제시하였다.

첫번째로, lanthanum 도핑농도를 조절하며 도핑된 티탄산 스트론튬 물질을 합성하는데 성공하였으며 그 열전 성능을 측정하였다. 합성된 나노입자들을 spark plasma sintering 을 이용하여 다결정 나노벌크를 제조하였다. ZT는 973 K에서 0.37을 나타내었는데 이는 기존의 단결정 벌크 물질보다 약 25% 정도 높은 성능으로서 이 같은 성능 향상은 나노 구조 도입을 통하여 성공적으로 열전도도를 낮추면서도 전기전도도와 제백상수가

유지되었기 때문이다. 더불어 이 방법으로 제조한 lanthanum이 도핑된 티타산 스트론튬 나노벌크는 높은 열적 안정성을 보였는데 이는 고온 열전 물질로의 적합성을 보여준다고 할 수 있다.

두번째로, 일반적인 상평형 구성을 이루지 않는 새로운 비스무스 텔루라이드의 도핑된 다결정 나노벌크를 나노입자 합성을 기반으로 하여 제조하였다. 게다가 새롭게 poatssium 양이온을 도핑을 하여 carrier 농도를 조절하는데 성공하였다. 과량의 tellurium과 potassium 이온들은 주사투과전자현미경과 전자 에너지 손실 분광법을 통하여 분석할 수 있었으며, 이러한 분석법들과 밀도 함수 이론 계산을 통하여 도핑된 potassium의 정확한 위치들도 확정할 수 있게 하였다. 열전 성능 측정을 통하여 이렇게 제조된 나노벌크가 전기전도도와 제백상수의 큰 향상을 가져왔다는 것을 확인하였으며 그 결과 350 K에서 1.1 이 넘는 높은 ZT를 얻을 수 있었으며 이는 ZT는 n-type 비스무스 텔루라이드 중 가장 높은 값들 중 하나이다.

주요어: 열전 물질, 도핑, 나노 벌크, 나노입자 합성, 티탄산 스트론튬, 비스무스 텔루라이드.

학번: 2009-20989